ABSTRACT

Title of Document: SYNTHESIS AND CHARACTERIZATION OF OXIDE THIN FILMS FOR ION TRANSPORT

Richmond Shiwei Wang
Doctor of Philosophy, 2023

Directed By: Professor Ichiro Takeuchi
Department of Materials Science and Engineering

Metal oxides are a diverse category of materials that exhibit many material properties and applications. They can range from insulators to superconductors and have uses varying from electronic semiconductor devices to solar cells and even biomedical applications. Thin films, specifically, attract interest due to their unique properties compared to the bulk alternatives. Their small nano to micro scale size provides a large surface to volume ratio, which can affect defect density and alter the optical, electrical, or mechanical properties. The ease of fabrication and the tunability of thin films through techniques such as strain engineering or doping enables them to be widely utilized to characterize material properties and interfaces.

Of these metal oxides, perovskite rare-earth nickelates exhibit intriguing electrical and optical properties, such as metal-to-insulator transitions. $LaNiO_3$ is the only exception where the metallic phase is robust at all temperatures. Electrolyte gating can be an efficient method to manipulate the electronic behavior of $LaNiO_3$ and induce an insulating phase. This work utilized ionic liquid gating with electric double-layer transistor devices to control the electronic properties of $LaNiO_3$. The electrolyte gating leads to an insulating phase transition with an increased film

resistivity by over six orders of magnitude. The electrolyte gating behaviors are found to be dependent on not only gating voltage and duration, but also the atmospheric environment. X-ray photoelectron spectroscopy (XPS) analysis revealed that ionic liquid gating promotes the removal of oxygen from the crystal to form oxygen vacancies, which also affects the Ni valence state. The insulating phase transition was attributed to enhanced electron correlation as well as an opening of the charge transfer gap due to the reduced overlap between Ni and O bands. The filling of carriers is controlled by the gate voltage. These results suggest that electrolyte gating devices can be useful for manipulating electron-electron correlation, furthering materials research in realizing exotic physics in correlated systems.

Li-ion batteries are widely used in electronics, appliances, electric vehicles, and energy storage systems. The transport of the Li ions in Li-ion batteries can be affected by many factors, such as crystal structure or the formation of interfaces between the electrodes and the electrolyte used. Investigation of delithiation in a $LiCoO_2$ cathode and the effects of Li removal on the structure demonstrated that charge compensation occurs via the formation of Co^{4+} and hole generation near O atoms. One drawback of conventional Li ion batteries is the flammability of the liquid electrolyte solvents. $Li_7La_3Zr_2O_{12}$ (LLZO) solid electrolytes have been considered an alternative to these liquid electrolytes. However, the reduced ionic conductivity of LLZO needs to be improved to fully realize their use in Li ion batteries.

A hybrid electrolyte composed of LLZO with small amounts of liquid electrolyte can potentially resolve this issue by increasing Li conductivity between the LLZO and electrodes. This results in the formation of a solid-electrolyte interface, which can adversely affect the performance of the overall battery. To fully understand how this interface forms and how it impacts the performance, Ta-doped LLZO/Li_2O multilayer films were exposed to a liquid electrolyte solution

containing $LiPF_6$. XPS analysis showed that carbon contaminants such as $LiCO_2$ were reduced upon electrolyte exposure. Fluorinated metals such as LiF, LaF_3, and ZrF_4 were detected at depths up to 10 nm, suggesting that LLZO interacts more strongly with HF than other decomposition products of the electrolyte. Overcoming the formation of fluorinated metals is critical to realizing hybrid electrolytes that use the SE LLZO in combination with a LE containing $LiPF_6$ without being inhibited by solid-electrolyte formation.

SYNTHESIS AND CHARACTERIZATION OF OXIDE THIN FILMS FOR ION TRANSPORT

by

Richmond S. Wang

Dissertation submitted to the Faculty of the Graduate School of the

University of Maryland, College Park in partial fulfillment

of the requirements for the degree of

Doctor of Philosophy

2023

Advisory Committee:
Prof. Ichiro Takeuchi, Committee chair
Prof. Patrick McCluskey, Dean's representative
Prof. You Zhou
Prof. Isabel Lloyd
Prof. Luz Martinez-Miranda

Dedication

To my wife and family, for their never-ending support in my endeavors.

Acknowledgements

I would like to acknowledge and thank my advisor, Prof. Dr. Ichiro Takeuchi, for his guidance and mentorship throughout my time in his group. His expertise and knowledge were immensely appreciated in helping create the framework of my research. The freedom in exploring different projects and materials allowed me to partake in a wide array of projects.

I would also like express my gratitude to the members of the research group for their support, guidance, and friendship. The help they gave was invaluable, and I would especially like to thank Dr. Rohit Pant and Jihun Park for their part in making these projects possible. I would like to thank Justin Seth Pearson for introducing me and guiding me in my first steps as part of this group. A big thank you to the other members in no particular order: Thomas Wong, Dr. Dylan Kirsch, ChihYu Lee, Dr. Heshan Yu, Haotong Liang, Dr. Sabrina Curtis, Ryan Paxson, and anyone else I may have missed.

I am grateful to Dr. You Zhou and his guidance and expertise on rare-earth nickelates and the ionic liquid gating project. I would also like to thank his current and past students, Suraj Maurya, Liuxin Gu, and Ruihao Ni for their assistance with the ionic liquid gating project and with the contact depositions in the Fablab.

The entire Materials Science and Engineering Faculty and Staff have supported me during my entire duration as part of this department, beginning from when I first joined as an undergraduate in 2016. The past seven years have been an integral and memorable part of my life, and I am grateful to the department and everyone in it for welcoming me and supporting me. I would especially like to thank Dr. Isabel Lloyd for taking me on as an undergraduate researcher

and supporting me through my first year in the graduate program. Her guidance was invaluable, and I am thankful that she supported my decision to continue pursuing a PhD in this department.

A special thank you to my committee members for their service: Dr. Isabel Lloyd, Dr. Martinez-Miranda, Dr. You Zhou, Dr. Patrick McCluskey, and finally, Dr. Ichiro Takeuchi.

I would like to acknowledge the support of the Maryland NanoCenter and its Fablab and AIMlab. I would also like to acknowledge the X-ray Crystallographic Center. I am grateful for the support of the members of the Quantum Materials Center, especially Dr. Tarapada Sarkar for his expertise on pulsed laser deposition and Brian Straughn for his support of the QMC.

I would like to acknowledge the generous funding support for this work provided by U.S. Department of Education's Graduate Assistance in Areas of National Need (GAANN) Fellowship, the Clark Doctoral Fellows Program, ONR MURI, AFOSR, and NIST grants.

I would lastly like to thank my parents, Faye Chen and Alex Wang, and my sister Dorothy, for their support in my journey and shaping me into the person I am today. I would like to thank my friends for being there and encouraging me to keep working towards my goal. And finally, I want to thank my partner and wife, Josie, for her endless love and support. They have been a great help over the past several years.

Thank you,

Richmond Shiwei Wang

Table of Contents

List of Tables

List of Figures

Chapter 1. Introduction

1.1 Metal oxides

Metal oxides encompass a large variety of materials with different chemical compositions and crystal structures. The term metal oxide refers to compounds which are composed of the oxygen element and another metal chemical element. Complex metal oxides are metal oxides which contain oxygen and at least two other elements or metals with two oxidation states[1,2]. This class of material hosts a wide range of exciting properties, such as magnetic and electronic properties. As an example, the electrical properties of metal oxides can vary from being insulating, to semiconducting, metallic, and even superconducting. Lanthanum aluminate $LaAlO_3$ is an insulator, while yttrium barium copper oxide is a notable high-temperature superconductor. Other notable properties include ferromagnetism, colossal magnetoresistance, ferroelectricity, and thermal metal-to-insulator transitions.

In addition to the wide range of tunable properties, metal oxides can be easily prepared and synthesized in many forms and with a variety of techniques. By altering the synthesis process and the chemical composition in the metal oxides, different properties can be induced. Metal oxides can be studied and utilized in bulk form or as thick or thin films, exhibiting unique properties in each form. Synthesis can occur through methods such as sintering, sol-gel, or various deposition techniques. The ease of synthesis and versatility of metal oxides makes them enables their use in numerous applications, such as electrodes, fuel cells, gas sensors, transistors, photovoltaics, non-volatile memories, and other energy, health, and electronics fields[3–8]. Thin film metal oxides are particularly attractive due to their prevalence in device fabrication and the ability to study the structure-property relationships of the materials[3,4].

Thin films are layers of materials that have a thickness within a range of a nanometer to several micrometers. The properties of thin film materials vary from those of their bulk form. The nanostructure of thin films and interfacial effects with substrates can contribute to these differences. For example, thin films can have a higher defect density due to the small size, which can include vacancies or interstitials in the crystal structure. This can yield a higher hardness or reduced conductivity in thin films when compared to their bulk counterparts. The smaller size also yields a shorter mean free path for charge carriers in a thin film, which can affect the electrical or optical properties. A larger surface to volume ratio means that surface properties such as surface roughness have a much larger impact on material properties in thin films. Thin films are more sensitive to thermomechanical stresses. Tensile or compressive strains are common due to the deposition process of thin films on substrates. Residual stresses in films can lead to deviations in electrical properties and the adhesion of the thin film onto various surfaces, such as for coatings. Single crystal thin films can also have preferred orientations, which can affect anisotropic properties when compared to bulk polycrystalline samples. The small, nanoscale size of these films makes them versatile in many fields, such as in electronic devices, coatings, photovoltaics, and biomedical applications. The ease of fabrication and the tunability of thin films during synthesis makes them widely used to characterize material properties and interfaces[4,9,10].

Ion transport in materials occurs when atoms, ions, and/or defects diffuse between definite sites in the crystal structure. Examples of ion transport include oxygen vacancies diffusing through the material, or ions hopping between different sites in a crystal lattice. Defects in the system, which include Schottky defects or Frenkel defects, have a large impact on the ion transport in metal oxides. Schottky defects refer to point defects in films, such as the oxygen vacancies in a material. These defects form when charged ions leave their lattice sites and diffuse to the surface of the

material, leaving behind oppositely charged vacancies. Meanwhile, Frenkel defects occur when charged ions exit their lattice sites and instead occupy an interstitial site. Defects in materials can be induced using a variety of methods, such as applying strain or doping a material. The concentration of defects that exist in a material can have an impact on its material properties[11,12]. In thin films, the smaller size results in a larger defect density when compared to bulk, increasing the effects that defects can have on the ion transport properties.

In metal oxides, properties can be greatly influenced by the oxygen content within the material. Oxygen vacancies can form in a material during synthesis or through other post-synthesis processes, such as high-temperature vacuum annealing. Figure 1.1 shows the structure of perovskite $SrTiO_3$ with oxygen vacancies present in the crystal structure. The formation of oxygen vacancies in any oxide can be shown with the following defect equation:

$$O_O^x = V_O^{2\bullet} + 2e' + \frac{1}{2}O_2(g) \quad (1)$$

Where O_O^x denotes oxygen atoms occupying a normal oxygen lattice site with zero effective charge, $V_O^{2\bullet}$ denotes oxygen vacancy sites with two positive effective charges, e' denotes electrons with a negative charge, and O_2 indicates the presence of oxygen gas[13]. This process can also be reversed to reduce vacancies by adding oxygen into the crystal. The presence of oxygen vacancies can have drastic effects on a materials structure and properties, such as electronic conductivity and light absorption. This is due to the change in charge carrier concentration, where a larger concentration of electrons increases the conductivity. For instance, raising the oxygen partial pressure surrounding SnO_2 nanowires causes oxygen to diffuse into the bulk material, filling the vacancies, which is accompanied by an increase in the resistivity[14]. This tunability of the material properties due to oxygen vacancy formation makes metal oxides desirable for applications such solar cells[15],

catalysts[16], and in gas sensors[17]. The focus of this dissertation involved two categories of metal oxides: rare-earth nickelates and lithium complex oxides.

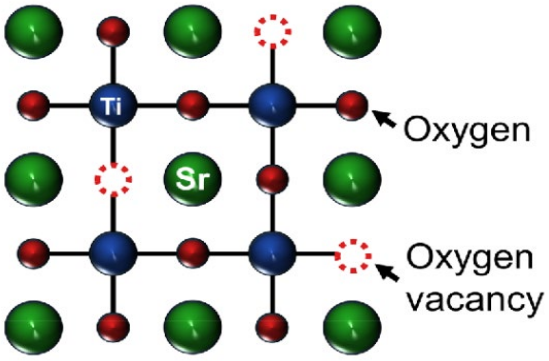

Figure 1.1. Oxygen vacancy defects in perovskite $SrTiO_3$[18].

1.2 Rare-earth nickelates

Transition metal oxides are a category of metal oxides which have interesting structural, electronic, magnetic, and optical properties. The unique properties of these materials are due to the behavior of the *d*-electrons in the transition metals. The partially filled *d*-valence in transition metals can induce spin and orbital degrees of freedom, promoting electron transfer between oxygen and metal ions in the material. The *d*-shells can also contribute to properties such as a wide bandgap or a high dielectric constant[6]. One important factor is the strong electron-electron correlation of transition metal oxides, which contributes to a metal-to-insulator transition that occurs in many of these materials[19–21].

An example of a family of transition metal oxides are rare-earth nickelates. Rare-earth nickelates have the chemical formula $RNiO_3$, where R represents one of the rare-earth elements, such as lanthanum, neodymium, or samarium. These materials exhibit a perovskite structure, which is characterized by the formula ABO_3. A and B represent two metal cations, where the A ion has a larger radius than the B ion. In this structure, the B atoms, Ni, bond with ligand oxygen atoms to form a BO_6 octahedra unit, while the A atoms occupy the cavities between the BO_6 octahedra and are 12-fold coordinated with the oxygen atoms[22,23]. Figure 1.2 shows the cubic and orthorhombic unit cells that can be found in perovskite crystals. In each image, the purple sphere represents the A cation. The orange spheres at the corner of the cubic unit cell represent the B cation and are 6-fold coordinated with the red O anion spheres. Regardless of crystal structure, it is convenient to describe the material with respect to its pseudocubic unit cell[22,24,25], indicated by the red arrows in orthorhombic unit cell depicted in Figure 1.2b. For example, the [010] direction in the pseudocubic unit cell corresponds to the [110] direction in the orthorhombic unit cell.

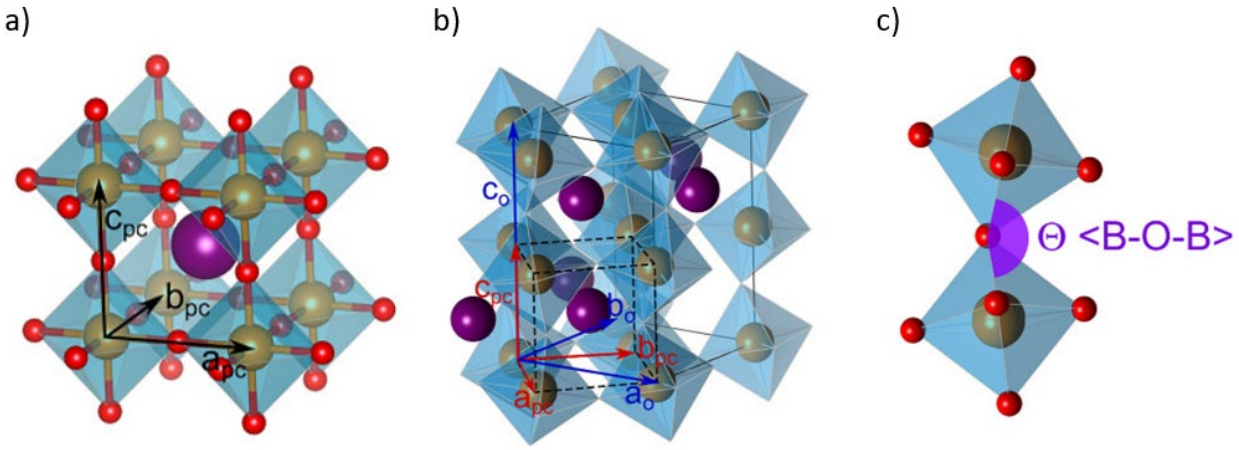

Figure 1.2. (a) Cubic and (b) orthorhombic unit cells with pseudocubic unit cells notated. (c) Distortion of B-O-B bond angle affected by cation size, where B indicates Ni ions in $RNiO_3$. In all panels, the A cation is the purple sphere, the B cation is represented by the orange sphere, and the O anions are represented by the red spheres[22].

While the ideal structure of perovskites is cubic, structural distortions can cause the crystal to adopt orthorhombic or rhombohedral structures. This depends on the ionic radii of the ions and can be estimated using the Goldschmidt tolerance factor *t:*

$$t = \frac{r_A + r_O}{\sqrt{2}(r_B + r_O)} \tag{2}$$

Where r_A, r_B, and r_O represent the ionic radius of the A, B, and O ions respectively[22]. When $0.9 < t < 1$, the cubic $Pm\bar{3}m$ structure is most stable. As r_A increases, the tolerance factor decreases (t < 0.9), and the crystal adopts either a rhombohedral or orthorhombic structure, with a space group of either $R\bar{3}c$ or $Pbnm$, respectively. This variation in crystal structure is due to distortions and rotations that occur within the BO_6 octahedral corner units. This can be quantified through a change in the B-O-B bond angle, which scales proportionally with *t*. Lower tolerance factors lead to a much narrower B-O-B bond angle seen in Figure 1.2c, which can affect the overlap between orbitals and cause changes in the structure and properties of the material. In $RNiO_3$, this is signified by the Ni-O-Ni bond angle[22,26].

An important feature of perovskite rare-earth nickelates is the metal-to-insulator transition (MIT). Most materials exhibit either metallic or insulating temperature dependent resistivity behaviors. When the temperature decreases, the resistivity of metals decreases. Meanwhile, semiconductors and insulators increase their resistivity as the temperature decreases. In some materials, such as transition metal oxides, there exists a transition temperature, the MIT, where the material changes from metallic behavior to insulating behavior when decreasing the temperature. At the MIT temperature, the material undergoes a phase transition, resulting in structural changes that can affect the overall properties of the material, such as its resistivity. The structural and physical properties of perovskite nickelates can be summarized with their phase diagram, which depicts the transition temperature and its relation to *t* and the Ni-O-Ni bond angle[22]. A decrease in the rare-earth cation size results in a lower tolerance factor and reduces the Ni-O-Ni angle. This also results in a reduction of the overlap between the Ni-3*d* and O-2*p* orbitals, affecting the bandwidth of the orbitals and increases the resistivity, consequently increasing the MIT temperature[22,27]. Figure 1.3 shows the phase diagram of $RNiO_3$ showing the relationship between *t*, the Ni-O-Ni bond angle, and the MIT.

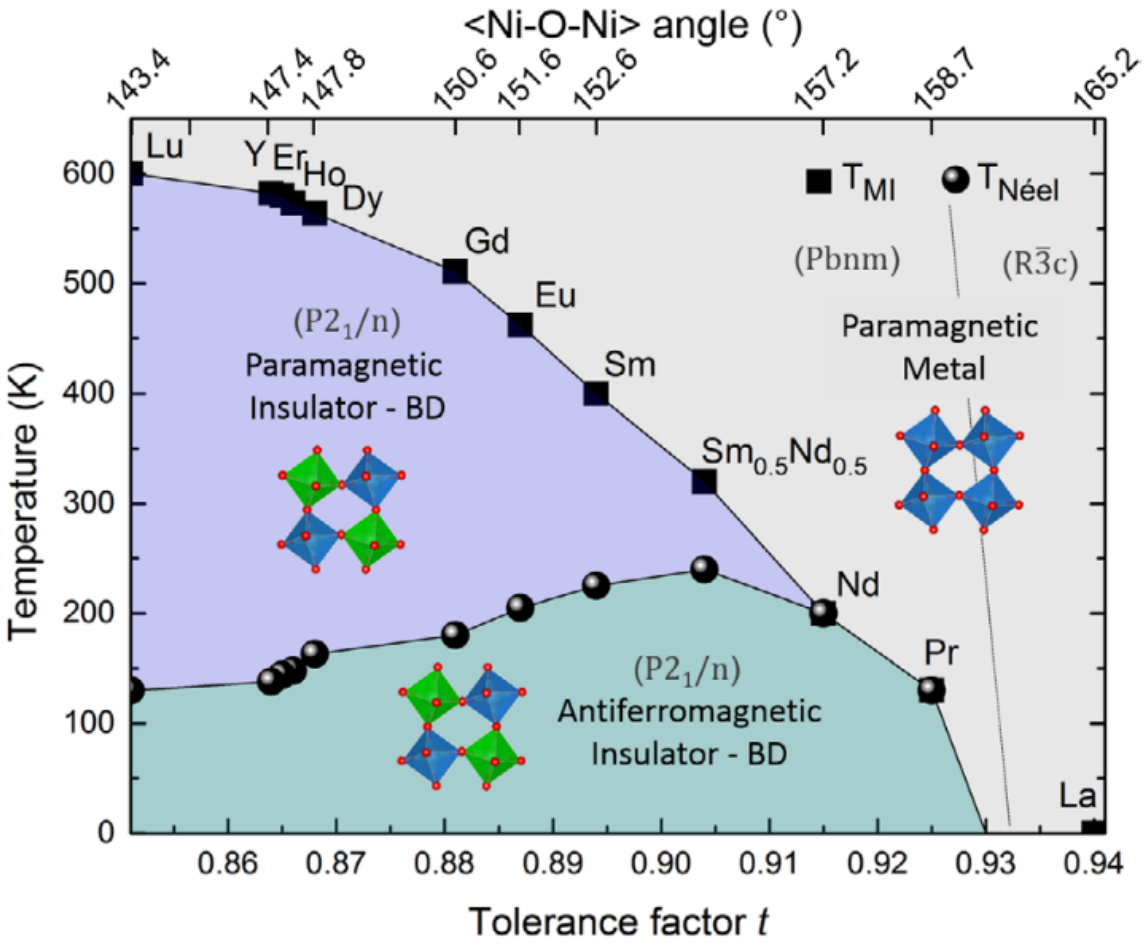

Figure 1.3. Phase diagram of $RNiO_3$ family showing the relationship between tolerance factor, Ni-O-Ni bond angle, and MIT temperature with increasing cation size of the rare-earth element. Néel transition is also shown[22].

The metallic phase in $RNiO_3$ materials originates from the hybridization of the Ni *3d* and O *2p* bands[22,28–31]. The primary mechanism behind the MIT has been attributed to charge disproportionation, wherein the bandgap opened by the charge disproportionation is strongly influenced by the Ni-O-Ni bond angle[22,27,29,30,32,33]. In rare-earth nickelates, the *d* band of the transition metal ions such as nickel, lie close to the *p* band of ligand oxygen ions. In this situation, electrons can transfer from the oxygen *p* band to the *d* orbitals, resulting in a ligand hole *L* in the oxygen band and an additional electron on the transition metal site:

$$d^n \rightarrow d^{n+1}L \tag{3}$$

This requires a certain amount of energy to occur, referred to as the charge transfer gap Δ and occurs in charge-transfer (CT) insulators. Other mechanisms involve the hopping of electrons between sites in the *d* orbital, leaving one unoccupied site and one doubly occupied site. This double occupancy is controlled by the Coulomb interaction, *U*, which and is present in Mott-Hubbard insulators[22] and defines the energy required for the process:

$$d_i^n + d_j^n \rightarrow d_i^{n+1} + d_j^{n-1} \tag{4}$$

Depending on the band structure, different materials can show either Mott-Hubbard or CT insulating behavior, as shown in Figure 1.4.

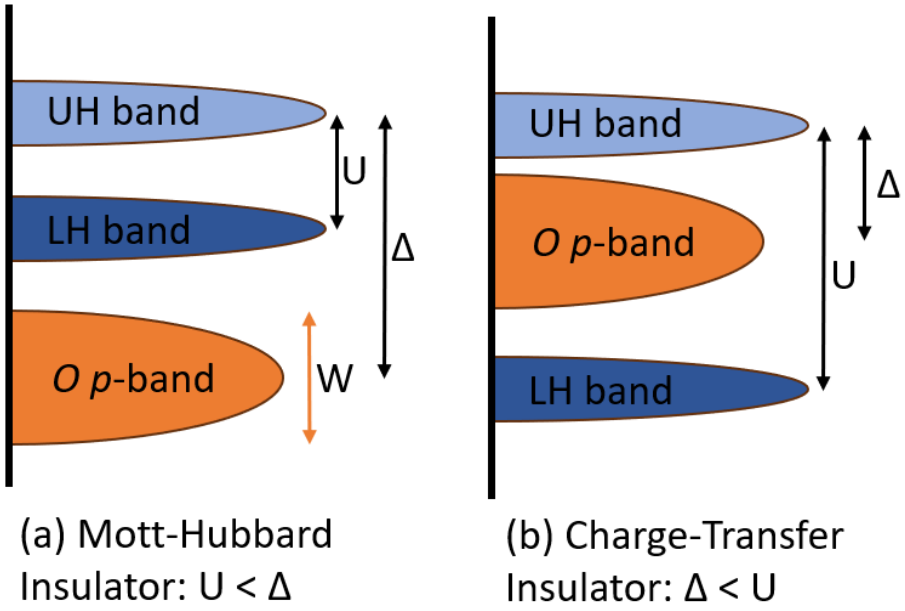

Figure 1.4 Band structure schematic of (a) a Mott-Hubbard insulator and (b) a Charge-Transfer insulator.

In $RNiO_3$, the dominant Ni valence state should be Ni^{3+} with 7 electrons in the *d* orbital, resulting in the d^7 spin configuration of $t_{2g}^6 e_g^1$. A relatively small Δ facilitates the transfer of

electrons from the oxygen 2p bands to nickel 3d bands, resulting in the electron configuration of d^8L. In the metallic state, the d^8L configuration is present in nearly all Ni atoms. However, at temperatures below the MIT, this configuration splits into two different Ni sites with the following configuration:

$$d^8L + d^8L \rightarrow d^8 + d^8L^2 \tag{5}$$

In this situation, the d^8 state forms a larger octahedra with a charge equivalent to a Ni^{2+} cation. Meanwhile, the d^8L^2 state forms a smaller O_6 octahedra with a similar charge equivalent, but also shares two electrons from the surrounding oxygen ions because of the ligand holes. These two inequivalent Ni sites lead to charge and bond disproportionation with long and short Ni-O bonds, which can be seen in Figure 1.5. The difference between the two states is the spin states, where the d^8 state has a $t_{2g}^6 e_{g\uparrow}^2 e_{g\downarrow}^0$ configuration and the d^8L^2 state has a t_{2g}^6 configuration, equivalent to a Ni^{4+} spin configuration. This disproportionation results in decreased overlapping between the *d-p* orbitals, reducing the bandwidth of the system and resulting in an insulating phase forming[22,33].

While most rare-earth nickelates exhibit an MIT, $LaNiO_3$ shows metallic temperature-dependent resistivity behavior at all temperatures when in its bulk form. This can be attributed to its larger rare-earth cation size, which increases t and provides a much broader Ni-O-Ni bond angle. The structural distortions that occur at the BO_6 octahedral due to oxygen rotation are consequently reduced. This limits the transition from the metallic phase to an insulating phase. With a smaller rare-earth cation, the tolerance factor and thus Ni-O-Ni bond angle are reduced, and rotations can increase and result in further distortions. This reduces the bandwidth opens the bandgap to induce a MIT[24,29,34].

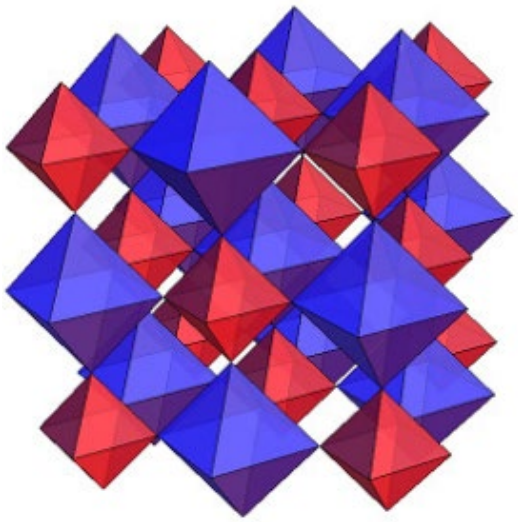

Figure 1.5. Charge disproportionation between the two NiO_6 octahedra of the $RNiO_3$ insulating state. The short-bond units (red) are surrounded by long-bond (blue) units[22].

The MIT in $RNiO_3$ is highly tunable, allowing the physical properties to be manipulated via means such as varying composition[35], strain engineering[24,28,35–38], doping effects such as cation substitution[39–43], or through oxygen vacancy control[26,29,44–51]. Many of these methods affect the lattice constants and modify the crystal structure of $RNiO_3$. These affect the Ni-O-Ni bond angle and bond lengths, which affect the MIT and overall properties. For instance, cation substitution can alter the tolerance factor due to a different cation size[39]. Oxygen vacancy control through methods such as vacuum annealing has been shown to induce an insulating phase and affect the MIT temperature[29,52]. The tunable electronic properties and phase transitions of $RNiO_3$ make it a promising material for many applications, such as in solid-oxide fuel cells (SOFC)[53] or as non-volatile memories[54] for neuromorphic computing.

1.2.1 Neuromorphic computing

Current computers use the von Neumann architecture, which separates data processing units and memory units which store data and instruction by encoding them in binary values. This requires the movement of data between memory units and processing units, which can limit the speed and increase energy consumption of computers (Figure 1.6). Neuromorphic computers bypass this limitation by processing and storing data in the same unit by utilizing artificial neurons and synapses, which seek to mimic the biological mechanisms in the brain[55–64].

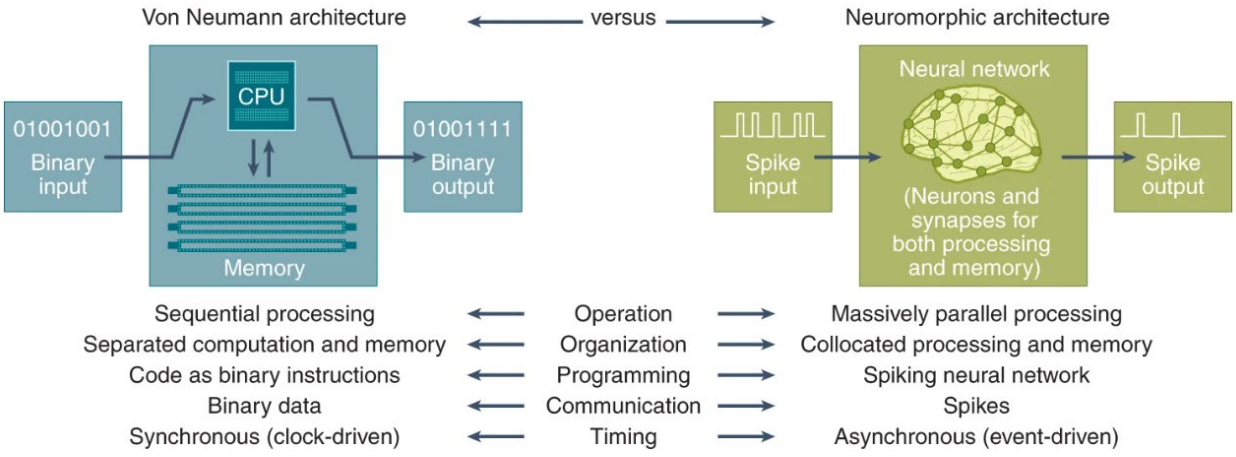

Figure 1.6. Von Neumann and neuromorphic architecture comparison[60].

The human brain uses a parallel architecture composed of neurons and synapses, which can be represented as computing and memory elements, respectively. The brain is highly connected, where billions of neurons are interconnected through synapses, forming a vast network. They interact with one another and transmit information with spikes of voltage pulses with varying strengths. This network is highly parallel, meaning all the neurons and synapses can operate simultaneously. This contrasts with von Neumann systems, where processing and memory occurs separately[58–62]. Another benefit of this connected network is the scalability, where an addition of

neurons and synapses can yield larger and larger networks. Neuromorphic computing seeks to mimic this behavior to overcome the limitations of traditional von Neumann computers.

Traditional von Neumann computers use transistors which act as a switch, existing in a binary on or off state. However, neuromorphic computing requires devices which can mimic the neurons and synapses in the brain, storing and transmitting data in spikes. In biological functions, the change in spike strength is defined as synaptic plasticity. This process, called spike-timing-dependent plasticity (STDP), modulates the signal strength between two neurons inside a synapse[61,62,65–67]. The change in synaptic weight is due to changes in the quantity of neurotransmitters and dendritic receptors in a neuron-synapse connection (Figure 1.7).

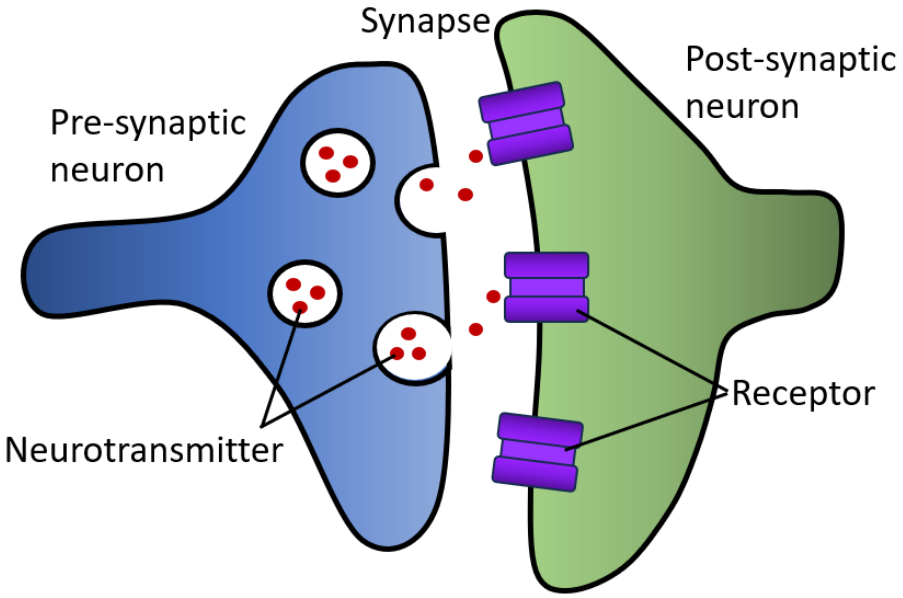

Figure 1.7 Diagram of neural synapse. Synaptic weight is determined by the quantity of neurotransmitters (red) and receptor molecules (purple).

Synaptic plasticity, or how the synapse weight changes, can be vital in how the brain undergoes learning and memory processes, which can be seen as following the Hebbian learning principle: cells that fire together, wire together[61,62]. In this principle, when one neuron is activated, the effectiveness of the signal is increased and passes this signal to the next neuron, forming an

interconnected network[68,69]. Understanding how the synaptic weight is modulated and mimicking this process can be key to utilizing neuromorphic computing. One method used to accomplish this is through non-volatile memories. Non-volatile memory is a type of memory that can store information even if external power is removed. Non-volatile memory arrays can form the basis of a neuromorphic network, mimicking the structure and function of biological neurons and synapses[57,59,61,70].

The most common form of non-volatile memories involves non-volatile resistance, where the resistance of a device can be modulated with an applied voltage pulse. Once the voltage pulse is removed, the device resistance remains at the modulated state until further pulses are applied[54]. This allows for control over the time and frequency of spikes in neuromorphic devices. Having multiple different conductance states also allows for different spike strengths to be tuned. One area of study that is being explored are materials and devices that can be utilized as non-volatile memories to mimic the behavior seen in the human brain, such as STDP for learning processes. Materials which have applications in neuromorphic computing utilize resistivity switching to realize STDP, where modulating the resistivity can mimic synaptic weight. Rare-earth nickelates are one class of materials which have tunable electrical properties.

1.2.2 Ionic liquid gating

The tunability of the MIT in $RNiO_3$ makes it a promising candidate for neuromorphic computing through resistivity switching. Modification of the electronic structure of $RNiO_3$ and thus the electrical properties has been shown using methods including strain engineering [24,28,35–38], cation substitution [39–43], or oxygen vacancy control [26,29,44–51]. The method focused on in this dissertation is oxygen vacancy control, which can also result in valence state changes. A promising method of manipulating oxygen vacancies in $RNiO_3$ is through ionic liquid (IL) gating[54,71–75]. Ionic liquid gating utilizes an electric double-layer transistor (EDLT) device design to manipulate the charge carrier density in a material. A diagram is shown in Figure 1.8.

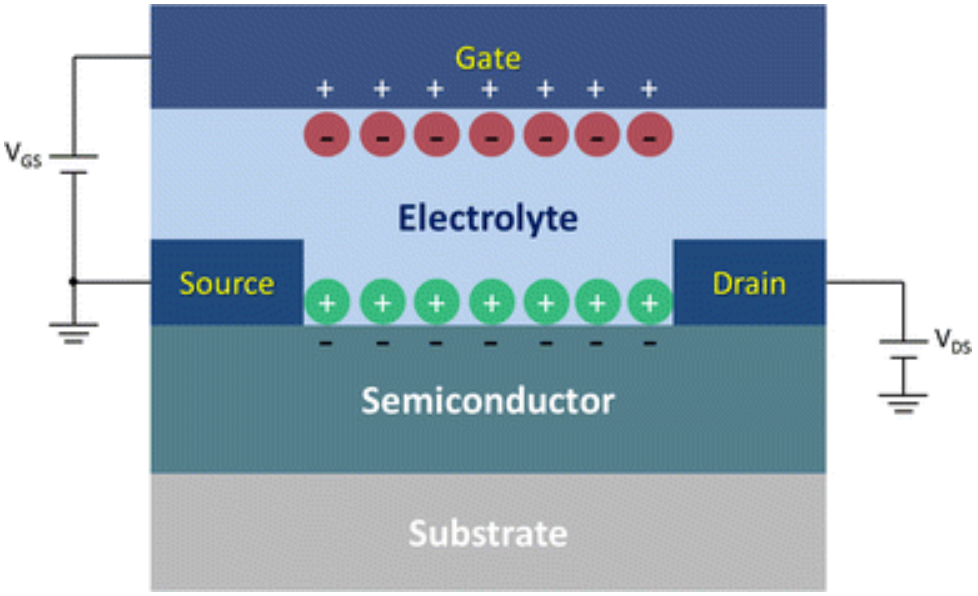

Figure 1.8 Diagram of electric-double-layer transistor using a semiconductor film and liquid electrolyte. V_{GS} indicates gate-source voltage path. V_{DS} indicates drain-source voltage path[76].

In an EDLT, the active source-drain channel through a sample is connected to an isolated gate electrode by a liquid electrolyte. An insulating barrier can be used to separate the gate electrode from contacting the source-drain electrodes. Ionic liquids are commonly used as the electrolyte due to their ability to achieve high carrier densities (10^{14} – 10^{15} cm^{-2}), as well as having

wide electrochemical stability windows, chemical flexibility, low vapor pressure, and a high ionic conductivity[74,77–79]. In the liquid phase, the cation and anion molecules in the organic salts of the IL are mobile, moving freely within the IL.

When a gate voltage (V_g) is applied to the electrolyte through the gate electrode, the mobile ions in the IL move towards the source or drain electrodes. At low voltages, they are unable to permeate the sample due to the size of the ions and therefore accumulate at the surface electrolyte/sample interface[76,77,80]. When a positive V_g (PGV) is applied, the negative anions in the IL accumulate on the surface of the gate electrolyte, while positive cations accumulate on the surface of the sample. This induces an equal charge density on the sample side of the interface to maintain charge neutrality, forming the electric double layer. When a negative V_g (NGV) is applied, the opposite occurs, where anions accumulate on the surface of the sample and result in a depletion of electrons near the interface[77,81,82]. The electric field applied to the gate electrode induces electrostatic charge accumulation and results in the doping of electrons or holes into the sample. Under a large voltage bias, mobile ions can penetrate the electrolyte/sample interface through an electrochemical process and generate interstitials, substitutional defects, or vacancies in the films[75,77,81,83], seen in Figure 1.9. At lower gate voltages, it has been shown that electrostatic doping effects of electrons or holes is the dominant mechanism, while electrochemical effects tend to dominate at larger gate voltages [77,81,84], such as when $V_g > 3$ V. However, it is likely that both mechanisms are present at different strengths during IL gating. The electrostatic charge accumulation effects at low gate voltages are largely reversible, while electrochemical doping can induce persistent changes in the electrical or magnetic properties of a material. This can be attributed to the defect formation that occurs deeper in the samples.

This process has been used to tune electrical properties and carrier mobility[85–87] and even induce superconductivity[88–92] in materials such as $KTaO_3$[93] or Pr_2CuO_4[94]. IL gating has been shown to affect the MIT[73,84,95–98] and superconducting behavior[89,99–101] in transition metal oxides. Such electrochemical processes lead to drastic and nonvolatile changes in a material's resistance and have been explored as a novel basis for neuromorphic computing[54,102,103]. In this dissertation, IL gating was used to induce oxygen vacancies and electron doping into $LaNiO_3$ thin films to demonstrate non-volatile memories with resistivity switching behaviors.

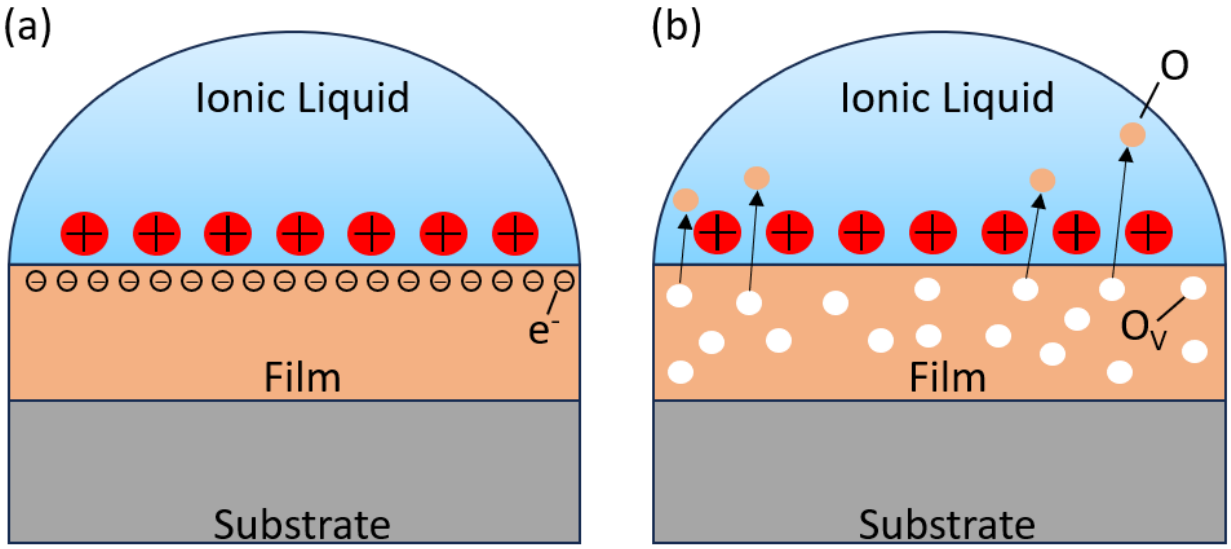

Figure 1.9 (a) Electrostatic and (b) electrochemical doping effects of ionic liquid gating. e- indicates electron, O indicates oxygen atoms, and O_V indicates oxygen vacancies.

1.3 Lithium-ion batteries

In 1972, Stanley Whittingham developed the first functional lithium battery, a rechargeable battery using a liquid electrolyte that utilized intercalated lithium ions. In 1980, John B. Goodenough replaced the original titanium disulfide cathode with lithium cobalt oxide, boosting the battery's voltage output. Then, in 1985, Akira Yoshino replaced the previous lithium metal anodes with a carbon-based anode, resulting in a much safer battery. These three individuals helped in pioneering LiB technology leading up to the first commercialized LiB by Sony Corporation in 1991, and in 2019, were recognized with a Nobel Prize in Chemistry[104–107].

Li-ion batteries are widely used in many products, ranging from small toys to appliances to electric vehicles and energy storage systems. Conventional Li-ion batteries consist of cells that utilize a liquid electrolyte (LE) placed between a cathode and anode material. Common electrodes used are lithium cobalt oxide ($LiCoO_2$) as the cathode and graphite as the anode, with $LiPF_6$ as one of the more commonly used LEs[108–111]. A polymer separator such as polyolefin acts as a barrier between the cathode and anode while enabling lithium-ion movement and preventing short-circuiting due to contact between the electrodes[112]. A schematic diagram is shown in Figure 1.10. During a discharge cycle, lithium atoms that are intercalated in the anode are ionized and separated from their electrons. The lithium ions move through the LE and permeate through the polymer separator, traveling from the anode to the cathode. Meanwhile, the electrons pass through an external circuit before recombining with the lithium ions at the anode. During the charging cycle, the lithium ions are released by the cathode and are stored back at the anode via intercalation, where the ions are inserted between the graphite layers[108,109,113].

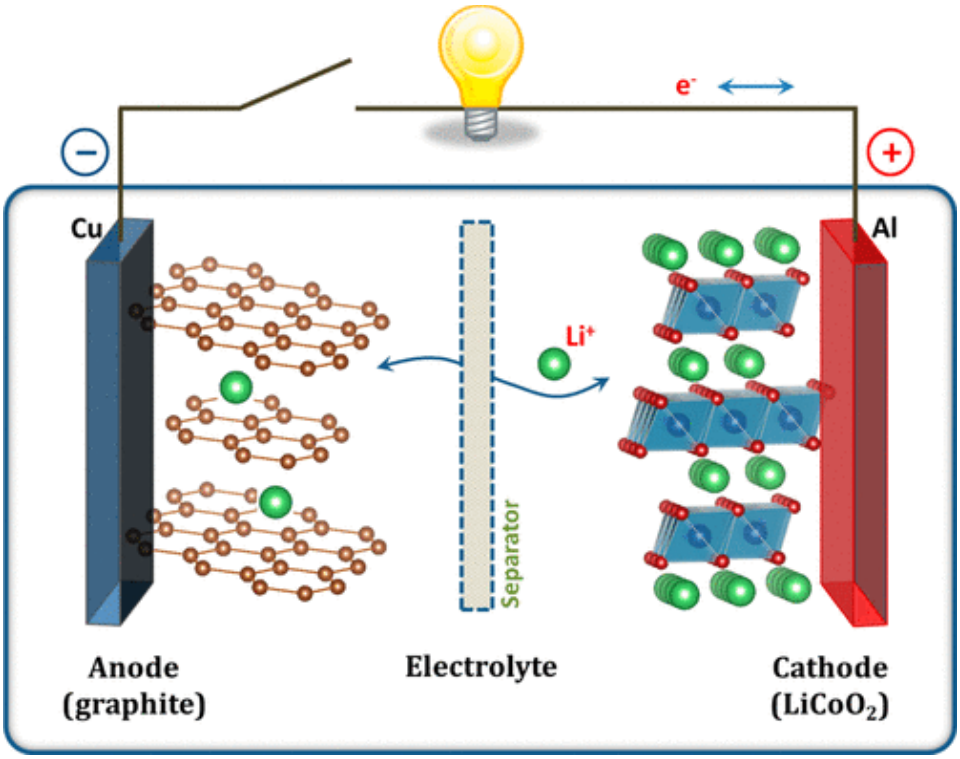

Figure 1.10 Lithium-ion battery diagram[114].

The overall performance of the LiB is greatly influenced by the materials used in its fabrication. For example, while a TiS_2 cathode has a relatively low voltage of around 2 V, $LiCoO_2$ cathodes have a significantly higher Li-ion insertion voltage of around 3.5-4 V[110]. Compared to other rechargeable alternatives, LiBs can have an energy density nearly 300 watt-hours per kilogram (Wh/kg) and have a much longer lifespan[109,115]. However, LiBs can have disadvantages, the most prominent of which are safety concerns regarding materials used.

Liquid electrolytes are typically used due to high ionic conductivity and interfacial wettability. However, these materials are limited to lower temperatures, as the solvents used have low boiling points and are highly flammable[116–118]. When cells are overheated, overcharged, or experience internal defects, effects such as thermal decomposition can result in a short circuit and an increase of temperature and pressure within the cell[119]. This can result in thermal runaway, a

process in which the battery cell reaches a critical temperature where decomposition reactions feed further into the increase in temperature. When the temperature of the cell increases to around 80°C, the anode material begins to decompose and break down in an exothermic reaction. As the temperature increases further (100°C - 130°C), the electrolyte begins breaking down and generating various gases. Near 120°C, the polymer separator can melt, causing an internal short circuit to further generate heat. Above this temperature, the cathode can break down and generate more oxygen, driving the cell towards combustion and failure. The oxygen generation in these reactions makes this process self-sustaining, as it promotes heat generation and decomposition of the components, which further generate oxygen. This leads to thermal runaway and possible failure, where the cells swell, rupture, leak, or ignite and cause an explosion. Thermal runaway propagation can also occur, where the heating of one cell in a battery leads to overheating in neighboring cells as well, furthering this process until the entire battery ignites[116,120–122].

This thermal runaway has led to many cases where LiBs have ignited or exploded, leading to potentially catastrophic results. According to the Federal Aviation Administration, between March 3rd, 2006 and September 19, 2023, there have been 484 verified incidents related to LiBs involving smoke, fire, or extreme heat[123]. 53 of these incidents occurred in 2023 alone. Since 2019, at least 19 deaths and over 300 injuries have been reported that were related to LiB fires in New York City[124,125]. Different methods have been explored to minimize the risks of thermal runaway and battery fires. For instance, flame retardants have been added to the electrolyte to improve thermal stability with minimal performance loss[122,126]. Different battery materials can increase the thermal runaway onset temperature. For example, the polymer separator melting can result in short circuiting of the cell and increase thermal runaway. By changing this material, such as from polyethylene to polypropylene, the melting temperature can increase from 140°C to 160°C and

reduce the likelihood of thermal runaway. Another method which can be explored is a change in the battery design to limit thermal runaway propagation, such as by increasing the gap between cells. Fail-safe mechanisms such as vents and thermal fuses have also been explored[122]. For LiBs to be utilized in larger energy-storage devices for applications such as electric vehicles, the overall safety and performance needs to be improved.

1.3.1 Lithium garnet solid electrolytes

One method that is being explored to reduce risk of flammability is the transition from liquid electrolytes to solid electrolytes (SE) [113,127,128]. SEs have been explored for all-solid-state batteries (ASSB) and have also been utilized in hybrid electrolytes in conjunction with existing LEs. Typical SEs include polymer electrolytes or ceramic, such as sulfide-based and oxide-based electrolytes. One example which is explored in this work is $Li_7La_3Zr_2O_{12}$ (LLZO). LLZO has a garnet structure composed of ZrO_6 octahedra and LaO_8 dodecahedra, while Li ions (Li^+) and Li vacancies (V_{Li}) are located in the interstices of the framework structure[129]. LLZO SEs can exhibit a high ion conductivity of up to 10^{-3} S/cm, reaching levels that are comparable to existing LEs [128,130,131]. A higher electrochemical potential offers flexibility when choosing cathode materials, which can increase the overall energy density of the battery [128]. One of the more important features of LLZO SEs is the chemical stability of LLZO against high-capacity Li metals, which allows for Li to be used as the anode material in ASSBs instead of the traditional graphite anodes [128]. The solid-state of these electrolytes allows for large-scale battery devices to be reduced in size while still maintaining a high volumetric energy density. This is due to how batteries containing SEs can be assembled directly in layers as opposed to LE cells, which require additional parts to seal and isolate each individual cell [128,130,132].

To best utilize LLZO SEs, certain challenges need to be overcome. Improving the ionic conductivity further supports the use as SEs, and decreasing the processing temperatures during synthesis can enable a wider range of electrode materials and applications that require lower temperatures to function. One method that can tune the ionic conductivity in LLZO is by altering the crystal structure. LLZO has two crystal structures: cubic and tetragonal, shown in Figure 1.11.

The cubic phase (*c*-LLZO) exhibits a higher ionic conductivity (~10^{-4} S/cm) when compared to the tetragonal phase (*t*-LLZO), which generally exhibits a conductivity of around 10^{-6} S/cm [128–130].

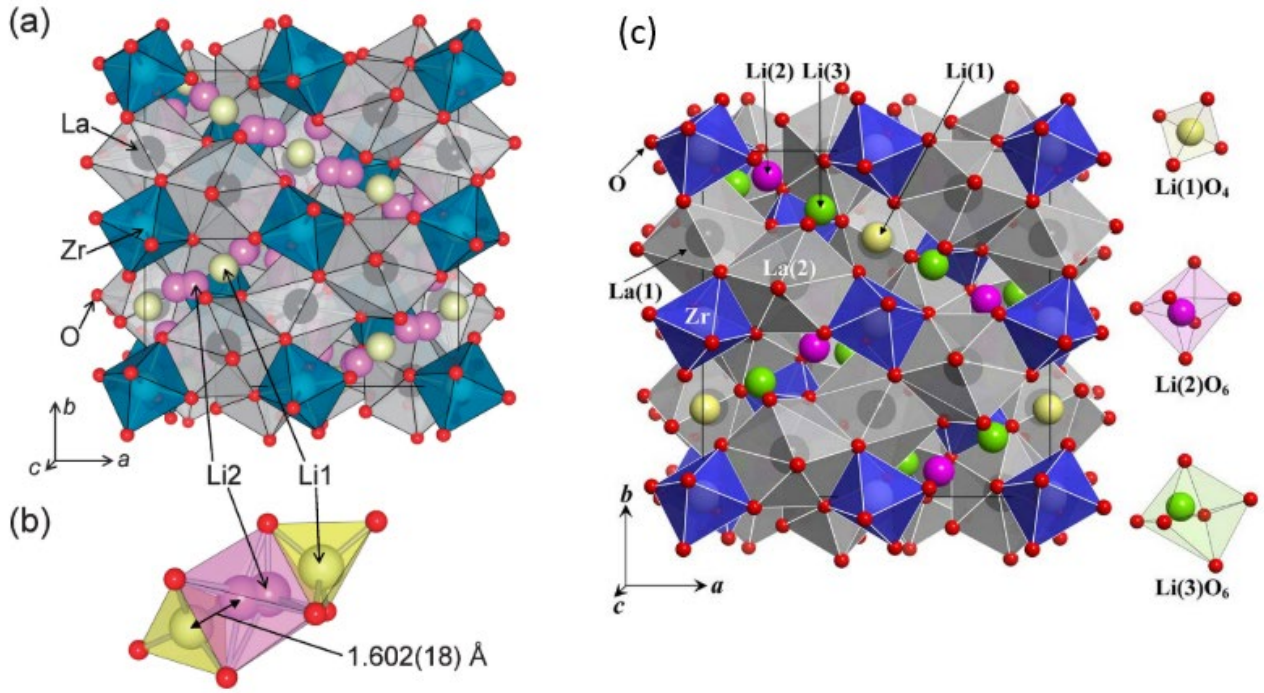

Figure 1.11 (a) Cubic LLZO with (b) Li1 and Li2 sites in the lattice. (c) Tetragonal LLZO phase[129,133].

The increased conductivity in *c*-LLZO originates from the uniform movement of Li^+ ions in the *x, y,* and *z* directions, while Li^+ ions only exhibit movement along the *x* and *y* directions in *t*-LLZO. In addition, the different distributions of Li^+ ions also affect the conductivity. *t*-LLZO has an order Li sublattice, where nearly all the 56 Li lattice positions are occupied. In contrast, the *c*-LLZO phase has 120 possible Li sites, where the Li sublattice is disordered and there is only partial occupation of the Li sites[128,129,133]. This can be seen in Figure 1.12, where g is the occupancy value for each Li site. The increase in Li sites and Li disorder in the *c*-LLZO phase results in increased Li migration when compared to the *t*-LLZO phase. The Li loop seen in Figure 1.12a can link with

other loops to form a three-dimensional Li-ion migration pathway with increased Li-ion migration. The numerous Li-ion sites with partial occupancy allow the Li-ions to migrate through the crystal structure more freely than in the ordered, fully occupied *t*-LLZO phase[128,129].

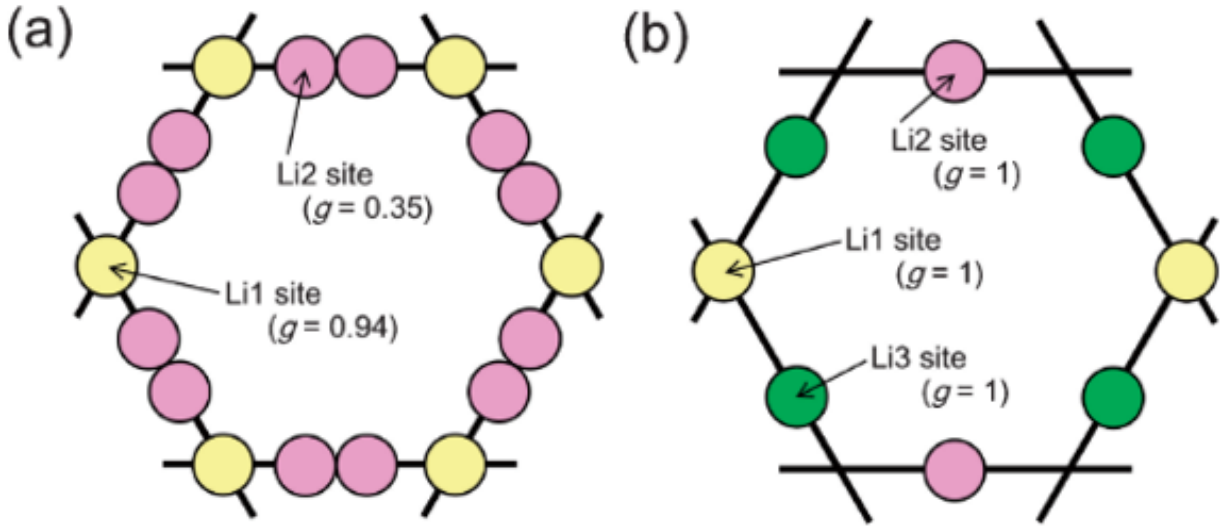

Figure 1.12 (a) Cubic Li site with g occupancy. (b) Tetragonal LLZO phase with g occupancies[129].

t-LLZO is more thermodynamically stable at room temperature (RT) compared to *c*-LLZO due to the ordered nature reducing the Coulombic repulsion among Li^+ ions[134]. However, due to the increased ion conductivity of *c*-LLZO, the cubic phase needs to be stabilized over the tetragonal phase. One method that is used to stabilize the cubic phase is through the doping of ions. Doping develops disorder at the Li and V_{Li} sites in the lattice, increasing the configuration entropy and reducing the Gibbs free energy of *c*-LLZO. This stabilizes the c-LLZO phase over the *t*-LLZO phase [128,135,136]. Common doping elements used are Al^{3+} and Ga^{3+} doped into the Li^+ site, Sr^{2+} and Nd^{3+} doped into the La^{3+} site, or Ta^{5+} doped into the Zr^{4+} site [128,136–139]. The doping of these elements has been shown to increase Li disorder and stabilize the *c*-LLZO phase at RT.

1.3.2 Lithium garnet thin films

Bulk ceramics are often synthesized using co-sintering, which occurs at high temperatures of around 1,050°C, to create macroscopic bulk bodies of ceramic LLZO. Reducing the processing temperature minimizes the evaporation of Li and reduces the reactivity between LLZO SEs and electrode materials, opening a broader range of candidates for electrode materials that was previously limited by the high processing temperature[128,130,137]. One method explored uses LLZO thin films, which decreases the processing temperature by over 400°C while maintaining the *c*-LLZO phase, high Li conductivity, and reducing the thickness down to nanometer scale[137,140]. In addition, LLZO thin films also offer opportunities in artificial intelligence, neuromorphic computing, and smart sensing[130,141].

LLZO thin films have been synthesized using methods such as chemical vapor deposition[142,143], sol-gel methods[144,145], and physical vapor deposition techniques[137,140,146]. However, the majority of LLZO films exhibit a room temperature conductivity that is orders of magnitude lower than their bulk counterparts, typically around 10^{-8} – 10^{-6} S/cm. In order to be utilized effectively for energy storage and other high energy density applications, the ambient conductivity needs to be improved. As mentioned previously, stabilizing the *c*-LLZO phase via elemental doping results in a higher ionic conductivity. This is done by doping the material and can vary depending on the deposition temperature[136,137]. Another method of improving the ionic conductivity is to increase the lithium content in the LLZO SE. During the vacuum deposition and annealing process of the films, Li loss can occur, reducing the conductivity, which can lead to unwanted phases. To solve this issue, additional Li can be introduced into the film during deposition. This has been done by either co-sputtering with two targets simultaneously or by using a multilayer deposition process with two alternating targets. Co-sputtering with a LLZO target and

Li_2O target created films which exhibited high ionic conductivities up to 1.9 x 10^{-4} S/cm[146]. A group from MIT under Professor Jennifer Rupp synthesized multilayer films by including layers of Li_3N in between layers of Al-doped LLZO. The LLZO films produced after deposition and annealing at 660°C showed the *c*-LLZO phase with an ionic conductivity of 2.9 x 10^{-5} S/cm[128]. Introducing additional Li during the deposition process produces LLZO thin films that are thin and dense while exhibiting high Li conductivity compared to typical LLZO films, allowing for the implementation of these LLZO thin films as fast Li-conducting SEs in ASSBs and other device structures[137,146].

Another important factor to consider when utilizing LLZO as a solid electrolyte is the interface between LLZO and the electrodes chosen. Li metal is considered the best anode material due to its low redox potential and high capacity[147]. However, challenges exist relating to the interface between LLZO and Li metal. LLZO is susceptible to forming contaminates on the surface after exposure to ambient conditions[128,148–150]. The surface contaminants, namely Li_2CO_3 and LiOH, are insulators and prevent the SE and Li metal from forming physical contact, decreasing lithium wettability. This results in high interfacial resistance of ~10^3 Ω in the films[128]. The inhomogeneity of the current distribution due to the poor interface can also lead to dendritic growth of Li metal during cycling, causing a short circuit to occur[128,151,152]. Methods to enhance physical contact and increase lithium wettability have been explored to reduce the interfacial resistance. Depositing a capping layer of a material that wets Li metal well can improve Li wettability, as does removing the surface contaminants, often done through polishing or heat treatment[128]. A more recent approach to improving Li wettability involves LE soaking[148–150].

LE soaking involves immersing the LLZO electrolyte in an organic solution which contains $LiBF_4$. This was first explored by Besli et al. using LLZO powders and pellets. Samples exposed

to air for three days were examined using X-ray absorption spectroscopy (XAS) before and after soaking the samples in the $LiBF_4$ solution for 16 hours. The soaked samples exhibited reduced Li_2CO_3 absorption features compared to the exposed samples, indicating that the surface contaminant layer of Li_2CO_3 was removed[148]. This was further confirmed using XRD and Raman spectroscopy. Electrochemical measurements showed significant improvement in the cycling behavior and impedance of LLZO pellets that were soaked in the LE[148]. This process enables the removal of surface contaminants and increases the Li wettability and interfacial contact for LLZO SEs. While these measurements were done using LLZO in powder or pellet form, there are no known reports on the LE soaking of LLZO thin films.

As previously mentioned, Li metal is a highly desirable candidate for use as an anode in Li-ion batteries. The use of LLZO as a SE enables Li anodes due to the chemical stability. In addition to being utilized in ASSBs, LLZO can be utilized in hybrid-electrolyte cells to further enhance the performance in batteries. In this scenario, a LE is inserted at the SE/cathode interface to enhance Li-ion transfer kinetics[153,154]. The stability of the solid-liquid electrolyte interface (SEI) is crucial for the success of the hybrid electrolyte cells, as it can impact the ion conductivity and reduce its effectiveness[154]. Previous reports on the SEI have investigated bulk LLZO immersed in a LiTFSI or $LiPF_6$ LE to uncover the composition of the SEI layer that forms. The main component of the SEI in these hybrid electrolytes is believed to be LiF, which generates and grows into a thick layer which prevents LE permeation into the SE[154–156]. Using LLZO thin films immersed in a LE can allow further insights into the composition of the SEI and provide a better understanding of the mechanisms behind the SEI formation and its effects on the ionic conductivity in hybrid electrolyte cells[127,157,158].

1.3.3 Lithium cobalt oxide cathodes

In addition to the solid electrolyte in batteries, the performance and safety of Li-ion batteries can be improved by increasing the understanding of the structure and physicochemical properties of elements such as the electrode materials used. In Li-ion batteries, the conduction of the Li^+ ions through the electrodes and electrolyte materials is of great importance. However, the addition and removal of lithium can affect the structure and properties of the cathode and electrolyte material. In addition, the interface between the varying electrode materials and electrolytes can also impact the power density and capacity retention of the Li-ion batteries[159,160]. An integral component to Li-ion batteries is the cathode material used. $LiCoO_2$ (LCO) has been extensively studied as a cathode material due to its high energy density, cycle life, and reliability[159,161]. This, however, can be affected by microstructure changes that occur during cycling and when in contact with the electrolyte.

The interface between LCO and an electrolyte (solid or liquid) has been studied previously. When a liquid electrolyte is used with the LCO cathode and electrochemically cycled, kinks can form in the CoO_2 layers, which can hinder Li translation between the electrode and electrolyte[159]. Delithiation and lithiation of the films can also induce structure changes, where the trigonal layered structure changes to a spinel structure after Li extraction near the interface[159,162]. When using a solid electrolyte LLZO, the migration of Co into the LLZO can also result in additional phases forming at the interface[163]. While understanding the evolution of the interface is important, it is also vital to understand how the delithiation of the cathode LCO can affect its structural properties. Understanding how the LCO structure evolves under delithiation can provide further insight into the effects that the interface with a solid or liquid electrolyte will have on the overall performance.

Chapter 2. Experimental approach

2.1 Thin film synthesis with pulsed laser deposition

Thin film materials can be synthesized through a variety of methods, such as chemical deposition techniques, sol-gel processing, or physical vapor deposition. These categories can be divided into other more specified techniques. For instance, physical vapor deposition involves vaporizing a solid material and depositing that material onto a substrate. This is done through methods such as thermal or electron beam evaporation, magnetron or ion beam sputtering, or through pulsed laser deposition (PLD). The primary focus of this thesis is of metal oxide thin films that have been deposited onto substrates by using PLD[164].

Among the physical deposition methods, PLD offers numerous advantages. PLD allows for a high degree of control over material properties due to the large number of parameters that can be controlled. It offers the broadest range of material compositions that can be deposited and is effective for materials with complex chemistries and structures[165]. The PLD process can be divided into three major processes:

- Laser-target interaction
- Plume formation and propagation
- Film deposition and growth

PLD uses the energy of a pulsed laser in order to vaporize a target material. To achieve this, a high-energy laser is focused on a target material in a vacuum chamber, creating a plasma plume which deposits the material onto a chosen substrate. The laser that is used for these films is a KrF excimer laser with a wavelength of 248 nm[166]. Excimer lasers induce an excited state in krypton atoms through a high voltage discharge, causing them to react with the fluorine gas and produce

krypton fluoride. This temporary complex then relaxes back to its lower energy ground state, releasing photons in either spontaneous or stimulated emission[167].

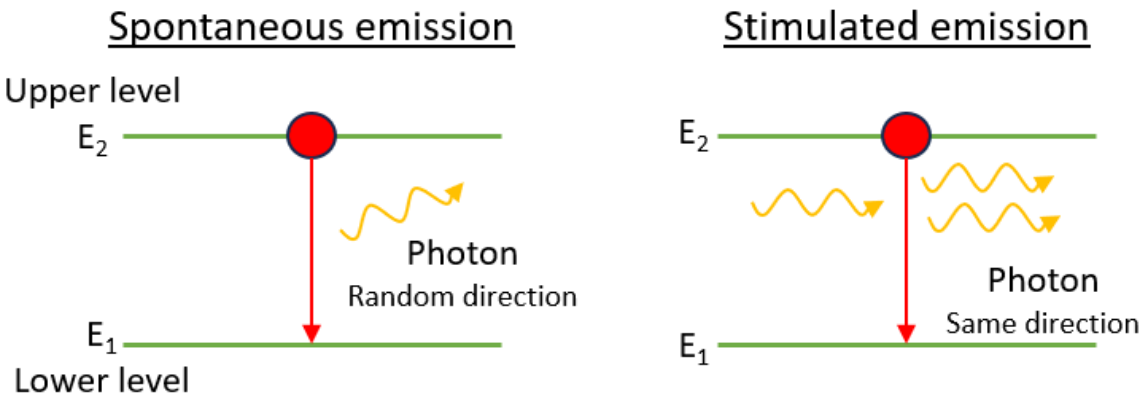

Figure 2.1 Spontaneous and stimulated emission of photons to produce laser pulses for PLD.

Spontaneous emission results in random emission, while stimulated emission occurs when the excited electron interacts with other photons and results in emitted photons with identical properties, shown in Figure 2.1. This ground state complex then dissociates into the unbound krypton and fluorine atoms[166]. This process results in a laser pulse of 248 nm which can then be directed towards the PLD system. Other lasers that can be used for PLD depositions include Nd:YAG (355 nm) and ArF (193 nm).

During the laser ablation process, both thermal and non-thermal processes occur in order for the laser pulse to remove the target material. Initially, the incident photons in the laser pulse penetrate the target material and cause the electrons in the material to transition to an excited state. The relaxation of the excited electrons transfers heat to the system, increasing the temperature to several thousand Kelvin and causing localized melting and instantaneous vaporization of the target material[164].

The ablated target material then moves towards the substrate, interacting with the gaseous environment in the chamber. The shape of the plasma plume is affected by the pressure inside the chamber. An increase in pressure increases the collisions between plume particles and gas molecules, leading to a decrease in the energy of the particles[164].

Once the plasma plume particles reach the surface of the substrate, they become adsorbed onto the substrate. Adsorbed particles diffuse along the surface of the substrate and can either form nucleation sites and begin film growth, or they can further evaporate from the sample surface during desorption. The temperature of the substrate during depositions can affect whether the adsorbed particles form nucleation sites or evaporate further. Lower growth temperatures can reduce the mobility of the target species on the surface of the sample and limit diffusion among favorable sites on the surface. On the other hand, higher temperatures increase the energy of the particles promoting diffusion, but also promotes re-evaporation of the particles. If the initial adsorbed particles form nucleation sites, then the film can continue to grow further[164,168]. During the deposition, there are three main modes that define how a film grows[168] (Figure 2.2):

- Frank-Van der Merwe (layer-by-layer): Strong interactions between atoms and surface result in layers forming.
- Volmer-Weber (island growth): High atom-atom interactions result in island-like formations growing.
- Stranski-Krastanov (layer and island): While the film begins growing layer-by-layer, external forces can result in islands forming.

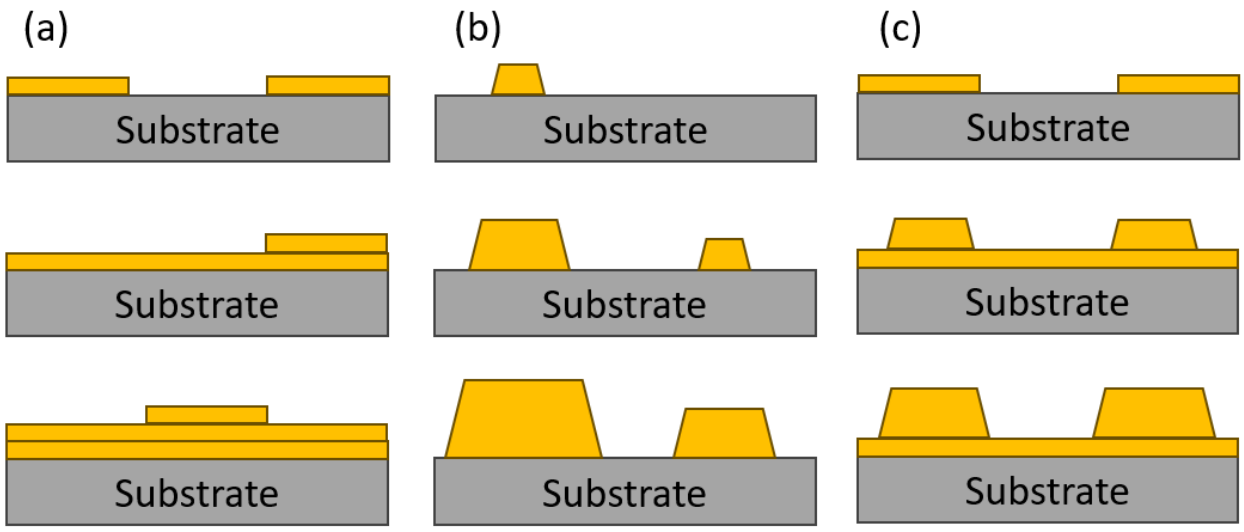

Figure 2.2 Three modes of thin film growth. (a) Frank-Van der Merwe (b) Volmer-Weber (c) Stranski-Krastanov

PLD is advantageous because of the many parameters that can be controlled to affect the quality of the deposition and the properties of the resulting films. These can include:

- Laser parameters: laser pulse energy, pulse duration, laser frequency, laser spot size, laser spot shape
- Chamber parameters: growth pressure, target-substrate distance (fixed)
- Substrate parameters: lattice constant, orientation, sample preparation, sample adhesion method, growth temperature.

Varying these parameters can affect the film deposition quality by altering how the laser interacts with the target material, the plume formation, and deposition of the material and the growth of the film on the substrate. An important parameter to note is the growth pressure of the chamber during depositions. Because the films deposited are metal oxides, oxygen gas is added into the chamber to provide oxygen for film growth. The quality and stoichiometry of the films depends greatly on the amount of oxygen present during deposition. Lack of ambient oxygen leads to off-

stoichiometry and the formation of oxygen vacancies in the film. Increasing the oxygen pressure also increases the interactions between the plume particles and gas particles, which affects the plume size and the resulting formation and quality of the films[4,169,170].

2.1.1 The PLD system

The thin film deposition occurs inside a high-vacuum growth chamber (Figure 2.3).

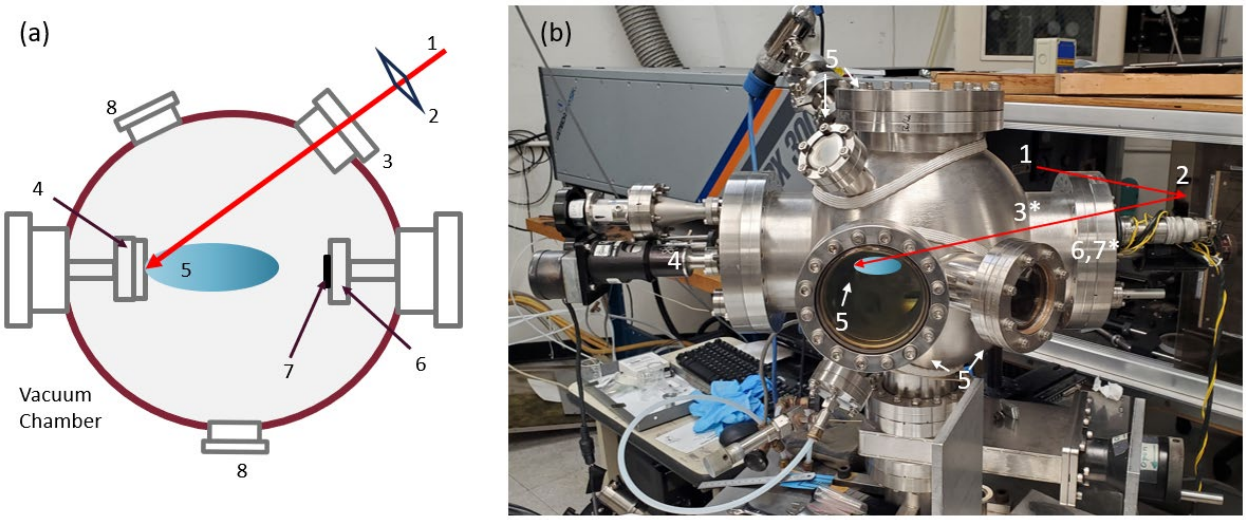

Figure 2.3 (a) Diagram and (b) image of PLD chamber. Labels indicate: 1 - Laser source; 2 - Laser optics; 3 - Laser window; 4 - Target carousel; 5 - Laser plume; 6 - Substrate heater; 7 – Substrate; 8 - Viewing ports. Red line indicates laser path.

The deposition process is as follows:

1. The KrF excimer laser generates a laser pulse with a wavelength of 248 nm.
2. The laser pulse exits the laser system.
3. The optics, which includes external slits, mirrors, and lenses, constrain, direct, and focus the laser beam to the appropriate size and dimensions.
4. The laser beam passes through a single side anti-reflection coated fused silica laser window into the deposition chamber and strikes the target.
5. The PLD target with the desired material or composition is attached to a target holder. The target holder is connected to a target carousel to allow for multiple targets to be loaded simultaneously, enabling different materials to be deposited. The target holder rotates the

target so that the laser does not strike the same point, which can create cavities in the target material.

6. Substrates are attached using either silver paste or with metal clamps to a sample holder which is temperature controlled through either resistive heating or a diode laser.
7. Oxygen gas is flowed into the chamber through valves to control the oxygen partial pressure during the deposition.
8. The laser ablates the PLD target, creating the laser plume which interacts with the injected gas particles.
9. The laser plume deposits the target material onto the heated substrate.

In addition, other viewing ports located around the chamber allow for observation of the plume and substrate during the deposition. The laser is focused using optics to form a laser spot size which was typically around 1mm x 3mm for these depositions. Along with the laser energy, the laser spot is important as it affects a parameter called laser fluence, which is the energy per unit area that ablates the target material. The laser fluence that was used for these depositions varied by chamber and was typically between 1 J/cm^2 to 1.5 J/cm^2.

Three different PLD systems were primarily used for the metal oxide depositions: two systems are located in the Quantum Materials Center (QMC) in the John S. Toll Physics building, and the third is located at the Keck laboratory in the Jeong H. Kim Engineering building. The two PLD systems in the QMC utilize an LPX 300 excimer laser. In both chambers, a roughing pump and turbo pump are used to create a high-vacuum environment in each chamber with a base pressure between $5*10^{-6}$ torr and $1*10^{-7}$ torr. Two flanges opposite one another contain the target carousel and substrate heater, respectively. Targets are mounted using silver paste onto target holders that are aligned horizontally. Substrates are mounted onto a substrate heater using silver

paste or metal clamps, which then heats the substrate using a resistive heater to the desired deposition temperature. This orientation results in a horizontal plume during laser ablation. During the deposition, oxygen gas is flowed into the chamber to raise the oxygen partial pressure in the chamber to a desired level. This aids in the formation of oxide films and reduces the oxygen vacancies that can form at high temperatures. Two main chambers were used in the QMC, hereby designated as the lithium chamber and nickelate chamber (Figure 2.4). The lithium chamber is used primarily for materials which contain lithium, such as lithium cobalt oxide (LCO) and lithium garnet. The nickelate chamber can be used for a variety of materials and contains a programmable shutter mechanism that allows for combinatorial thin films to be synthesized.

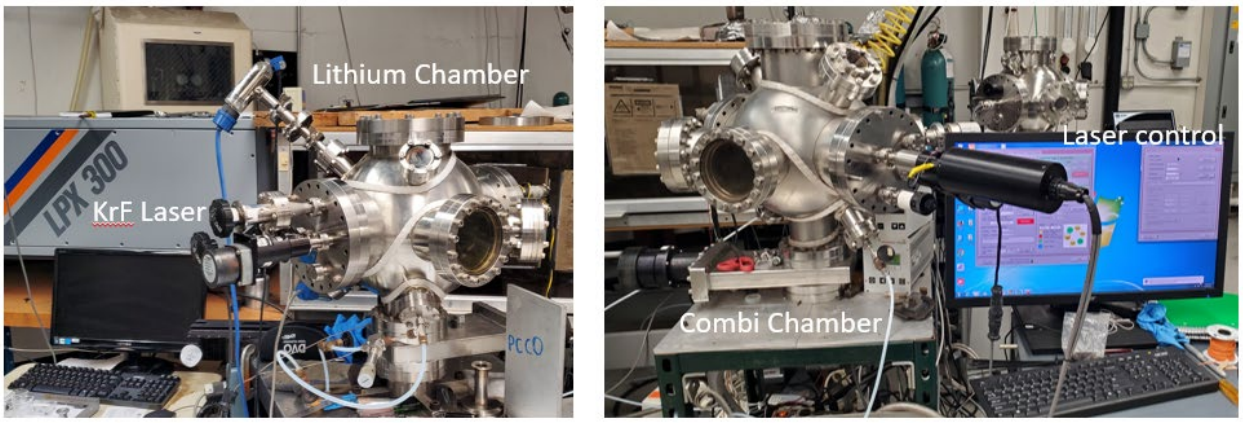

Figure 2.4 (a) Lithium chamber and (b) nickelate chamber in the QMC PLD lab.

Unlike the QMC PLD systems, the system in the Keck lab utilizes a load-lock system in order to maintain ultra-high vacuum pressure in the main deposition chamber (Figure 2.5). For this system, substrates are mounted onto a metal plate and placed into a sample holder. The sample holder can then be placed upside down in the load-lock chamber to be pumped down to high vacuum before being transferred into the main chamber. A diode laser is used to heat the sample, unlike the resistive heater used in the QMC systems. A small opening in the back of the sample holder allows the laser to directly heat the back of the metal plate, heating the substrate to the

desired temperature. The temperature of the substrate is controlled by the voltage applied to power the laser. The targets in the Keck PLD system are mounted on the bottom of the chamber, directing the plume upwards onto the surface of the sample. The excimer laser pulses are directed into the chamber from above instead of horizontally like the QMC chambers. The load-lock system allows for the main deposition chamber to remain at ultra-high vacuum pressures of 10^{-9} torr, resulting in higher quality films with minimal contaminants.

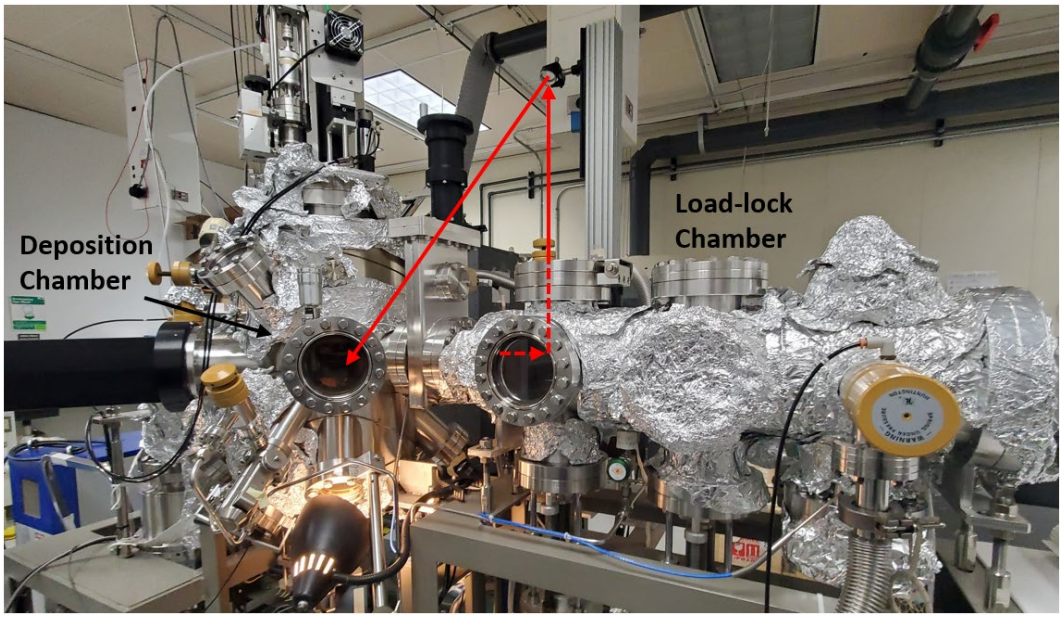

Figure 2.5 Keck PLD chamber with attached load-lock chamber. Dashed red lines indicate obscured laser path behind chamber. Solid red line indicates continued laser path into chamber.

Before the metal oxides are deposited onto the substrate surface, the targets used are pre-ablated with a masking shutter for up to 10 minutes. This removes any contaminants that may have accumulated on the target surface. After pre-ablation, the masking shutter is removed, and the metal oxides begin depositing on the substrate surface. The advantage of using PLD to deposit thin films is the amount of control over the deposition parameters. These factors can affect the thickness of the film, the crystallinity, surface roughness, phase, and overall quality of the films deposited. Multiple depositions are run in order to determine the optimal conditions and parameters for the

films grown. After each deposition, samples are removed from the chamber and stored in either a desiccator or vacuum sample box to limit further oxidation or degradation of the films before characterization.

2.1.2 Thin film deposition procedures

For rare-earth nickelates, $LaNiO_3$ was deposited onto $SrTiO_3$ (STO) or $LaAlO_3$ (LAO) substrates with (001) orientation in the QMC and Keck PLD chamber. Prior to each growth, substrates were scribed using a diamond tipped cutter and cut into 5 mm x 5 mm, 5 mm x 10 mm, or 10 mm x 10 mm samples as needed. Cut substrates were then cleaned using a four-stage acetone-methanol-isopropanol-deionized water cleaning process with a sonicator. In this process, samples were immersed in the liquid and sonicated for five minutes at each step. Samples were washed with deionized (DI) water and dried with nitrogen gas between each step. This process removed any particles or contaminants on the surface of the substrates after cutting the substrates. Cleaned samples were examined under an optical microscope to ensure that the surface was free of any particulates. Initial depositions of $LaNiO_3$ were done in the QMC nickelate chamber. However, later depositions were moved to the Keck chamber due to issues with laser gas levels and issues with the substrate heater. Substrates mounted in the QMC nickelate chamber were fixed directly onto the heating stage using silver paste. The silver paste was then cured at 100 °C for five minutes to adhere the substrate. The heater flange was then loaded into the PLD chamber and the chamber was pumped to high-vacuum levels of 10^{-7} Torr. The $LaNiO_3$ films were deposited at 650 °C and an oxygen partial pressure of 150 Torr with a laser frequency of 10 Hz for 20 minutes.

Substrates that were deposited using the Keck chamber were mounted onto a metal backing plate using silver paste, which was then heated to 100 °C for five minutes to ensure good contact and adhesion to the plate. The metal backing plate was then placed into the sample holder along with a metal mask which covered half of the substrate, ensuring that the film is only deposited on one half of the 5 mm x 10 mm substrate. This provided a region of exposed substrate which is used as an insulating barrier for gating device experiments. Substrates were then placed into the load-

lock chamber and pumped to approximately 10^{-7-} Torr before being inserted into the main deposition chamber. Before the deposition, the substrate was pre-annealed at 930 °C with an oxygen partial pressure of 5 x 10^{-6} Torr to obtain atomically flat surfaces[171]. During the deposition, $LaNiO_3$ was deposited at 600 °C with an oxygen partial pressure of 250 mTorr and a laser frequency of 6 Hz. Samples were deposited in twelve sets of 2,000 pulses for a total of 24,000 pulses. The samples were then removed using the load-lock chamber for characterization and electrical measurements.

$LiCoO_2$ films were deposited onto Nb-doped STO (111) and STO (001) substrates in the QMC PLD system. Films were deposited in the QMC lithium chamber over a period of 80 minutes at 700 °C with an oxygen partial pressure of 150 Torr and a laser frequency of 10 Hz. On some samples, a layer of $SrRuO_3$(111) was deposited as a buffer layer to provide electrical contact to $LiCoO_2$. This was done in the Keck PLD chamber by another member of the group before being transferred to the QMC lithium chamber for LCO depositions.

An advantage of using PLD for thin film depositions is the ability to change the targets that are being ablated. This allows for different materials to be deposited on a single substrate in situ, enabling the deposition of multilayered films and of combinatorial spreads. Multilayered films are made by alternating between different targets to create individual layers of a target material. By depositing at high temperatures or annealing the deposited films, the layers merge together to form a single uniform film. This enables easy composition tuning by adjusting the thickness of each layer and the number of layers that are deposited in a film. Multilayered Ta-doped LLZO/Li_2O films were made by ablating two targets, $Li_{6.5}La_3(Ta_{0.55}Zr_{1.45})O_{12}$ (Ta-LLZO) and Li_2O, in alternating layers. The thin films were deposited on $Gd_3Ga_5O_{12}$ (GGG) or MgO substrates with either 5 mm x 5 mm, 5 mm x 10 mm, or 10 mm x 10 mm dimensions. Substrates were cut in the

same manner as those for $LaNiO_3$ using a diamond tipped scribe. After cutting, the substrates were gently wiped with an acetone-soaked cotton swab to remove particulates. MgO substrates were not washed with the same process to minimize degradation of the films due to exposure with solvents. Substrates were then loaded onto the lithium chamber heater using either silver paste or with metal clamps. Metal clamps were used in order to minimize any contaminates that may be present in future NR and liquid electrolyte soaking experiments, where the presence of silver paste can contaminate the measurements. The lithium chamber was then brought to a high-vacuum level of around 10^{-6} Torr and was allowed to pump down at least overnight to purge the chamber from any possible air contaminants before deposition of the multilayer films. The initial and final deposited layers were Ta-LLZO to ensure good lattice match and to limit Li loss to ambient exposure. The number of pulses for each layer and the number of layers can be varied between depositions to influence the thickness of the Ta-LLZO or Li_2O reservoir layers and affect the overall Li content in the film. After deposition, films were kept in the high-vacuum PLD chamber until needed for characterization, after which they were stored in a vacuum sample container to limit exposure to ambient conditions to reduce degradation of the films.

2.2 EDLT devices

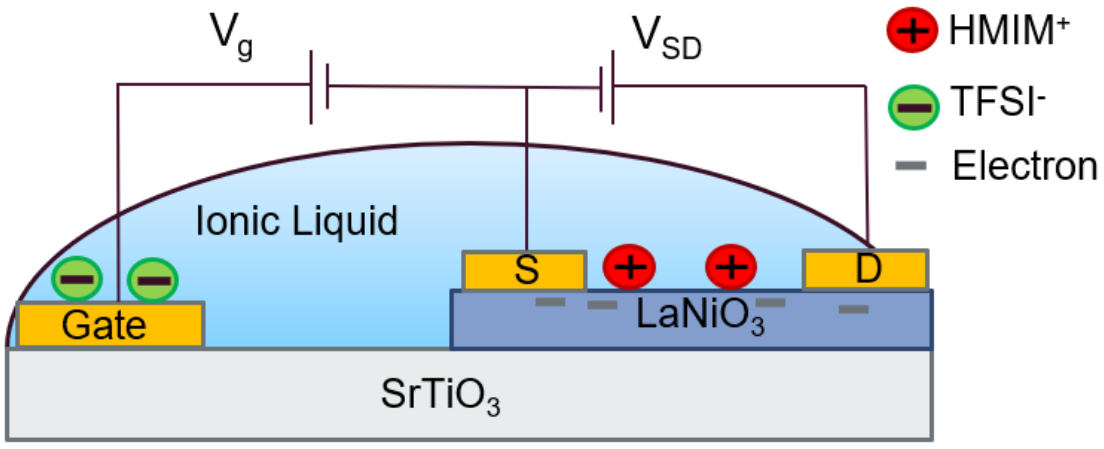

Figure 2.6 Diagram of ionic liquid gating device fabricated.

EDLT devices were fabricated using the $LaNiO_3$ thin films on STO substrates. The EDLT devices followed the principle shown in Figure 2.6. The ionic liquid used was 1-Hexyl-3-methylimidazolium bis(trifluoromethylsulfonyl)imide (HMIM-TFSI). Three device designs were used for IL gating experiments. In the first design, 5 mm x 5 mm $LaNiO_3$ films with two-point probe contacts were immersed in the IL along with a separate Pt or Cr/Au film as a gate electrode. The second and third design used 5 mm x 5 mm $LaNiO_3$ films deposited on half a 5 mm x 10 mm STO substrate. In one design, Pt or Cr/Au contacts were deposited in a three-bar formation, where two longer bars acted as the source/drain electrodes and a separate bar deposited solely on the substrate acted as the gate electrode. In the third design, Al wires were directly bonded to the surface of the $LaNiO_3$ film and STO substrate to act as the source/drain electrodes and gate electrode.

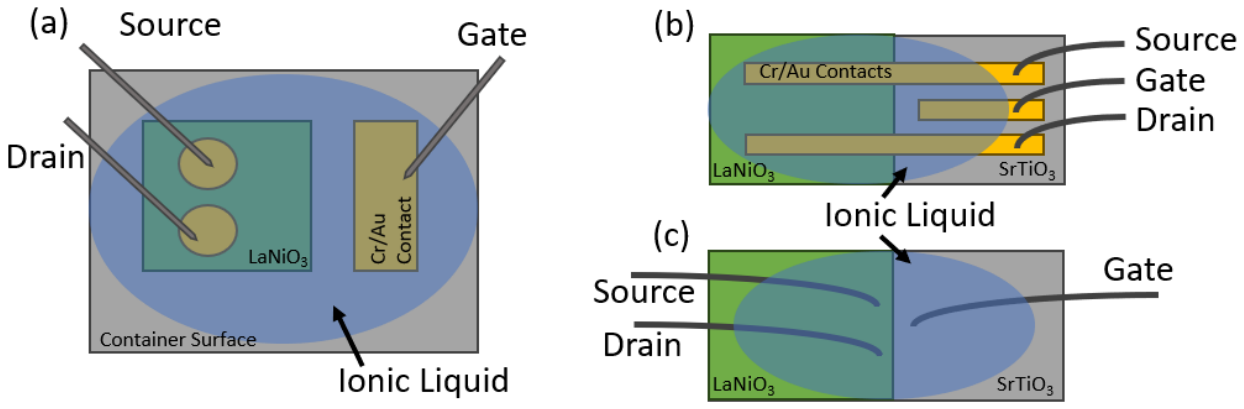

Figure 2.7 Three device designs utilized in IL gating. (a) Separate film and contact immersed in IL. (b) Half-deposited film with three-bar contact design. (c) Half-deposited film with direct wire bonding.

2.3 Liquid electrolyte soaking

Ta-LLZO film samples from UMD were transferred to a He glove box at NIST using a vacuum sealed bag with desiccants. The thin film samples were exposed to 3 mol/dm^3 $LiPF_6$/propylene carbonate (PC) electrolyte using Markez® O-rings to regulate the exposed area to solely the Ta-LLZO surface. The sample was exposed to the electrolyte for up to 65 hours, followed by rinsing of extra electrolytes with dimethyl carbonate (DMC). Chemicals were obtained from Kishida Chemical.

2.4 Thin film characterization

2.4.1 Structural characterization

Structural characterization of the deposited metal oxide thin films was performed at room temperature using multiple different characterization techniques. X-ray diffraction (XRD) and grazing-incident X-ray diffraction (GI-XRD) were used to determine the crystal structure and orientation of the deposited films, as well as any contaminate phases that may have occurred. The diffractometers that were used include a Bruker D8 Advance (D8) in the QMC, a C2/D8 Discover (C2) with an area detector in the X-ray Crystallographic Center (XCC), and a PANalytical X'Pert Pro MRD system (X'Pert) in the XCC.

The XRD measurements using the D8 were performed with a Cu Kα X-ray source with a wavelength of 1.54 Å. The D8 has an installed monochromator which removes interfering emission lines that can be seen in XRD patterns. The D8 utilizes a four-circle goniometer with XYZ motion, which allows for proper alignment of the samples before measurements are taken, which can be seen in Figure 2.8. Samples were aligned along the substrate peak in order to maximize the reflection intensity. With the substrate peak aligned, any additional peaks can be attributed to either the thin film growth or contaminant phases. It is possible that the sample can be so misaligned that no peaks appear if the sample is not aligned to the substrate peak. By aligning the sample to a known substrate peak, the chance of a film peak appearing during the XRD scans increases. This effect changes however, if the thin film is grown at an off angle when compared to the substrate orientation, as is the case for the Ta-LLZO films discussed later.

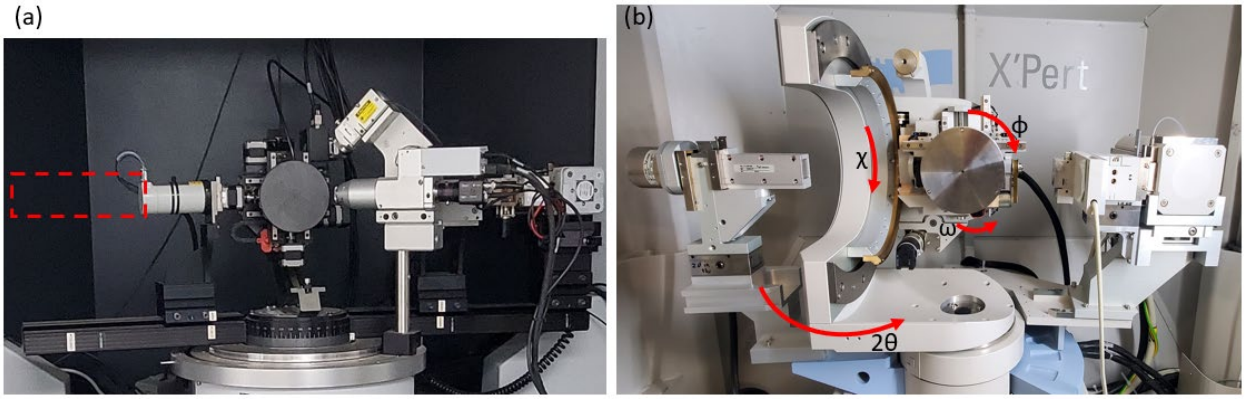

Figure 2.8 XRD instruments with four-circle goniometers. (a) QMC Bruker D8. Red dashed box indicates detector removed for maintenance. (b) XCC X'Pert with red arrows indicating χ, 2θ, ω, and φ movement.

The X'Pert XRD instrument in the XCC uses CuK_α sealed X-ray tube with a parallel beam W-Si mirror and has a similar four-circle goniometer. 2θ-ω scans were taken with a 2θ range of 20° – 80°. The X'Pert however, does not have a monochromator, and therefore also includes the $K\alpha_1$, $K\alpha_2$, Kβ, and Tungsten (W) $L\alpha_1$ lines. Reflection peaks provide information on the crystal structure and orientation of the films grown. According to Bragg's law, the reflection peaks are detected at specific angles for known materials and define the crystal structure of the material. Any deviations in peak position compared to reference values can indicate strain effects on the films. The shape of the peak and its full-width-half-maximum (FWHM) can provide insight into the quality of the film and the crystallinity of the film. Sharper peaks can indicate larger grains and can suggest epitaxy in the films. In addition to 2θ-ω XRD scans, GI-XRD was also utilized to obtain diffraction patterns of the deposited films. In the XRD geometry, the incident beam angle between the X-ray source and the film surface is the same as the angle between the sample and the diffracted X-rays. GI-XRD however, keeps the incident ω angle constant at a low grazing incidence angle of ω = 0.5° while scanning a wide 2θ range. This results in shallower penetration into the thin film (a few nanometers) and can reduce the effect of the substrate in the resultant

patterns[172,173]. The difference between XRD and GI-XRD are shown in Figure 2.9. One important distinction is that in Figure 2.9, the sample position is fixed while the X-ray source and detector move. However, in both the D8 and X'Pert, the X-ray source position is fixed, while the sample and detector move, defined by ω and 2θ, respectively. The alignment procedures are specified in Appendix A.1.

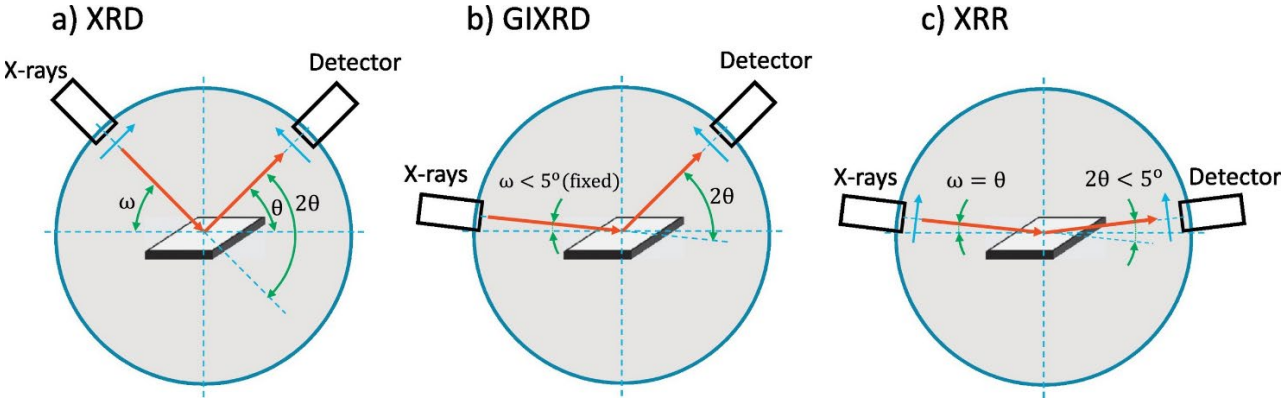

Figure 2.9 Schematic of (a) X-ray diffraction (XRD), (b) grazing incidence X-ray diffraction (GI-XRD), and (c) X-ray reflectivity (XRR)[173].

The C2 XRD instrument has a CuK_α sealed X-ray tube with a graphite Göbbel mirror and utilizes an area detector for measurements. For these measurements, samples are attached to a glass slide and placed horizontally within the measurement zone. This instrument does not allow for fine alignments of the sample, as the stage can only move in the XYZ directions. The reflections are detected by a general area diffraction detector system (GADDS) to form a spectrum of the reflected intensity vs 2θ angles, which allows for a wide range of 2θ and χ values to be measured simultaneously (Figure 2.10). The detector used is a Vantec 500 area detector for 2D diffraction. The area detector enables a large portion of the diffraction rings to be measured simultaneously, producing frames with a set 2θ and χ range which show the Debye rings produced by Bragg reflections. The area detector frame provides a quick insight into a material's crystallinity, composition, and orientation. Continuous Debye rings indicate a polycrystalline film, incomplete

rings can indicate texture, and individual spots suggest single crystal or epitaxial films. Integrating the area detector frame along the chi (χ) direction provides a standard intensity vs 2θ diffraction pattern, allowing for quantitative and qualitative analysis of the crystal structure.

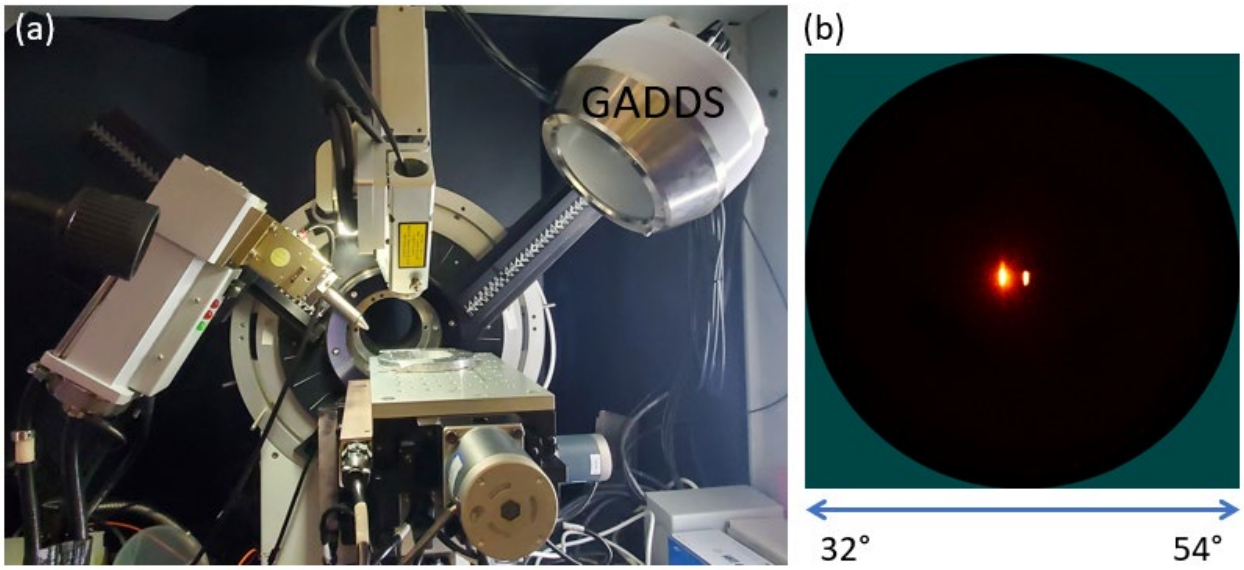

Figure 2.10 (a) XCC Bruker C2/D8 instrument with attached GADDS. (b) Generated diffraction frame with indicated 2θ range.

2.4.2 Surface and thickness characterization

Surface characterization was performed with atomic force microscopy (AFM) using a Digital Instruments Nanoscope V AFM instrument in the QMC. AFM involves scanning an AFM tip attached to a cantilever over a sample surface in a raster pattern. Attractive and repulsive forces between the surface and tip cause the tip to deflect towards or away from the surface. A calibrated laser beam reflected off the cantilever detects the cantilever deflection, recording any height changes on the surface of the film. AFM scans were then analyzed using Gwyddion to level the data, align rows, and calculate the Root Mean Square (RMS) value of the roughness. Line profiles were also obtained using Gwyddion. The lowest value of each scan image was set to zero.

Thickness characterization of the films was performed using three methods: scanning electron microscopy (SEM), atomic force microscopy (AFM), and X-ray reflectivity (XRR). SEM was performed in the Advanced Imaging & Microscopy Laboratory (AIM Lab) using the Hitachi SU-70 FEG SEM. Samples were cut in half to image the cross-section and measure the thickness of the films. This method was used for films with a thickness of around 200 nm, but showed inconsistency depending on how the samples were cut and oriented.

AFM was performed using a Digital Instruments Nanoscope V AFM in the QMC. For thickness measurements, films were deposited with a metal mask covering part of the substrate. After deposition, the mask was removed to leave an edge of the film exposed. This allows for rough thickness measurements to be taken. However, this is unreliable as the film edge can be affected by other factors, such as poor contact between the mask and substrate, which prevents a sharp edge and instead creates a gradual incline, making thickness measurements difficult.

Of the three methods used, XRR measurements were taken as the primary method to measure the thickness of films deposited. XRR is a non-destructive technique which measures the

specular reflection of X-rays. The specular reflection produces oscillations known as Kiessig fringes, which are due to the reflection of X-rays at each layer and the interference of X-rays reflected from different layers in the sample[174]. XRR was performed using the D8 and XPert instruments. Initial sample alignment was performed in the same manner as with XRD. 2θ-ω patterns were obtained with a 2θ range of 0.4° - 3°. This range allowed for density profiles to be modeled and fitted to the obtained XRR patterns. The software GenX 3 was then used to analyze the XRR patterns and estimate the thickness of the thin films by fitting simulated models. Multiple layers were defined by their composition, density, roughness, and thickness. By varying these parameters, a simulated model of the film was fitted to the obtained 2θ-ω pattern to obtain a density profile and estimate the total thickness[175].

2.4.3 Composition analysis

Determining the composition of the samples being deposited is vital to ensure that high quality metal oxide thin films are synthesized. If the composition of the films is off, then different phases or structures can be deposited instead of the desired phase. To analyze the composition of the film, we utilize wavelength-dispersive X-ray spectroscopy (WDS), energy-dispersive X-ray spectroscopy (EDS), and X-ray photoelectron spectroscopy (XPS). WDS and EDS are used to determine the elements that are present in the film and substrate, as well as their relative weight percent and atomic percent. This is used to confirm the composition of the film and ensure that the correct ratios are present, aiding in the formation of the desired phases. EDS is performed alongside SEM in the AIMLab, while WDS is performed at the Institute for Research in Electronics & Applied Physics (IREAP).

XPS is used to analyze the elements present as well as determining the valence state and vacancy concentration of the ions. This is performed by collaborators at the National Institute of Standards and Technology (NIST) using a Kratos XPS with a monochromatic Al Kα (10 mA, 15 kV) X-ray source with 20 eV pass energy. Charge neutralizer was used with a filament current of 1.8 A and charge balance of 3.5 V. Sputtering of Ta-LLZO samples was carried out with an Ar^+ gun with an energy of 2 kV over a raster area of 6 mm x 6 mm. The sputtering rate used for these samples was around 0.75 nm/min. To analyze the XPS data, CasaXPS is utilized with a Shirley background method[176]. Peaks obtained before sputtering were calibrated based on the carbon peaks at 284.8 eV as the reference[177]. Peaks after sputtering were calibrated using the O 1s peak of metal oxides at 529.5 eV, consistent with the strongest metal oxide peak position before sputtering.

NR can be used to characterize the structure of the solid electrolyte interface/interphase (SEI) by providing neutron scattering length density (SLD) profiles. Neutrons scattering is

advantageous because it is nondestructive and can penetrate thick samples, allowing multilayered structures to be characterized. Combining this with XRR allows for composition depth profiles to be generated. This is done by collaborators at NIST who are involved in the Ta-LLZO garnet film projects.

2.4.4 Electrical characterization

Characterization of the thin film samples' electrical properties, such as resistivity, were performed in two environments: in-air or in-vacuum. Contacts were deposited onto the surface of each sample using a Metra Thermal Evaporator or the AJA ATC Orion 8 Sputtering system in the UMD Fablab. Either gold or platinum was chosen as the contact material, with a 10 nm chromium adhesion layer. Contacts were deposited in either two-point or four-point probe geometry for resistance measurements. In-air measurements were performed at room temperature using a probe station in Dr. You Zhou's lab.

In-vacuum measurements were performed using a 9 tesla (9T) PPMS system from Quantum Design in the QMC. [Image of PPMS System] The vacuum level during measurements was kept constant at around ~10 Torr. Samples for measurement were loaded onto a PPMS resistivity puck using grease or GE Varnish. Once the sample was secured, wire bonding was performed in order to connect the samples to the PPMS pads for measurement. While the 9T PPMS was able to independently measure temperature-dependent resistivity of the samples, it is unable to apply a separate gate voltage to the samples when used for IL gating experiments. To resolve this issue, Keithley SourceMeter SMU units were used separately as needed to measure the resistivity and apply a gate. Resistivity measurements using the Keithley units was carried out by applying a specified voltage range and measuring the current output. The resistance can be obtained using Ohm's law:

$$V = IR \tag{6}$$

When measuring a range of voltages, the slope of the resultant current-voltage curve gives the resistance of the sample. Multiplying this value by the thickness of the films gives the resistivity of the films at a certain temperature. Labview programs were used to control the voltage and

current applied using the Keithley units and calculate the resistivity of the samples. When using the Keithley units, the 9T PPMS was used to lower the temperature of the samples to 1.8 K, giving time-dependent temperature measurements. The Keithley units were used to obtain time-dependent resistivity measurements. In order to obtain the temperature-dependent resistivity of the samples, the initial temperature of the system was raised from 300 K to 300.2 K, creating a spike in the time-dependent resistivity and temperature measurements. Taking measurements at set time values created synced measurements which were then combined to produce the temperature-dependent resistivity.

Chapter 3. Ionic liquid gating of $LaNiO_3$ thin films

3.1 $LaNiO_3$ thin film characterization

$LaNiO_3$ thin films were initially deposited in the QMC nickelate chamber on STO substrates. XRD 2θ-ω patterns of these thin films showed strong STO (002) substrate peaks at around 46.5° but showed no $LaNiO_3$ peaks.

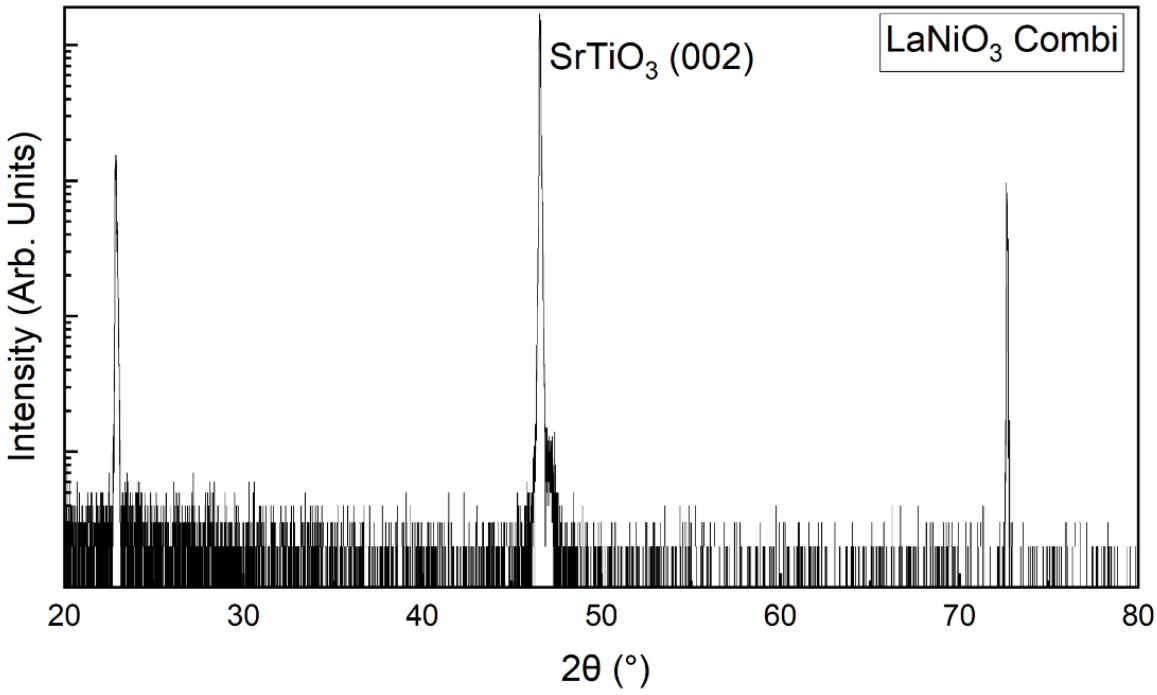

Figure 3.1 XRD pattern of LaNiO3 deposited in QMC nickelate PLD Chamber

This was attributed to issues with the deposition and chamber environment. One issue that arose during depositions was heater malfunctions, which necessitated frequent changes in the chamber and the heater used to heat the substrates during depositions. This frequent change in environment can cause detrimental effects to depositions. The different heaters used can influence how the substrate heats evenly, and a poor chamber environment can introduce contaminants into the system which can reduce film quality and crystallinity, resulting in the lack of a film peak as

seen in Figure 3.1. While these films did not show a substrate peak, they did have metallic resistivity behavior, as seen in Figure 3.2. Because of this, these films were used for the initial IL gating measurements.

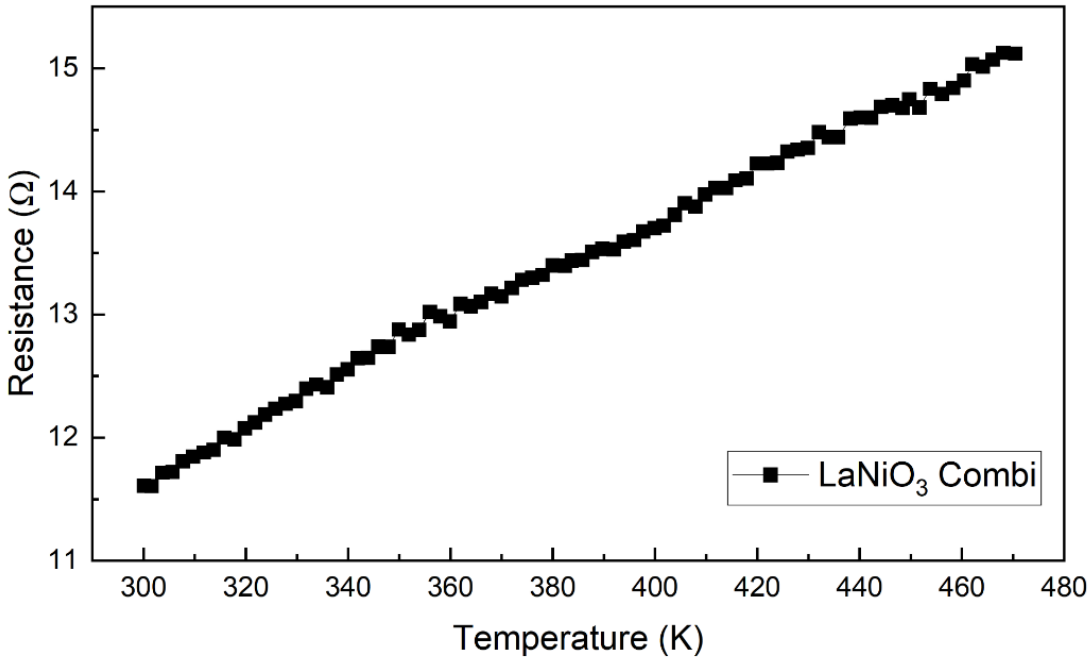

Figure 3.2 Temperature dependent resistivity of LaNiO3 deposited in QMC nickelate PLD Chamber. 300 K to 470 K.

After initial IL gating measurements discussed in a future section, a decision was made to transfer deposition of the $LaNiO_3$ thin films to the Keck PLD chamber. This chamber utilizes a load-lock system and can ensure a better environment inside the chamber for depositions, as the base pressure is around 10^{-9} Torr compared to the 10^{-6} Torr base pressure of the QMC nickelate chamber. In addition, substrates used in this chamber were annealed at 930 °C under an oxygen partial pressure of 5 x 10^{-6} Torr to obtain an atomically flat surface[171]. The XRD patterns of the films deposited in the Keck chamber showed the STO (002) substrate peaks as well as $LaNiO_3$ (002) film peaks at 47.9°, indicating an improvement in film quality and crystallinity, seen in

Figure 3.3. In addition, XRR scans showed that the deposited thin films had an estimated thickness of around 35 nm shown in the inset of Figure 3.3.

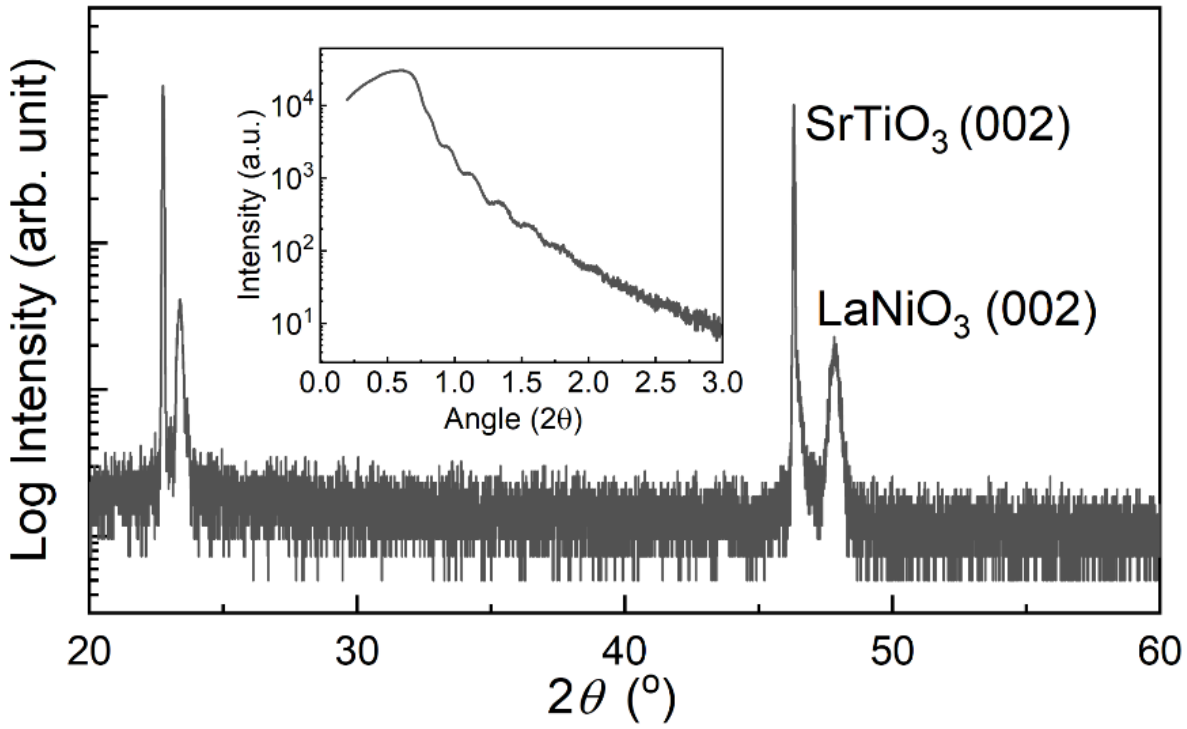

Figure 3.3 The XRD 2θ-ω scan of $LaNiO_3$ on STO(001) substrates deposited in Keck PLD chamber. Inset: XRR graph of $LaNiO_3$ films with thickness of 35 nm.

The out-of-plane c-axis lattice parameter of the $LaNiO_3$ thin films can be determined using Bragg's law[178]:

$$2d\sin(\theta) = n\lambda \tag{7}$$

Where d is the d-spacing, θ is the diffraction angle in degrees, λ is the X-ray wavelength, and n is an integer. The CuK_α X-ray source uses a wavelength of 1.54 Å (λ = 0.154 nm). Substituting these values into Bragg's law gives the d-spacing:

$$d = \frac{\lambda}{2sin\theta} = 0.1897\ nm \tag{8}$$

In cubic crystal structures, the d-spacing is related to the lattice parameter via the following:

$$d_{hkl} = \frac{c}{\sqrt{h^2+k^2+l^2}} \quad (9)$$

Where c is the out-of-plane lattice parameter and $h, k, l,$ are the Miller indices[12]. For pseudocubic $LaNiO_3$, the c-axis lattice parameter from the (002) plane is determined to be approximately 3.79 Å, which is smaller compared to bulk $LaNiO_3$, which has a lattice parameter of 3.838 Å. This confirms the successful deposition of pristine $LaNiO_3$ on the STO substrate without detectable impurity phases. The smaller lattice parameter is likely due to tensile strain in the in-plane lattice, as STO has a slightly larger pseudocubic lattice constant of 3.905 Å[179,180], the effects of which can be seen in Figure 3.4. The tensile strain on the films can result in reduced crystallinity, suggesting the presence of defects within the films such as oxygen deficiencies[28].

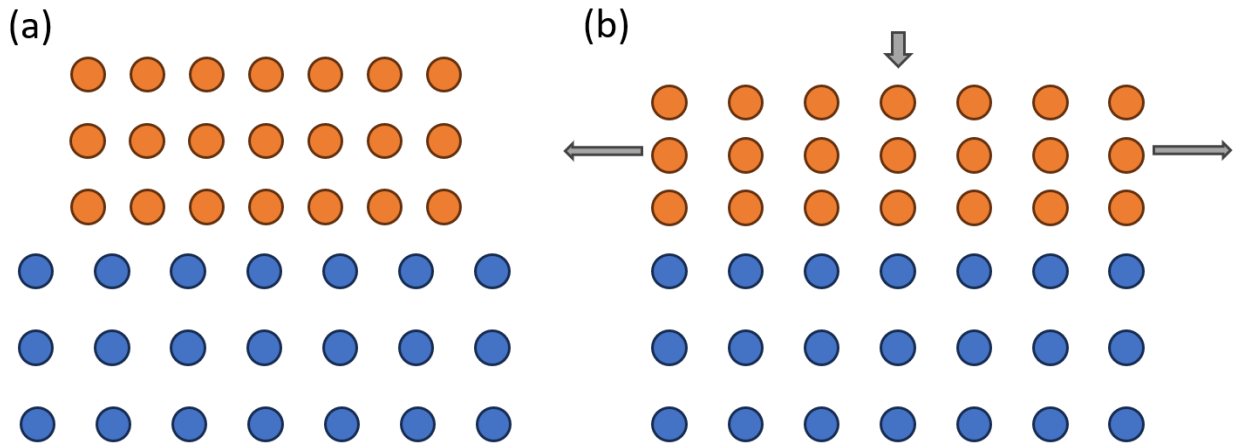

Figure 3.4 Substrate-film interface with (a) no strain and (b) in-plane tensile strain.

AFM scans of the surface morphology showed that the films had a smooth surface, with a Root Mean Square (RMS) of 0.83 nm (Figure 3.5 inset). The RMS is used to determine the average roughness of a surface which accounts for larger peaks and valleys that may appear on a sample. Ideal thin films have a roughness of less than one nm, which is exhibited by the $LaNiO_3$ films deposited. The resistivity behavior of these films was found to be metallic down to 1.8K, which is to be expected for $LaNiO_3$ films (Figure 3.5). The films have a room-temperature resistivity of

0.059 mΩ cm with a resistivity ratio [ρ (300 K) / ρ (2 K)] of 4.08, which is comparable to previously reported results for PLD deposited $LaNiO_3$ films[181].

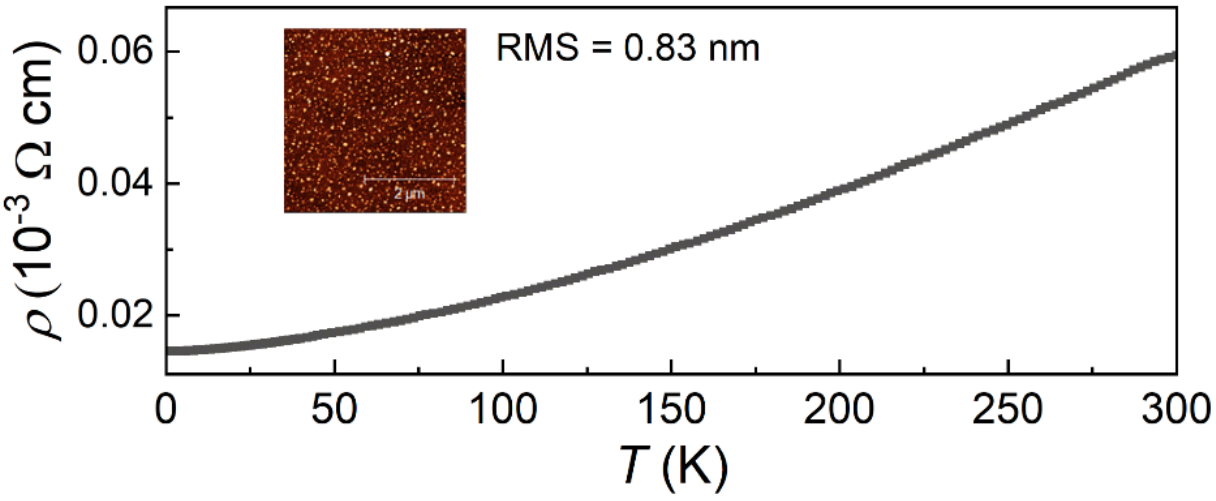

Figure 3.5 Temperature dependent resistivity of pristine $LaNiO_3$ after deposition in the Keck PLD chamber with a range from 1.8 K to 300 K. Inset: 4 µm x 4 µm AFM image of pristine $LaNiO_3$ film with RMS 0.83 nm.

3.2 Ionic liquid gating

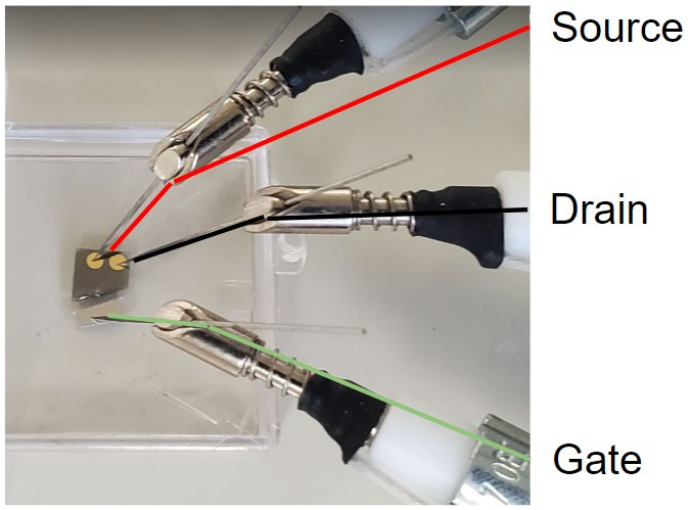

Figure 3.6 Room temperature IL gating using probe station using separate gate electrode. Source, Drain, and Gate electrodes labeled.

Initial IL gating measurements on $LaNiO_3$ thin films were performed using a probe station in an in-air environment, shown in Figure 3.6. EDLT devices were fabricated using the $LaNiO_3$ thin films and the ionic liquid HMIM-TFSI. Two-point probe resistivity measurements were performed with Cr/Au contacts deposited on the film. The film was immersed completely in HMIM-TFSI and platinum probes were used as source/drain electrodes. A separate STO substrate with Cr/Au contacts was used as a gate electrode.

Initial measurements were performed using a gate voltage V_g = +3 V and V_g = -3 V, which was held for a period of 24 hours in succession. The initial IL gating resulted in an increase in resistivity before stabilizing around 1000 Ω. It is important to note that the thickness of these films was not measured, and so only resistance was measured which depends on the thickness of the sample. When a NGV of -3 V was applied, the resistance decreased to below its initial state, which can be seen in Figure 3.7.

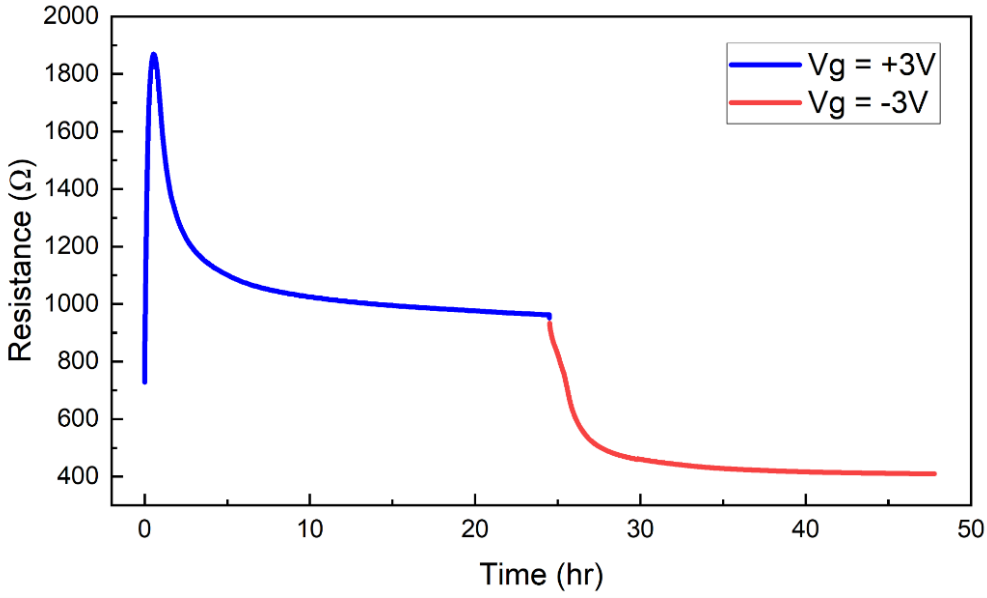

Figure 3.7 Time-dependent resistance during IL gating of a $LaNiO_3$ sample with V_g = + 3 V followed by immediate V_g = - 3 V. Each V_g duration was 24 hours.

The preliminary IL gating experiments demonstrated that IL gating could be used to induce a change in the film's resistance. A PGV demonstrated a resistance increase, while a showed a decrease in resistance. This was explored further using new samples that were fabricated in the Keck PLD chamber. Modification of the $LaNiO_3$ resistivity was investigated with varying V_g applied to the films. To explore the reversibility of IL gating with low gate voltages, the applied gate voltage was cycled between a PGV and NGV of ±1 V, with a period of zero V_g in between. The cycle proceeded as follows: V_g = +1 V → V_g = 0 V → V_g = -1 V → V_g = 0 V, with each step held for 20 minutes (Figure 3.8). When a small V_g of +1 V was applied, the sample's resistivity increased from its initial value of around 129.4 nΩ cm to 130.7 nΩ cm. When the gate voltage is removed (V_g = 0 V), the sample resistivity drops lower, but to a value higher than its pristine state. Even under a small V_g, we note hysteretic gating behaviors in the samples. Under a negative V_g = -1 V, the sample resistance returned to its initial state and remained close to this value even after the gate voltage is removed, suggesting the reversibility of the gating process under this particular

gating cycle. The reversibility of the IL gating was measured with a different pristine sample and was shown to be repeatable, where the resistivity stabilized at a similar level after each cycle. Differences in the film deposition such as thickness and surface roughness affected the resistivity of the films, as different samples showed different resistivity values. However, the behavior under the IL gating process remained similar among the different samples measured.

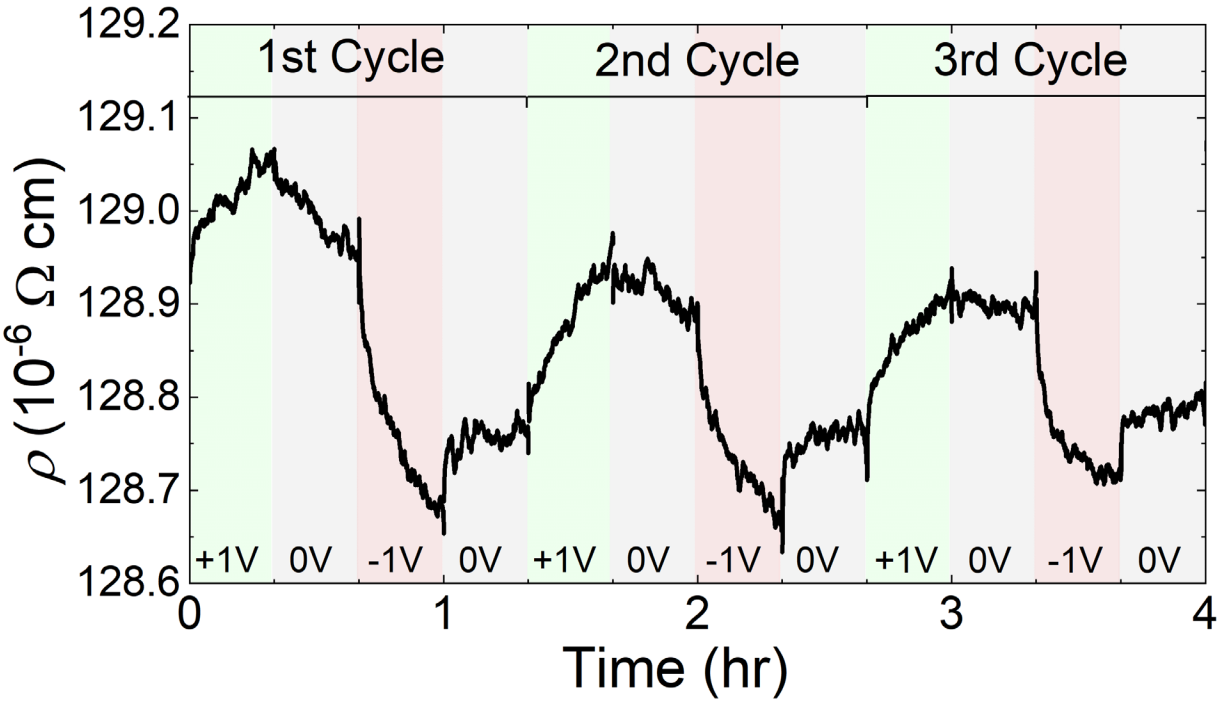

Figure 3.8 Reversibility of resistivity changes in LaNiO3 with gate voltage cycling. The applied V_g sequence used: (1) 20 min positive V_g → (2) 20 min V_g = 0 V → (3) 20 min negative V_g → (4) 20 min V_g = 0V with a low applied V_g = ± 1 V.

To further investigate the film's response to such a gating procedure, we increased the maximum gating voltage to 3V. This was done by cycling through increasing gate voltages with the same sequence as before (PGV → 0 V → NGV → 0 V). After the sample was gated with V_g = ±1 V, the gate voltage was increased to ±2 V and ±3 V. In contrast to the low gate voltage, higher gate voltages resulted in a net increase in the resistivity of the films. An applied V_G = +2V increased the resistivity from 129.4 to 173.2 nΩ cm, with a subsequent V_G = -2V reducing the resistivity to

152.4 nΩ cm. Once the V_G was removed, the resistivity stabilized around 150 nΩ cm. For the maximum gate voltage of +3V, the resistivity increased up to 4,383 nΩ cm and stabilized at 740.9 nΩ cm when the voltage is reversed to -3V after 15 minutes (Figure 3.9).

In contrast to a low gate voltage, higher gate voltages ($|V_G| \geq 2$V) resulted in a net increase in the resistivity of the films. For a $V_G = \pm 2$V, the resistivity shifts by ~0.02 mΩ cm after the gate voltage was removed. A $V_G = \pm 3$V increased the resistivity by up to 30 times its initial state before it stabilized at ~0.741 mΩ cm, five times larger than the initial resistivity.

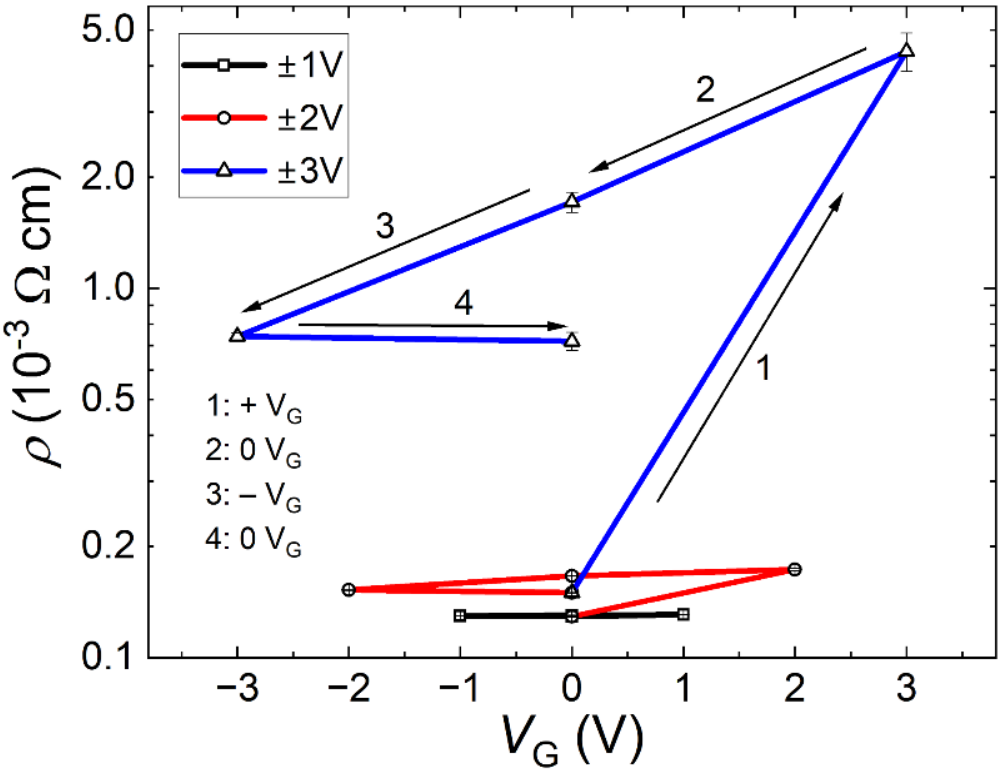

Figure 3.9 Resistivity changes with increasing applied $V_g = \pm 1$ V, ± 2 V, and ± 3 V. The cycles use the same sequence as before but for a duration of 15 minutes per segment.

The hysteretic gating behaviors suggest electrochemical processes that contribute to the observed resistivity changes. Electrostatic doping effects such as electron and hole accumulation have been shown to be reversible up to certain V_g thresholds[77,81]. Electrochemical effects such as

vacancy generation can lead to more irreversible effects on material properties. The fact that the sample's resistivity does not revert to its initial values under this symmetric gating procedure suggests asymmetric reaction barriers for electrochemical reactions during the ionic liquid gating experiments. The difference in resistivity can also be due to oxygen deficiencies in the as-grown films. High-growth temperatures and vacuum-growth can contribute to lack of oxygen in the films, even with the injection of oxygen gas during deposition. This can also lead to the decreased crystallinity seen in the XRD patterns[46]. To further understand the underlying reactions, we perform IL gating measurements in different ambient conditions, i.e., air and vacuum, and measure the change in resistivity under +3V gate over long periods of time.

$LaNiO_3$ thin films were gated in-air using a probe station for a period of four hours with a PGV of 3 V. The resistivity-time graph is shown in Figure 3.10. This gating procedure showed a resistivity increase which peaked after one hour before the resistivity began decreasing and eventually stabilized. IL gating in-air results in a resistivity increase by around 100 times its initial state, peaking at a resistivity of 211 mΩ cm. Because the IL gating can result in oxygen vacancies in the film, it is important to determine the effects of the environment surrounding the gating experiments.

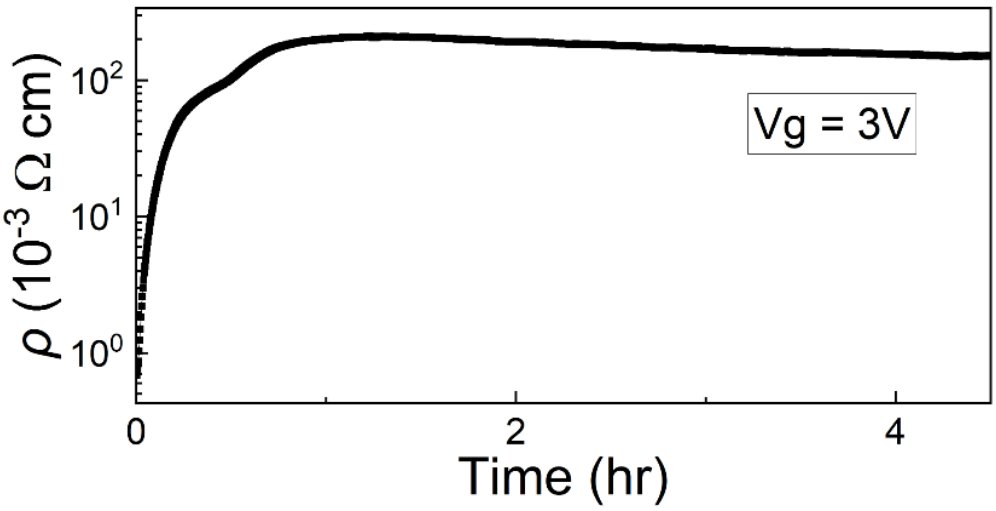

Figure 3.10 In-air gating time dependence of room temperature resistivity in LaNiO3 IL gating devices with a V_g = + 3 V.

To observe the effect that the environment has on the IL gating process, $LaNiO_3$ films were measured in-vacuum using a 9T PPMS. Thin films were adhered to a PPMS puck and wire bonded to gold pads on the PPMS puck. The device designs used are shown in Figure 3.11 and include a three-bar contact design and bonding directly to the sample.

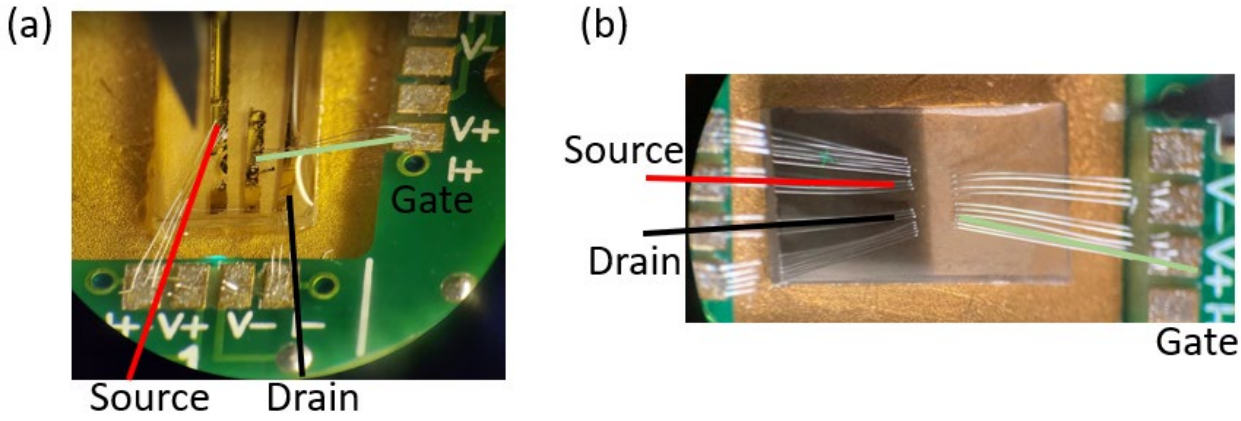

Figure 3.11 In-vacuum gating device designs used. (a) Three-bar design with $LaNiO_3$ deposited on half of the STO substrate. Peeling of the Cr/Au contacts can be seen. (b) Wire bonding directly onto substrate and film. Source, Drain, and Gate electrodes labelled.

An issue with using the contacts that were utilized during the in-air measurements with the IL in the PPMS was the peeling of the contacts when cooling the sample below room temperature.

This resulted in contact issues with the film and unstable measurements. Contact issues manifested in unstable resistivity measurements and as electrical shorts in the circuit if the wires came into contact with one another. This occurred even when an adhesion layer of Cr or Ti was added beneath the Au or Pt contacts. Because of this issue, wire bonding was performed directly onto the surface of the $LaNiO_3$ film and STO substrate. Multiple Al wires were bonded to a single pad to ensure a connection even if one or more of the wires would be disconnected. Once the samples were adhered to the PPMS puck, four drops of the IL HMIM-TFSI were placed onto the sample to form the EDLT. Care was taken after this step to ensure the IL did not come off the surface of the sample before it was placed in the 9T PPMS for measurements. Keithley sourcemeters were used to both measure the resistivity of the films and apply a V_g = +3 V to the gate electrode for the IL gating process. LaNiO3 films that were IL gated in-vacuum exhibited an increase in resistivity from 0.08 mΩ cm to a peak of 65,500 mΩ cm, before the resistivity stabilized at around 46,000 mΩ cm after a period of four hours, shown in Figure 3.12.

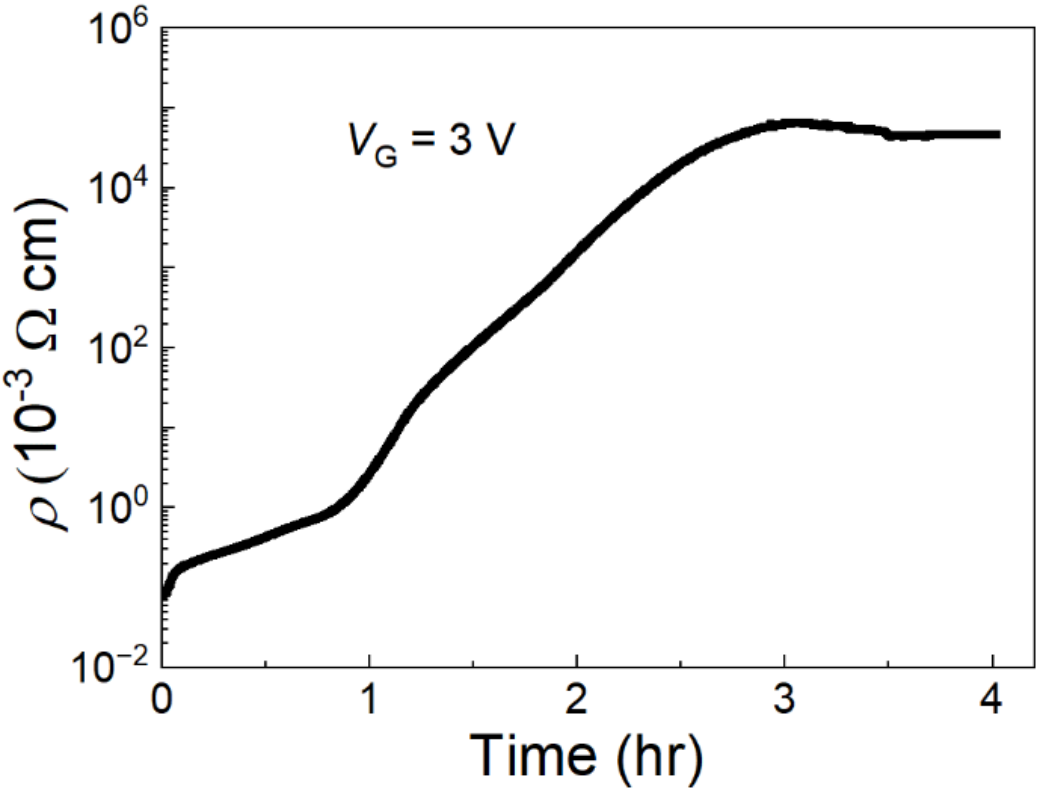

Figure 3.12 In-vacuum gating time dependence of room temperature resistivity in $LaNiO_3$ IL gating devices with a V_g = + 3 V. Inset, images of pristine and gated samples showing transparency difference after IL gating.

AFM measurements of pristine and gated films reveal the changes in surface morphology in the $LaNiO_3$ films due to IL gating. Pristine films have a surface roughness (RMS) of around 0.83 nm, showing that the PLD process produced uniform and smooth films, seen in Figure 3.13. Films that were gated at V_G = +3V for over 10 hours show significantly increased surface roughness with an RMS value of 4.55 nm, demonstrating how the IL gating process affects the surface properties and can cause degradation in the $LaNiO_3$ films. The increase in surface roughness can indicate a phase separation due to changes in the microstructure of the sample. A large enough portion of the $LaNiO_3$ films undergoes a phase transition from metallic to an insulating state, evidenced by the change in temperature dependent resistivity.

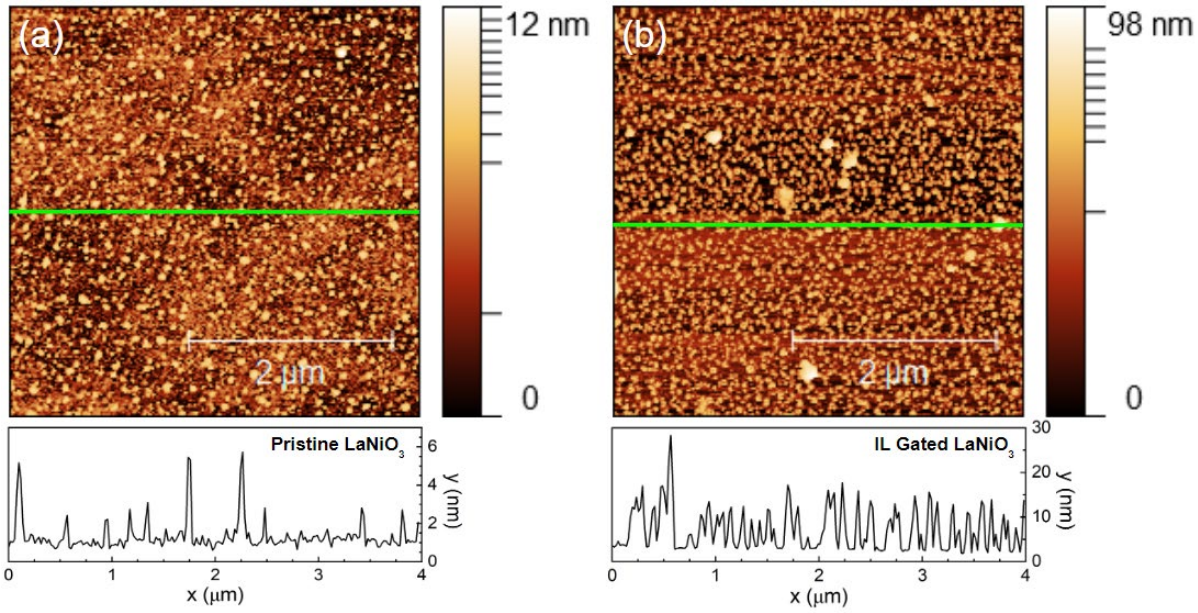

Figure 3.13 AFM scans and line profiles of (a) pristine and (b) IL gated $LaNiO_3$ thin films. Line profiles are extracted from the green line in the AFM scans. Scale bars are shown on the right with the lowest measured point set as 0 nm.

In addition, the IL gating process results in a change in the optical properties of the film. As seen in Figure 3.14, the film becomes more translucent after the film is gated. This can suggest a widening of the optical bandgap of the material as it undergoes a transition to an insulating state[182,183].

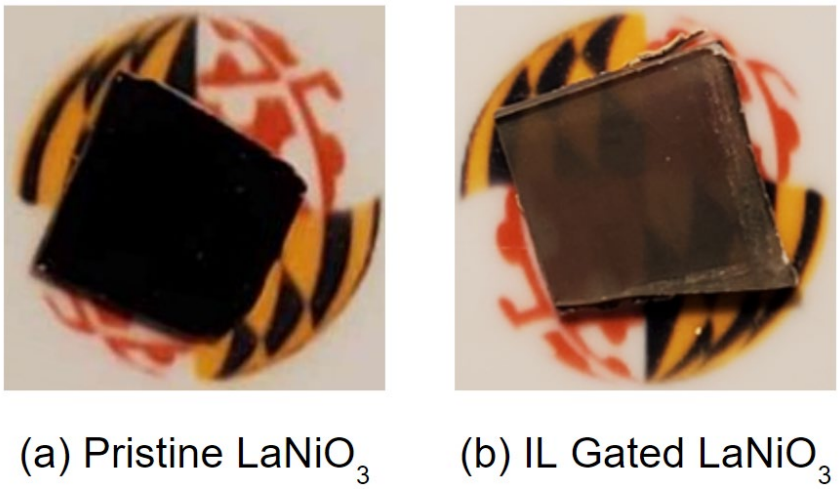

Figure 3.14 Optical images of (a) pristine and (b) IL gated LaNiO3 thin films.

IL gating of the $LaNiO_3$ thin films results in not only an increase in the resistivity of the film, but also modifies the band structures of the sample. This is evidenced by the resistivity-temperature measurements taken using in-vacuum gated samples from 300K down to 1.8K. As seen in Figure 3.15, pristine samples show metallic behavior, with decreasing resistivity as the temperature decreases. After a $LaNiO_3$ film sample was gated in vacuum for four hours and its resistivity had stabilized, the temperature was reduced to 1.8 K with the IL and V_G still applied to the sample. Unlike the pristine $LaNiO_3$ sample, this gated sample with V_G = +3V shows an insulating resistivity behavior, where the resistivity increased from 3,500 mΩ cm to over 42,000 mΩ cm as the temperature decreased. Interestingly, the insulating behavior persists even after removing the ionic liquid and the vacuum environment. After removing the sample from PPMS vacuum and rinsing with isopropanol to remove the IL, the samples were then stored in a desiccator for a few days before being remeasured in a PPMS. When the *R–T* behavior was remeasured, the initial resistivity at room temperature had reduced to 240 mΩ cm but showed an insulating behavior, demonstrating a persistent change in the electrical properties of the $LaNiO_3$ films compared to its initial pristine state. Remarkably, even very low gate voltage (V_G << 1V) can induce insulating behavior in the $LaNiO_3$ devices, making the slope of the *R–T* curve negative.

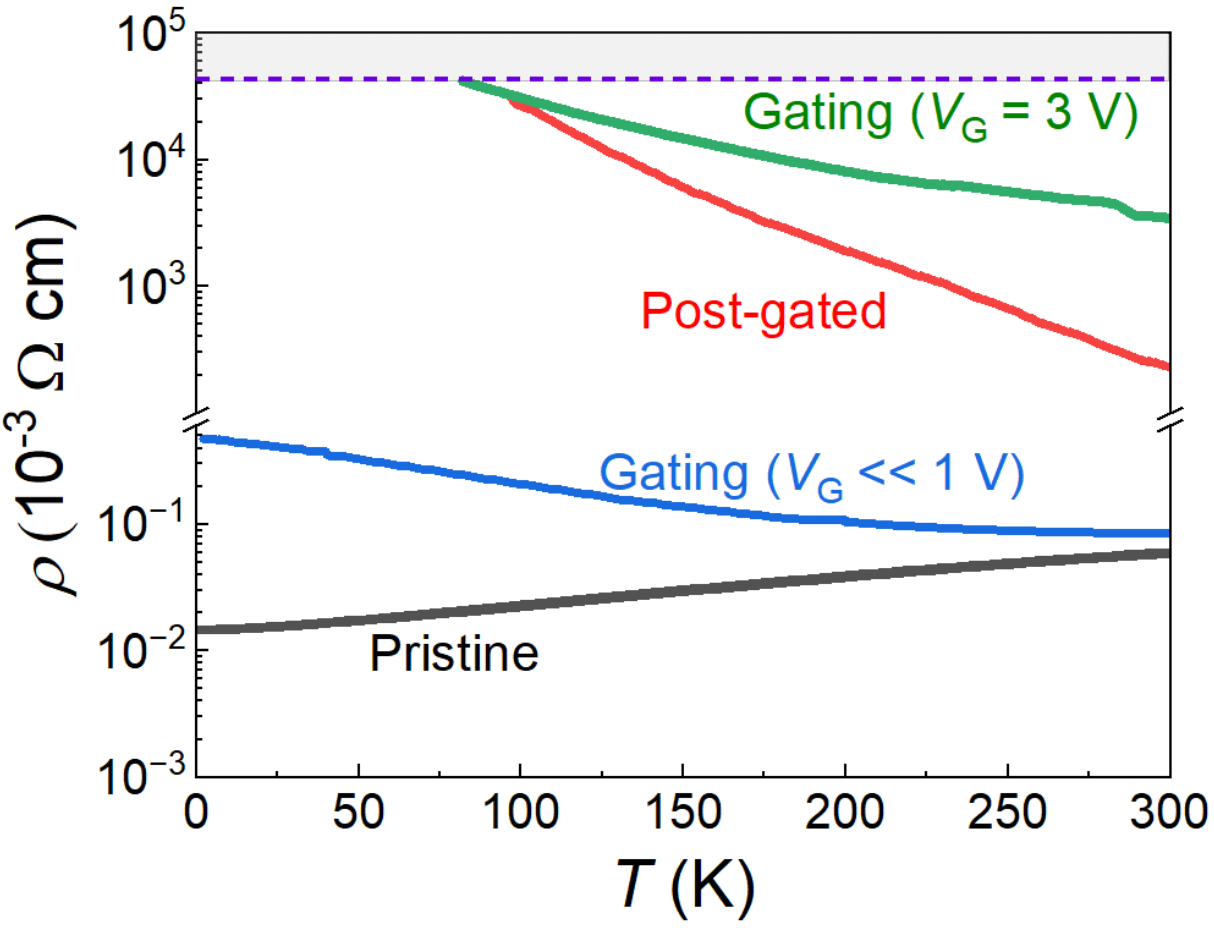

Figure 3.15 Temperature dependence of $LaNiO_3$ samples in the pristine state (pristine), during IL gating (gating), and after the V_g and IL were removed from samples (post-gated at 3 V). A physical measurement limit occurs when the resistance was too large to be measured (gray area).

3.3 X-ray photoelectron spectroscopy of IL gated films

In order to investigate the underlying electrochemical reactions leading to our experimental observations, XPS measurements were taken on various films which were gated for different periods of time. XPS graphs of the O 1s and Ni 3p spectra for pristine and 40-hour gated films are shown in Figure 3.16. The XPS data were calibrated using the C 1s = 284.8 eV peak as a standard[177].

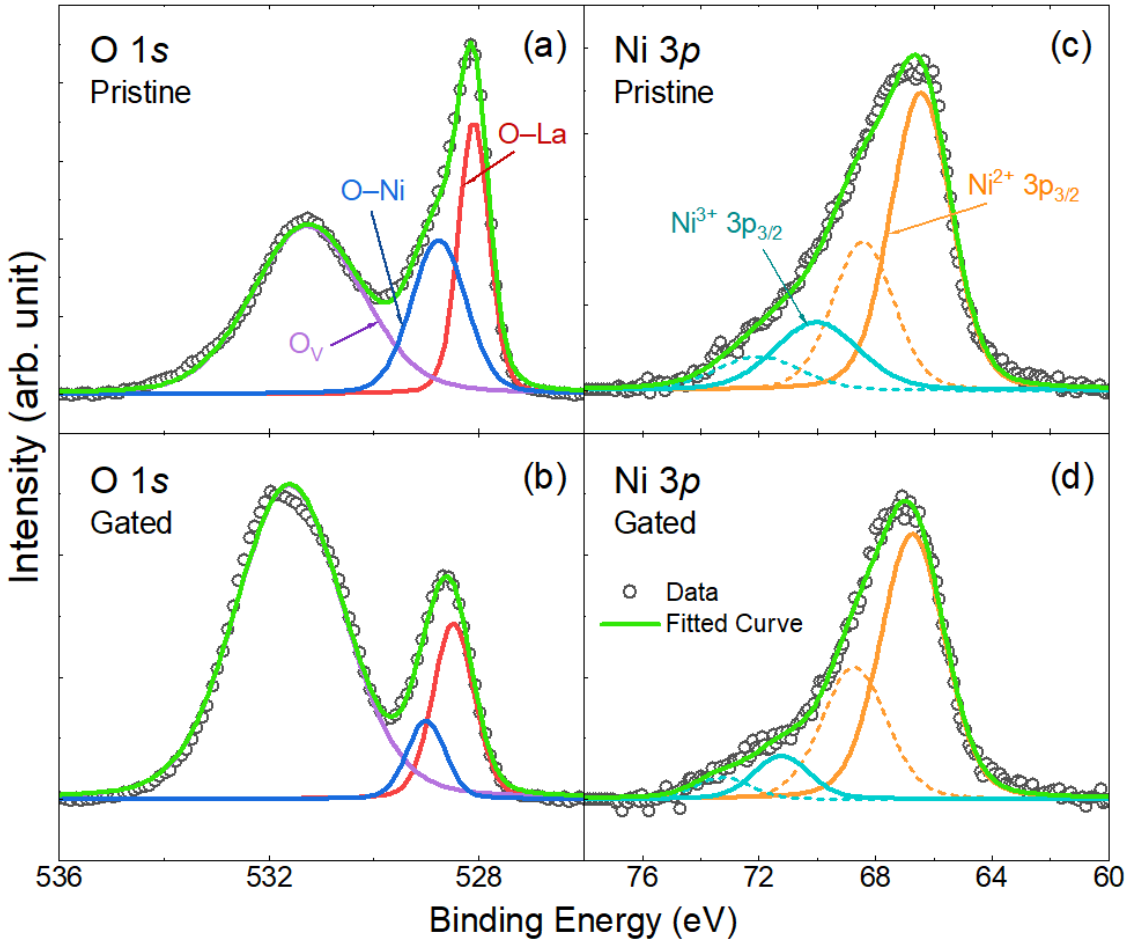

Figure 3.16 XPS spectra of $LaNiO_3$ films in pristine and gated states: O 1s for pristine (a) and gated (c) samples, and Ni 3p for pristine (b) and gated (d) samples. The O 1s XPS data was fitted by deconvoluting with three components: O–La (red), O–Ni (blue), O_V (purple). The Ni 3p XPS spectra show the deconvoluted $3p_{3/2}$ peaks (solid lines) and the $3p_{1/2}$ peaks (dashed lines) for Ni^{2+} (orange) and Ni^{3+} (cyan) ions.

The O 1s spectra show peaks at 527.9 and 528.5 eV (O_{lat}), which can be attributed to lattice oxygens that are bonded to La and Ni atoms in the crystal structure, respectively [28,49,184–186]. The peak at around 531.2 eV (O_V) can be attributed to oxidative species on the surface, such as OH^-. This peak has been shown to be representative of oxygen vacancies that have formed in the film [28,48,49,184–186]. From the O 1s spectra with increasing gating time, the ratio O_V/O_{lat}, which relates to the concentration of oxygen vacancies in the film, can be determined using the integrated area of the fitted peaks. For pristine samples, O_V/O_{lat} is approximately 1.07. As the samples are gated for increasing periods of time, the ratio increases up to 2.58 for the 40-hour gated $LaNiO_3$ sample. Table 3.1 shows the binding energies of the peaks used to determine O_V/O_{lat}. A full table including the FWHM and relative area can be found in Appendix 1.

Table 3.1 Binding energies of the O 1s spectra of IL gated $LaNiO_3$ thin films shown in eV. O_V represents oxygen vacancies, O-Ni and O-La are lattice oxygen bonded to Ni and La atoms and make up O_{lat}.

	Binding energy (eV)			
	O_V	O_{lat}		O_V/O_{lat}
Gating time		O – Ni	O – La	
Pristine	531.21	528.59	527.99	1.072
15 min	531.35	528.79	528.43	1.366
10 hour	531.45	528.9	528.62	1.443
20 hour	530.99	528.63	528.16	1.797
40 hour	531.77	528.96	528.44	2.581

This suggests that the IL gating of the film results in an increase in oxygen vacancy content of the films by a factor of around 2.4. This also explains how the gating environment affects the

sample's response to electrical voltages. In the in-air environment with higher oxygen partial pressure, the IL contains more oxygen and in fact can be saturated with oxygen atoms[75]. This decelerates the process of removing the oxygen atoms from the $LaNiO_3$ films, reducing the amount of oxygen vacancies formed in the film and resulting in a smaller resistivity peak. In contrast, gating in-vacuum allows the oxygen atoms that are removed from the film to be purged from the vacuum chamber, resulting in more oxygen vacancies in the film and a greater change in resistivity[49,75]. Oxygen deficient $LaNiO_{3-\delta}$ films have been shown to be insulating when compared to stoichiometric $LaNiO_3$ films[51,187]. Annealing in an oxygen or vacuum environment alters the concentration of oxygen vacancies present and in turn affects its resistivity. Introducing further oxygen deficiencies through methods such as CaH annealing can result in further structural evolutions to the insulating $LaNiO_{2.5}$ phase and eventually the superconducting infinite-layer $LaNiO_2$ phase[187].

The increased oxygen vacancy formation in the films can result in the reduction of Ni^{3+} to Ni^{2+} in the films, which we further investigated using the Ni 3p spectra, as shown in Figure 3.16. Due to the coupling of spin-orbit splitting and multi-splitting, both the La 3d and Ni 2p spectra show complex multi-component structures[188–190]. The Ni $2p_{3/2}$ peaks also overlap with the La $3d_{3/2}$ peaks, creating difficulties in determining the Ni valence in the films[34,191,192]. On the other hand, the Ni 3p core-level spectrum, while having a reduced intensity compared to the Ni 2p spectrum, does not overlap with other peaks[34,52,193]. Therefore, the Ni 3p core-level spectrum was used to distinguish between Ni^{3+} and Ni^{2+} in the films.

The Ni 3p spectrum shows peaks at 66.46 eV and 70.09 eV, corresponding to Ni^{3+} and Ni^{2+} $3p_{3/2}$, respectively, as well as their satellite peaks[34,48,52,193–195]. The pristine sample exhibits a Ni^{3+}/Ni^{2+} ratio of 0.304, obtained using the relative area of the main $3p_{3/2}$ peaks. The relatively

high Ni^{2+} content in pristine samples could be related to the formation of oxygen vacancies at the sample surface due to the thermodynamic instability of Ni^{3+} ions[196]. As the films are gated for longer periods of time, this ratio decreases to 0.143, showing the shift in Ni valence in the film towards Ni^{2+}, seen in Table 3.2. A complete table including the FWHM and relative area of both the main and satellite peaks is included in Appendix B. These XPS measurements offer complementary insights into the trend where longer gating times increase the resistivity of the $LaNiO_3$ films, affecting the Ni valence and oxygen vacancy concentration.

Table 3.2 Binding energies of Ni 3p spectra of IL gated $LaNiO_3$ films. Only the main Ni^{3+} and Ni^{2+} peaks are included in the Ni^{3+}/Ni^{2+} ratio.

	Binding energy (eV)		
Gating time	Ni^{3+}	Ni^{2+}	Ni^{3+}/Ni^{2+}
Pristine	70.08	66.45	0.307
15 min	71.16	66.57	0.173
10 hour	71.35	66.75	0.165
20 hour	70.65	66.38	0.157
40 hour	71.23	66.73	0.143

3.4 Electronic structure of IL gated $LaNiO_3$

Previous experiments established that in the absence of hydrogen doping, the IL-gated rare earth nickelate can go through the following electrochemical reactions[54]

$$2Ni^{3+} + O_O^X \leftrightarrow 2Ni^{2+} + V_O^{2+} + \frac{1}{2}O_2 \quad (10)$$

Where O_O indicates oxygen atoms occupying oxygen sites and V_O indicates oxygen vacancy sites. When the oxygen leaves the nickelate lattice, the Ni^{3+} atoms in the lattice become destabilized and form Ni^{2+} ions, resulting in the increase in resistivity that is seen in the films[54]. This can be seen in Figure 3.17, where the electrons that accompany the oxygen vacancies localize onto nearby Ni ions and reduce the valence from Ni^{3+} to Ni^{2+}. This is consistent with our XPS studies of $LaNiO_3$ films at the initial gating stage, where both Ni valence state and oxygen vacancy concentration are modified significantly, as seen in Figure 3.18. Intriguingly, with longer gating time, the change in the Ni valence slows down while the oxygen vacancy concentration shows a more significant increase. This suggests that a more complicated electrochemical process than previously assumed occurs over longer gating periods, where oxygen vacancies are created without significant modification of the Ni valance state.

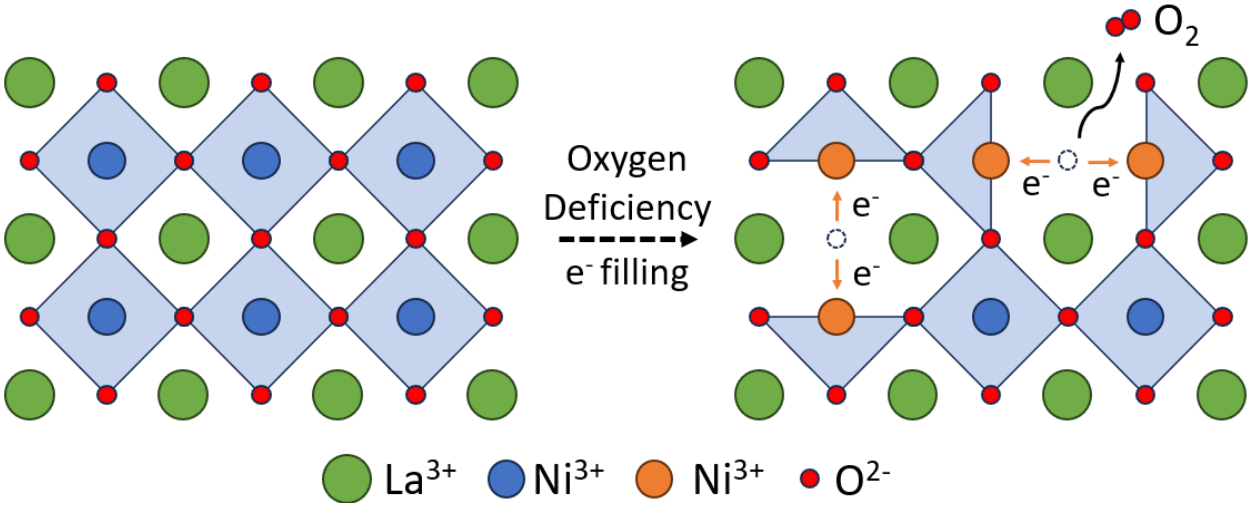

Figure 3.17 Schematic of $LaNiO_3$ showing oxygen vacancy formation and electron filling of Ni to reduce its valence state from Ni^{3+} to Ni^{2+}.

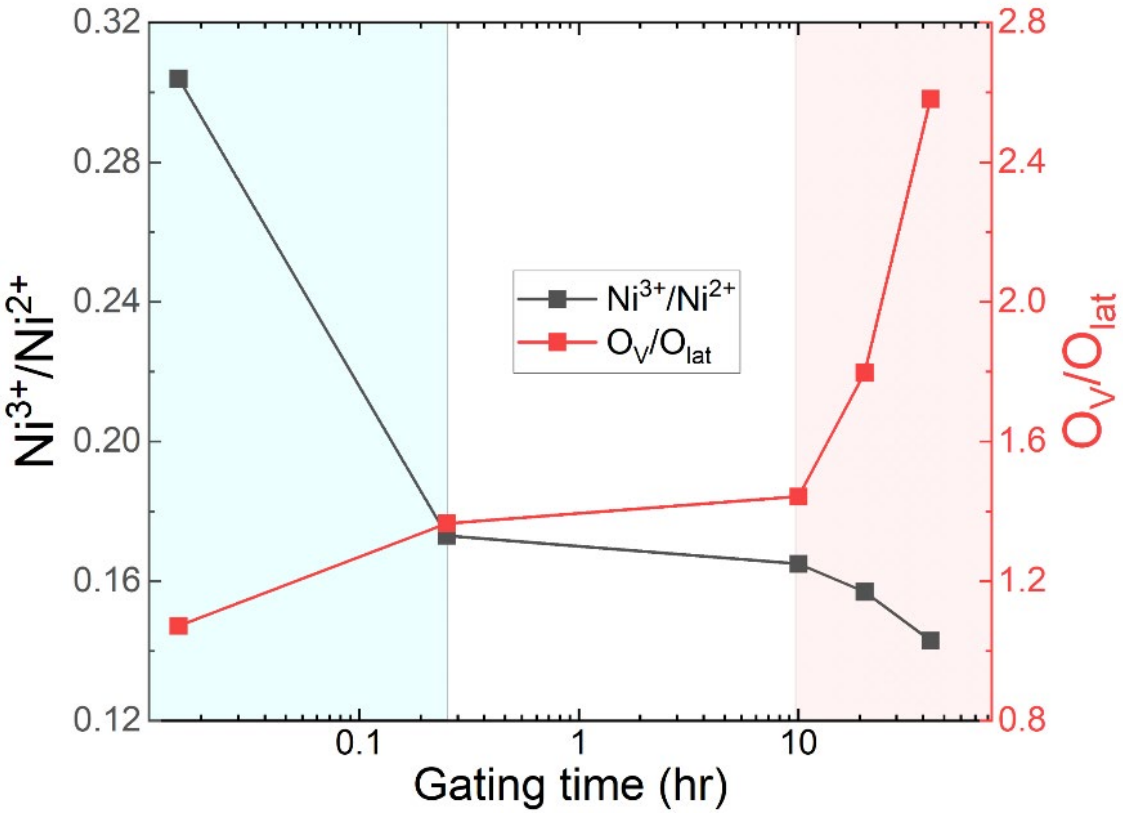

Figure 3.18 Evolution of Ni valence state and oxygen vacancy concentration in $LaNiO_3$ as a function of IL gating time.

To understand the observed experimental phenomena, we first rationalize the change in the resistivity and then examine additional insights gained from chemical characterizations. The change in electrical properties of the $LaNiO_3$ films can be attributed to the shifts in oxygen vacancy concentration and Ni valence in the films. The metallic behavior in $LaNiO_3$ comes from the overlap between the occupied O 2p valence band and the unoccupied Ni 3*d* conduction bands[34]. When oxygen vacancies are introduced into the film, the Ni valence shifts from Ni^{3+} to Ni^{2+}. Compared with Ni^{3+} with a $(t_{2g}^6 e_g^1)$ electron configuration, Ni^{2+} hosts a partially filled e_g orbital $(t_{2g}^6 e_g^2)$ at exactly half-filling, which leads to much stronger correlated electron effects and leads to a bandgap in the film [29,39,44,49,197]. Furthermore, the larger ionic radius of Ni^{2+} (69 pm) compared to Ni^{3+} (56 pm) increases the Ni–O bond length and reduces the Ni–O–Ni bond angle[49,198]. This causes a reduction in the bandwidth for both the O 2p and Ni 3d bands and reduces the overlap. The reduction of the bandwidth also opens up a larger charge transfer bandgap, as shown in 3.19[29,185,193,194]. These effects of the Ni valence change result in the bandgap opening and lead to the increased resistivity exhibited by the films, i.e., a transition from a metallic phase to an oxygen deficient insulating phase of $LaNiO_{3-\delta}$.

While this simple picture captures the essence of the experimental observations, the evolution of oxygen vacancy concentrations and Ni valence states from XPS analysis reveals the nontrivial band hybridization effects. In particular, for short gating duration and low oxygen vacancy concentrations, there is a large modification of the formal valence state of Ni, indicating that a significant fraction of electrons is added to nickel with positively charged oxygen vacancy formation, as shown in equation (1). Upon higher doping concentrations, the removal of oxygen vacancies does not modify the Ni valence state at the same rate as before (Figure 3.18), suggesting the electrons now occupy the oxygen vacancy sites by creating vacancies with reduced positive

charges V_O^+ or even neutral charges V_O^0. In the band structure picture, this corresponds to the electron filling of the O 2p band. Therefore, the insulating states created by the ionic liquid gating at the longer gating period shall be considered as an intermediate state between Mott-Hubbard and charge-transfer insulator featuring significant band overlap between the O 2p band and the lower Hubbard band. This can be seen as a transition state to the infinite-layer superconducting $RNiO_2$ phase, which has been shown to have signatures of a Mott-Hubbard system, where the O 2p band is located beneath the Ni 3d lower Hubbard band[199]. Such realization of a mixed Mott-Hubbard and charge-transfer state creates exciting opportunities for investigating and controlling the interplay between correlation and charge-transfer in oxides by ionic liquid gating.

As the changes in resistivity can be attributed to an increased concentration of oxygen vacancies and a Ni valence change, it is possible that the MIT in $LaNiO_3$ that occurs due to the applied positive V_G can be reversed by switching the polarity of the applied gate voltage.

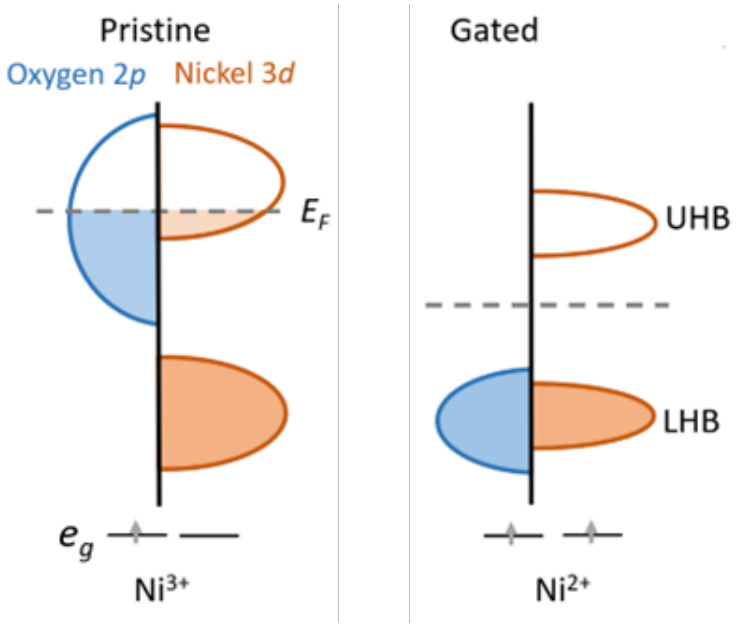

Figure 3.19 The band structure and electron configuration of (b) pristine and (c) gated $LaNiO_3$.

We note, however, that in our symmetric gating experiments the resistivity increases to a higher value than its initial state. In rare earth nickelates, Ni^{2+} is known to be thermodynamically more favorable than Ni^{3+} under ambient oxygen pressures. Although Ni^{3+} in $LaNiO_3$ is the most stable among the rare earth nickelate family[196], the thermodynamic and kinetic barriers to switch from Ni^{3+} to Ni^{2+} can still be considerably smaller than the reversal process. For applications in neuromorphic computing, it is critical to have a pair of bistable states with minimal difference in the thermodynamic and kinetic barriers so that one can realize a symmetric gate response[54,62,200]. Further development of methods to control the energy landscapes such as by strain tuning[201,202] and capping with an oxygen barrier to prevent oxygen[203–206] loss to the environment could open exciting avenues for applications to neuromorphic computing devices.

3.5 Conclusions

We fabricated $LaNiO_3$ thin films using PLD and performed systematic IL gating experiments by tuning gate voltage, duration, and vacuum environment. We observed an increase in the resistivity over six orders of magnitude in the $LaNiO_3$ devices gated in a low vacuum. This is attributed to a rise in oxygen vacancy concentration and a shift in the Ni valence from Ni^{3+} to Ni^{2+}. XPS analysis further shows non-trivial modification of Ni and O valence states, which were attributed to the electron filling of the Mott-Hubbard and charge-transfer bands. These electrochemical transitions enhance electron-electron correlation and increase the structural distortion of the NiO_6 octahedral units. This results in a narrower Ni-O-Ni bond angle, decreasing the bandwidth, reducing the overlap between O and Ni bands, and eventually inducing an insulating phase transition in $LaNiO_3$. This demonstrated capability of reliably and reversibly manipulating the electrical properties of perovskite nickelate thin films via IL gating opens new avenues for investigating the interplay between electron correlation and orbital effects and may find applications in neuromorphic computing.

Chapter 4. LiB thin films

4.1 $LiCoO_2$ thin film delithiation

In Li-ion SSBs, the interface between components can have strong effects on properties such as power density and capacity retention. Investigation of these interfaces is important to understand the mechanisms leading to instability in SSBs. $LiCoO_2$ (LCO) has been used extensively as a cathode in LiBs due to its high-energy capacity and cycle life[147,160,161]. As a cathode, the primary purpose is to donate Li ions to be stored in the anode material, traditionally graphite, which can result in Li deficiency in LCO. This Li deficiency has been shown to induce structural changes in LCO at the interface between LCO and a liquid electrolyte. The use of liquid or solid electrolytes to induce delithiation can result in the formation of a solid-electrolyte interface and chemical byproducts, which can affect measurements[160]. Investigation of the effects of Li deficiency in isolated electrodes is limited due to the difficulty of obtaining high-quality delithiated films[160]. To resolve this, delithiation via a physical process was investigated by Salagre et al using LCO films we deposited at QMC. LCO thin films for delithiation experiments were deposited on Nb-STO (111) substrates using the lithium chamber in QMC. $SrRuO_3$(111) was used as a buffer layer to provide electrical contact to LCO. XRD patterns of the LCO films show peaks which correspond to rhombohedral LCO. LCO has a pseudocubic nature, meaning the {001} family of planes of rhombohedral LCO corresponds to the {111} family in the pseudocubic orientation[162]. Thus, in the XRD 2θ-ω pattern shown in Figure 4.1, the LCO (003), (006), (009) peaks are visible alongside the STO (111) peak. AFM scans of the films show a roughness RMS of 6.3 nm. The scans show the formation of grains, which can indicate either Volmer-Weber or Stranski-Krastanov film growth. This can contribute to the increased roughness of the samples and result in pinholes.

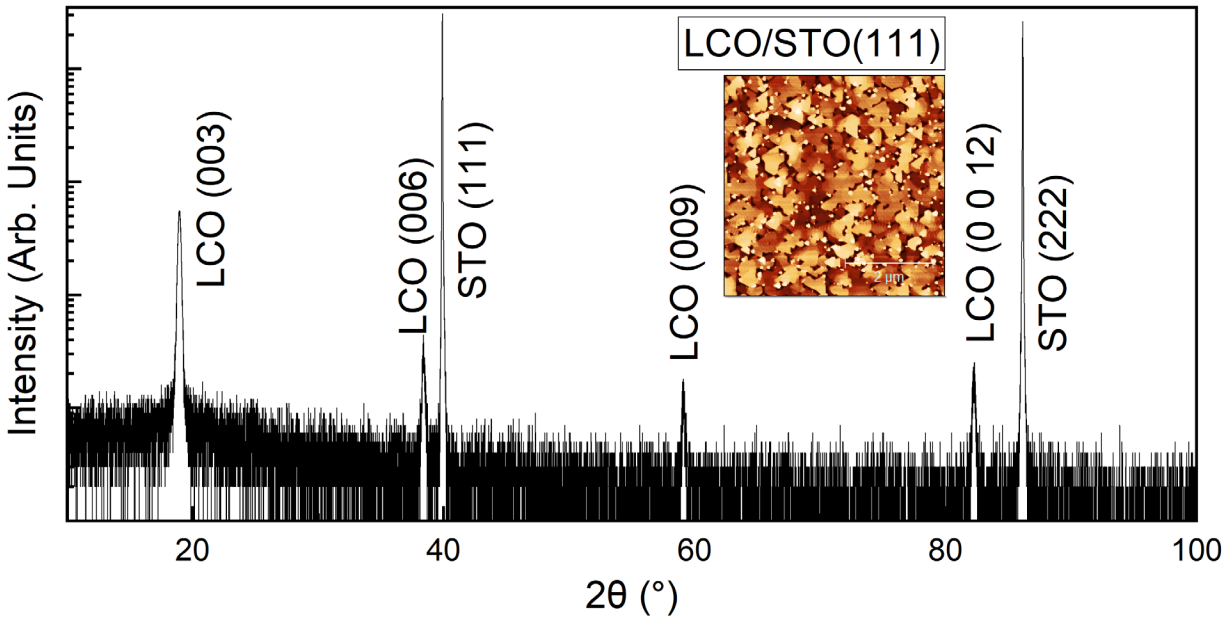

Figure 4.1 XRD 2θ-ω patterns of LCO deposited on STO(111).
Inset: AFM image showing RMS = 6.3 nm.

These LCO films were used by Salagre et al. to demonstrate a novel delithiation process using ion sputtering and annealing cycles. Ne^+ sputtering was used to physically remove Li ions without generating a solid electrolyte interphase that occurs when using liquid or solid electrolytes for delithiation. During Ne^+ sputtering, the Li atoms are efficiently removed from the film, although the heavier Co and O atoms can still be removed. This can lead to damage to the ion penetration layer, which varies in thickness based on the sputtering energy used. After annealing in O_2, the penetration layer can recover its crystallinity while maintaining an overall depletion of Li. This was supported with the XPS spectra of the Li 1s region normalized to the Co 3p peak intensity. When sputtered, the Li 1s intensity relative to the Co 3p peak was reduced compared to the pristine sample. After the sputtered films were annealed, the Li peak intensity recovered slightly, but still showed reduced Li intensity[160], which can be seen in Figure 4.2.

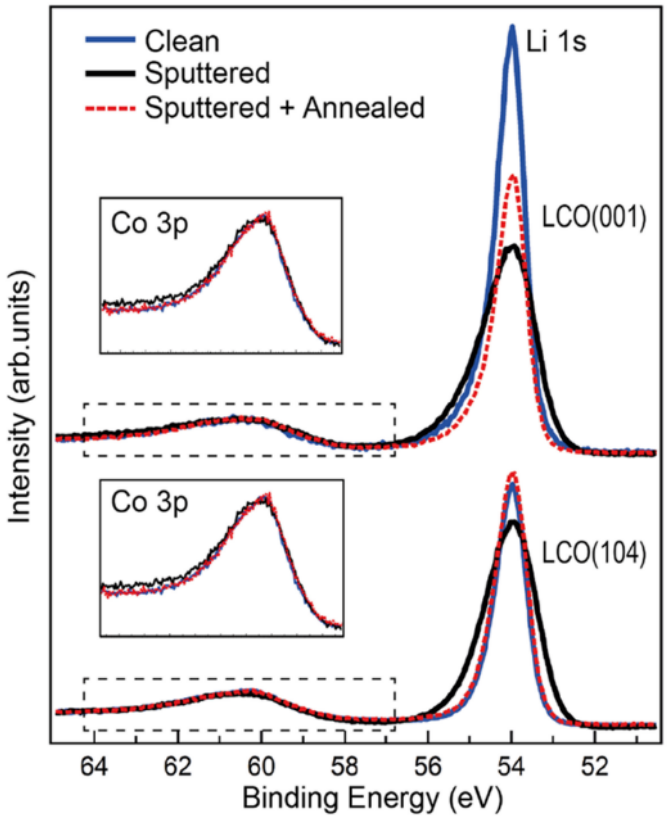

Figure 4.2 Co 3p and Li 1s XPS spectra, corresponding to pristine (blue), Ne^+ sputtered (black), and sputtered and annealed in O_2 (red) samples. The spectra are normalized to the intensity of Co 3p, shown in the inset graphs. Both LCO (001) and (104) orientations are shown.

Physical delithiation allows for examination of the electronic band structure of LCO and the changes that occur due to delithiation. X-ray absorption spectroscopy was used to monitor the charge states of Co and O after Ne^+ sputtering. It was found that the delithiation of LCO films resulted in the formation of Co^{4+} ions and holes near O atoms to compensate for the charge due to Li deficiencies. The resulting films after delithiation and annealing showed changes in the surface termination to retain charge neutrality, which was found to be due to 0.5 monolayer of ordered Li atoms[160]. This delithiation method can be used to investigate electronic structure and charge state in electrodes for solid-state interfaces in the future without contamination due to solid or liquid electrolytes.

4.2 Ta-LLZO/Li_2O thin films

4.2.1 Ta-LLZO/Li_2O thin film characterization

Ta-doped LLZO and Li_2O multilayer thin films were grown on GGG and MgO substrates to investigate the solid-electrolyte interface that forms when in contact with liquid electrolytes. These films were deposited using the lithium chamber in the QMC. Initial characterization of the Ta-LLZO/Li_2O multilayer films grown involved XRR and AFM to investigate the thickness and surface roughness of the films. XRR patterns (Figure 4.3) show that the thickness of deposited films is approximately 34 nm. AFM scans show a surface roughness ranging from 0.5 nm to 1.5 nm, indicating smooth surfaces with minimal peaks or valleys.

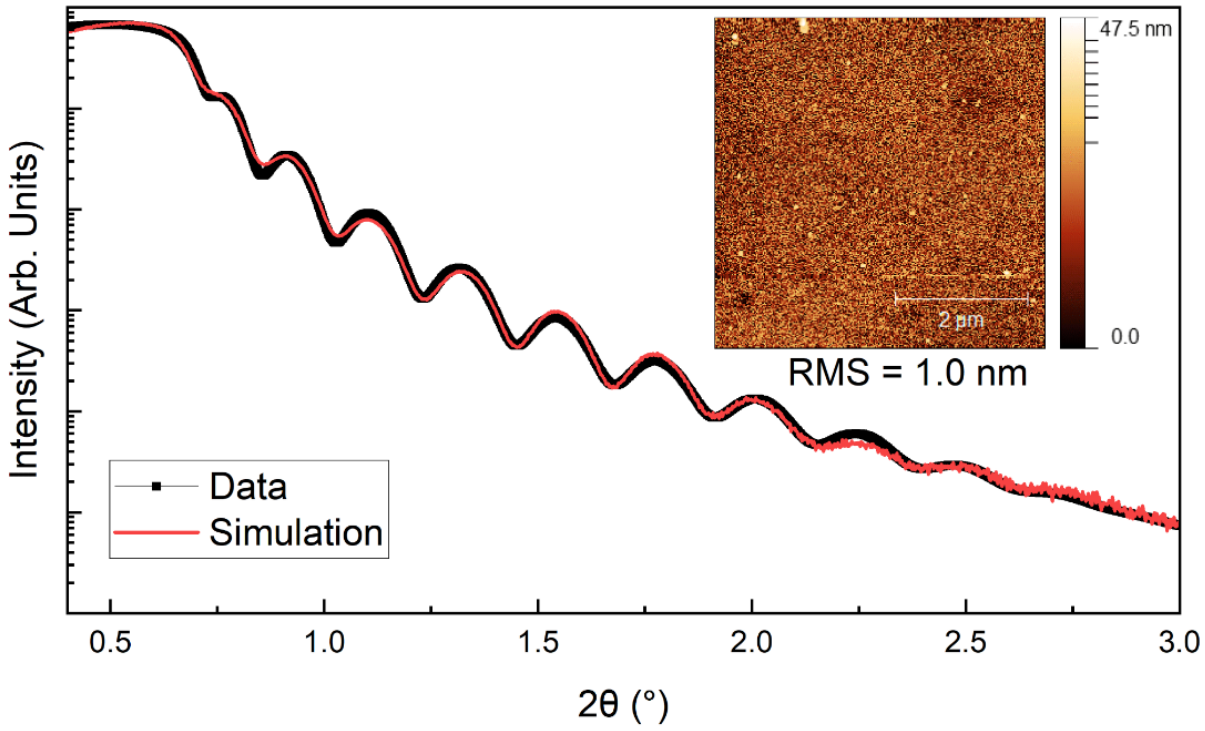

Figure 4.3 XRR pattern of Ta-LLZO/Li_2O thin films with thickness of around 34 nm. Inset: AFM scan showing RMS = 1.0 nm.

XRD patterns of the Ta-LLZO films grown on GGG substrates were taken by collaborators at NIST. These patterns show evidence of LLZO film peaks, but also includes possible contaminant

phases such as $La_2Zr_2O_3$, seen in Figure 4.4. While these films showed evidence of LLZO film growth, future films were deposited on MgO substrates. MgO was chosen as the primary substrate for depositions due to issues with GGG substrates for future neutron reflectometry measurements. This is because Gd is highly absorbing, and the neutron beam is unable to penetrate through the substrate during measurements, which is required for studies with LE soaking. Thus, MgO was used as the substrate for further depositions.

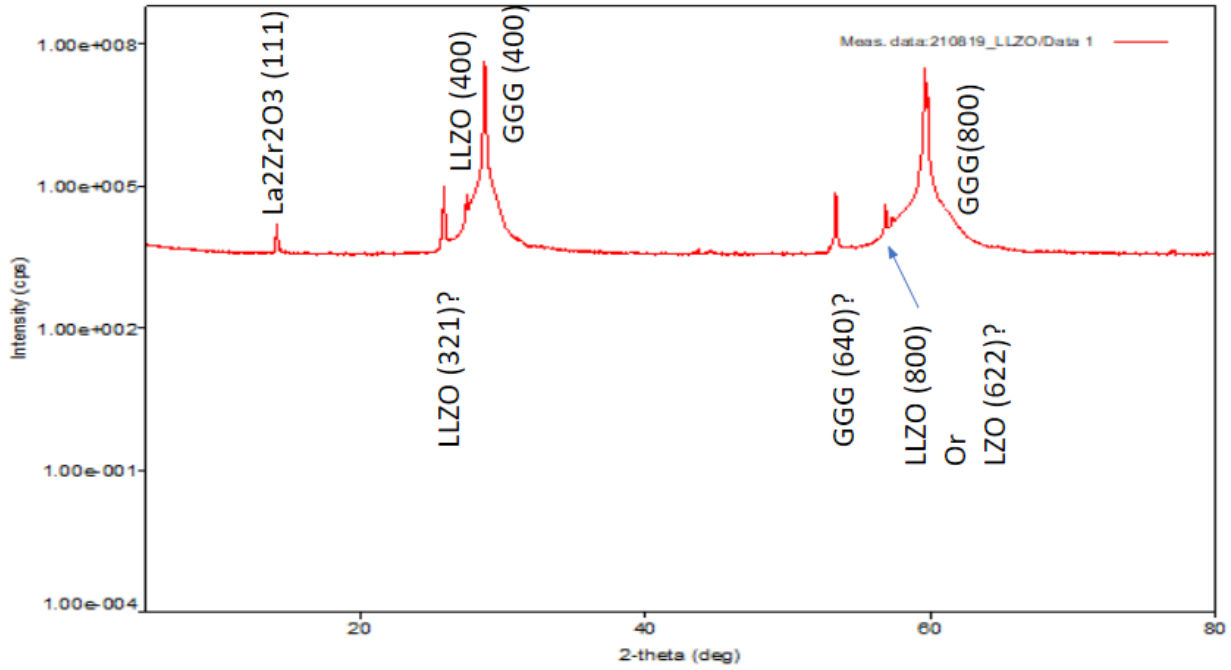

Figure 4.4 XRD 2θ-ω pattern of Ta-LLZO/Li_2O deposited on GGG (100) substrates.

Ta-LLZO/Li_2O films deposited on MgO substrates were primarily scanned using the C2 and XPert diffractometers in the XCC to generate XRD patterns. The C2 diffractometer utilizes a GADDS to detect reflection intensities of the film, producing frames which can be integrated to produce 2θ-intensity plots as seen in Figures 4.5 and 4.6. The MgO_2 peak can be due to substrate quality issues discussed further or due to oxidation that can occur when the substrate is exposed to atmosphere.

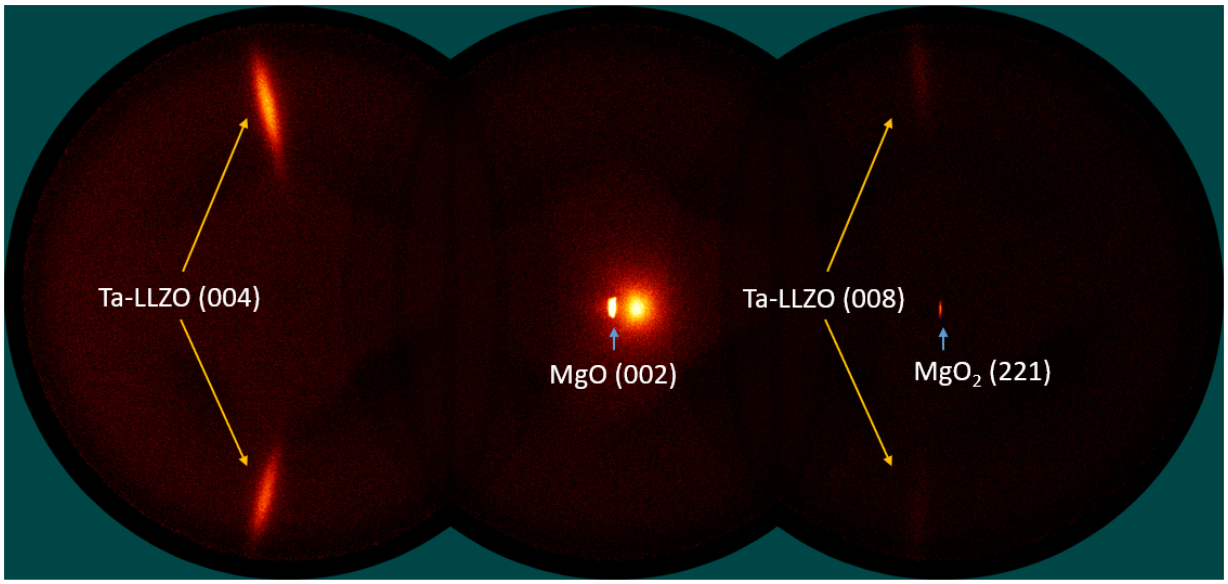

Figure 4.5 XRD GADDS frame of Ta-LLZO with 2θ range 17° - 69°. Ta-LLZO and MgO intensity peaks are labelled.

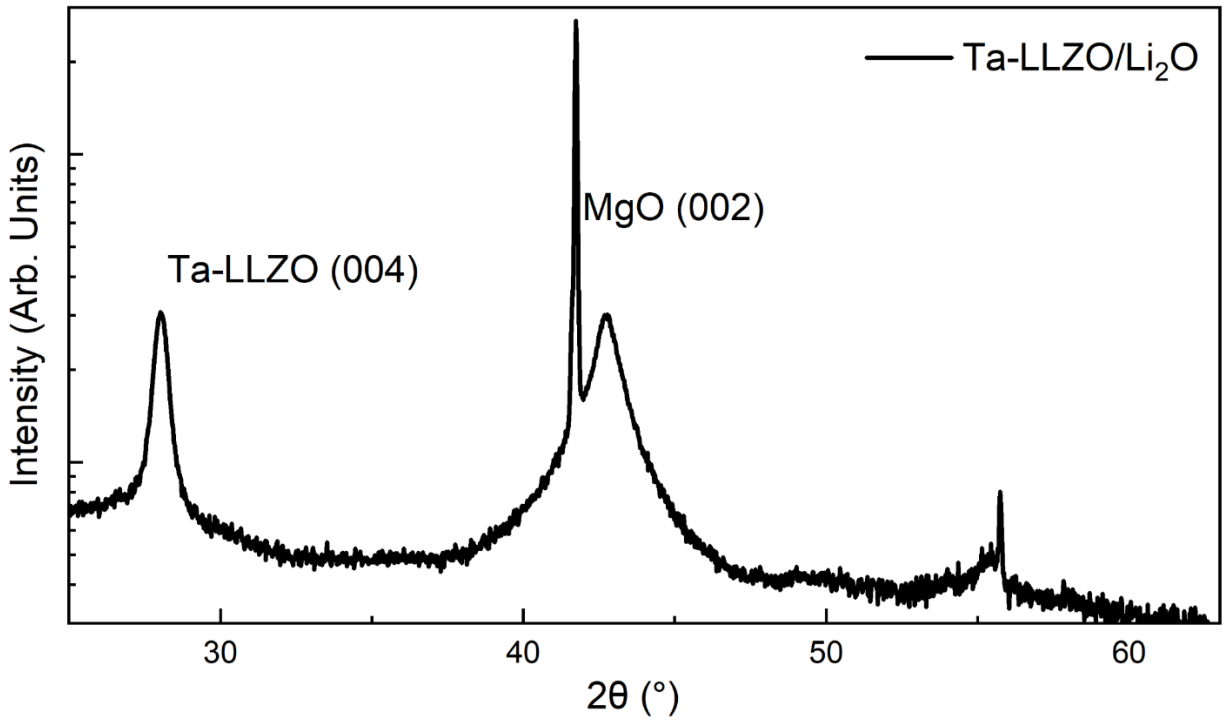

Figure 4.6 XRD pattern showing intensity vs 2θ of Ta-LLZO. Obtained by integrating the GADDS frames from Figure 5.3 using Diffrac.Eva.

The XRD patterns obtained by integrating the area detector frames show distinct Ta-LLZO peaks at around 28.4°, which indicate a lattice constant of 12.51 Å. This is smaller than bulk cubic LLZO, which has a lattice constant of around 13.09 Å. This is likely due to lattice mismatch with the MgO, which has a lattice constant of 4.211 Å. In addition, the Li_2O inclusion can also affect the Li and O concentration in the unit cell, affecting its lattice parameter. The XRD patterns obtained using the C2 area detector show a double peak around 42.8°, which is attributed to the MgO substrate. The double peak appearing is inconsistent and varies by sample and scan. Some clean MgO substrates, when scanned, would produce a single, sharp MgO (002) peak, while other substrates would exhibit a double peak. Some scans would even show up to five separate peaks near the MgO (002) peak. Figure 4.7 shows multiple Ta-LLZO films deposited on MgO substrates with an inset zoomed in on the MgO (002) peak. Some samples exhibited five peaks, while others showed a double peak around MgO (002).

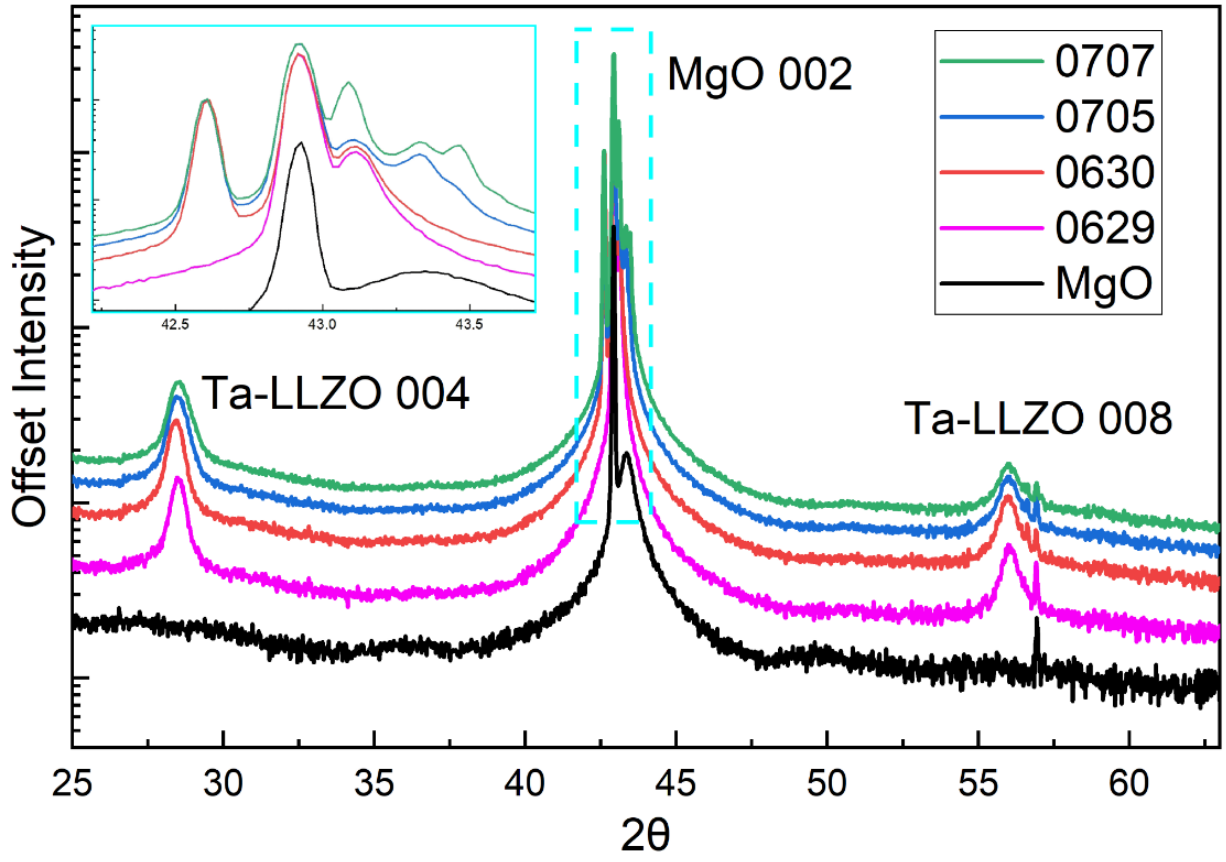

Figure 4.7 XRD Pattern of different Ta-LLZO samples deposited on MgO. Inset: Zoomed in view showing multiple MgO (002) peaks, indicated by the dashed cyan box.

The double peak can be attributed to either background reflections related to the area detector and/or XRD instrument, or it can be attributed to poor substrate quality. Existing studies on the quality of MgO substrates show inconsistencies in substrates obtained from different vendors and even within the same production batch[207,208]. These substrates may not be single crystal and can instead consist of multiple domains, appearing as multiple peaks in Ω-scans near the MgO (002) reflection. This is difficult to measure, however, using the instruments available in the XCC, as the C2 does not allow for omega scans and fine alignment, and the XPert does not have a monochromator and includes spectral lines. Thus, it is difficult to determine if there are additional double peaks that were present in C2 scans.

The XPert was used to measure additional XRD and GIXRD patterns of the deposited Ta-LLZO thin films (Figure 4.8). Because it does not have a monochromator, interfering components such as the $K\alpha_1$, $K\alpha_2$, $K\beta$, and Tungsten (W) $L\alpha_1$ lines are present in the 2θ-ω scans. However, the four-circle goniometer allows for much finer sample alignment than the C2. XRD patterns using the XPert show a distinct peak at 26.0°, while the GI-XRD patterns show peaks at 28.3° and 69.0°.

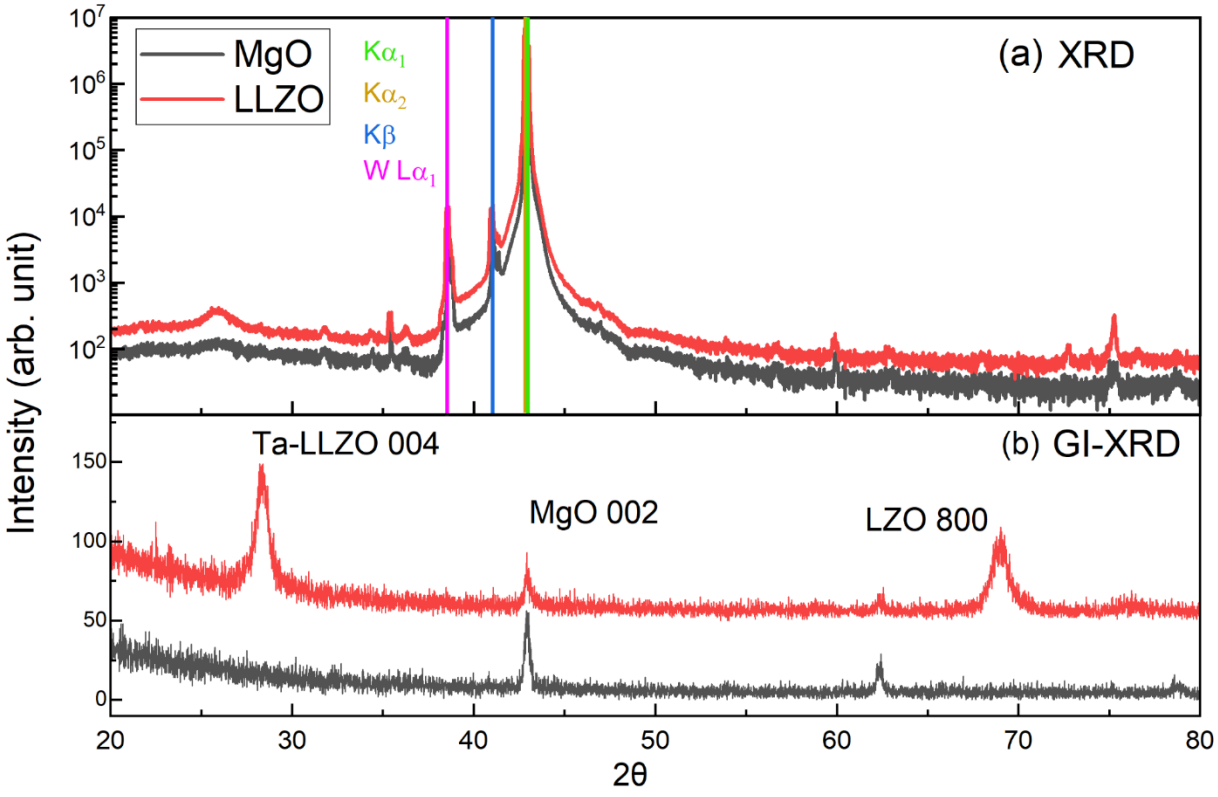

Figure 4.8 XRD and GI-XRD patterns of Ta-LLZO generated using the X'Pert instrument.

The GI-XRD peak at 28.3° is consistent with Ta-LLZO with a lattice constant of around 12.566 Å. The peak at 26.0° in the XRD pattern can also be attributed to LLZO, although it shows a lattice parameter of around 13.761 Å. The reason for this could be due to a tilt in the crystal lattice, which is discussed in section 4.2.2. The peak that occurs at 69.0° likely corresponds to the $La_2Zr_2O_7$ phase (LZO). This would indicate Li loss in the film, which can be due to Li evaporation at higher deposition temperatures. At high temperatures, a phase transition can occur to the

delithiated LZO phase, necessitating an increase in the Li content to compensate[137]. To resolve this issue, films were deposited at lower temperatures and with an increase in the Li_2O layer. This resulted in additional Li being added to the film and less evaporation due to the high temperatures.

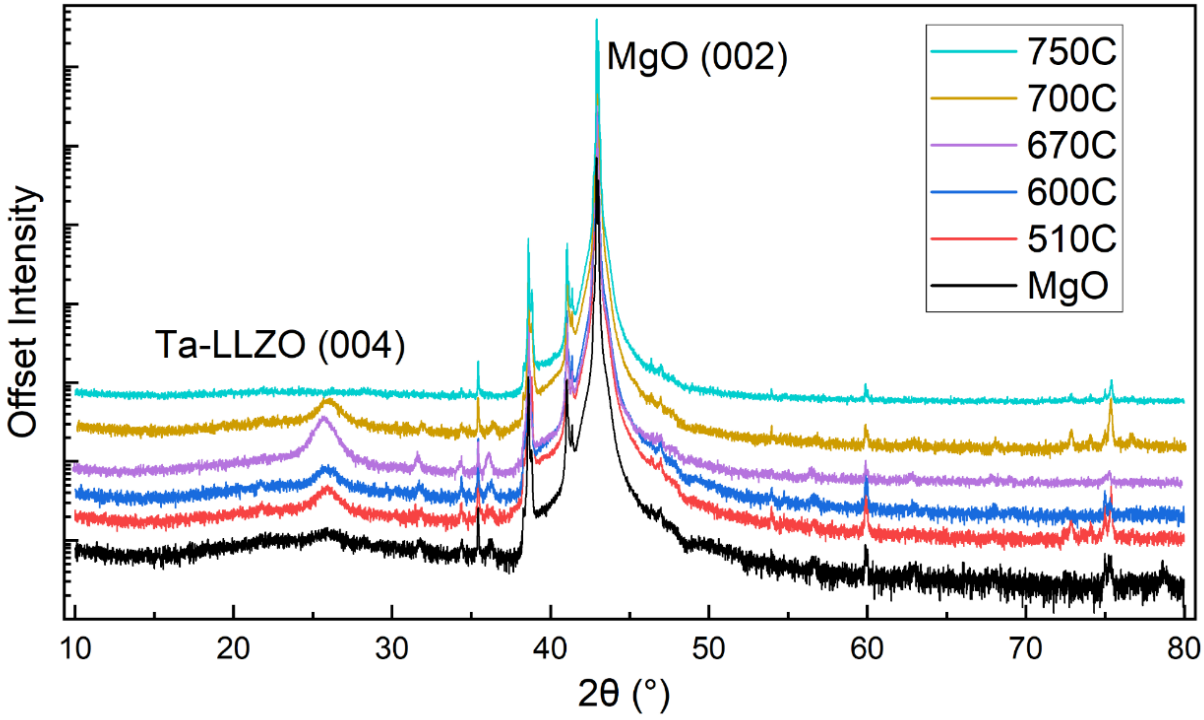

Figure 4.9 Temperature dependent XRD patterns of Ta-LLZO

Investigation into the effects of temperature on the Ta-LLZO deposition provides insight into which temperatures promote the LLZO growth. Figure 4.9 illustrates that a substrate temperature around 670 °C provides the most prominent Ta-LLZO peak without any contaminant peaks such as LZO. Similarly, GI-XRD patterns of films deposited at 670 °C show strong Ta-LLZO peak without the contaminant LZO peak (Figure 4.10).

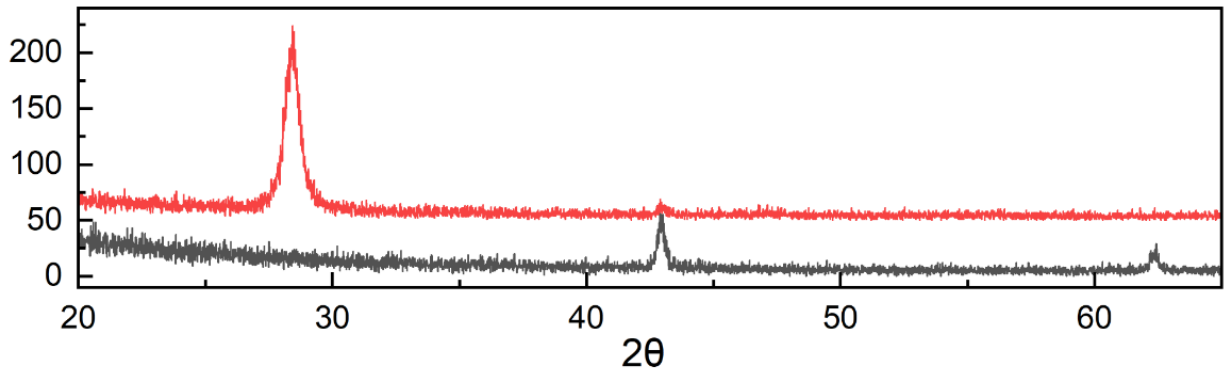

Figure 4.10 GI-XRD pattern of Ta-LLZO deposited at 670 °C

4.2.2 XRD chi tilt

The XRD 2θ-ω patterns generated with GADDS show the intensity peaks at offset angles when compared to the substrate peak. In the area detector frames, this is representative of the different χ angles that are measured simultaneously alongside the 2θ range. The incomplete rings along with the χ angle offset indicate single-crystal-like textured epitaxial thin films. This can be further seen in XRD scans generated using the XPert with an intentional chi (χ) offset. The C2 was used to determine the 2θ angle representing the Ta-LLZO (004) peak based on the generated intensity frames. This value was transferred to the XPert instrument, where a χ-scan aligned at the determined 2θ angle generates the pattern shown in Figure 4.11.

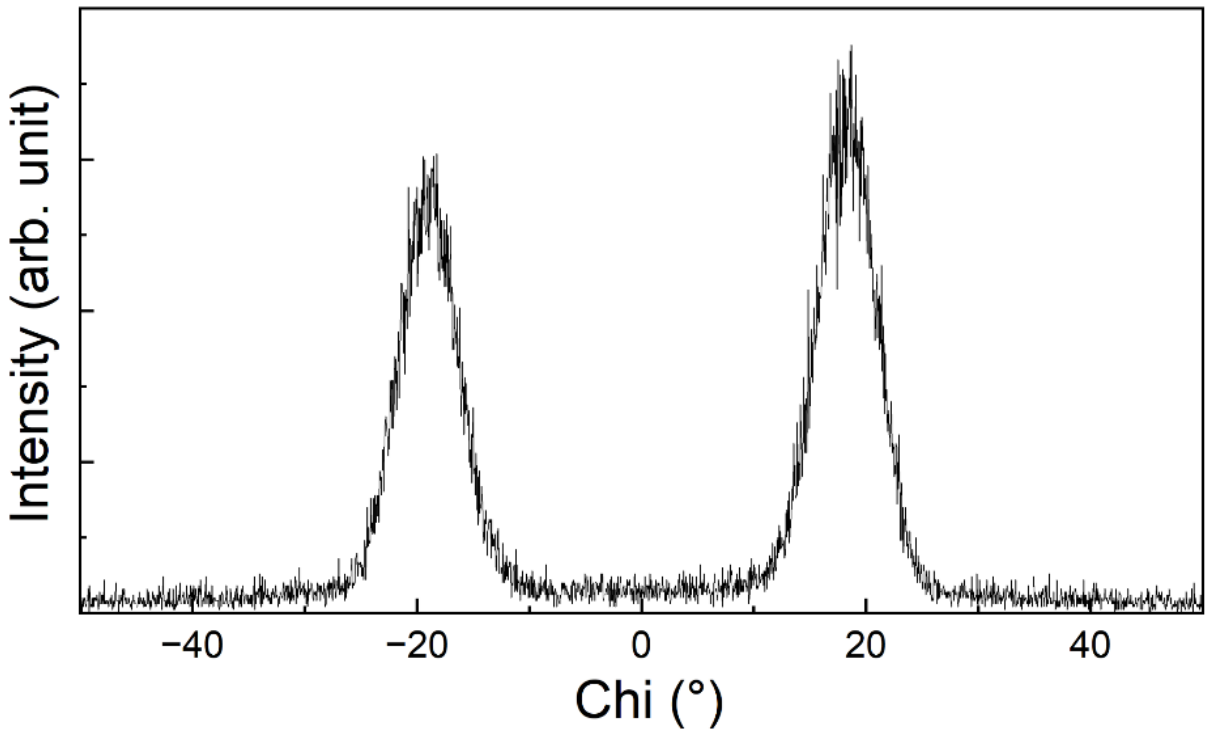

Figure 4.11 Intensity vs Chi XRD pattern showing tilt in the film.

This pattern shows two distinct peaks at around -18.8° and +18.5°. Aligning the Ta-LLZO thin film along a χ angle of +18.5° generated the 2θ-ω pattern in Figure 4.12. This pattern shows

much more distinct Ta-LLZO (004) and (008) peaks at around 28.18° and 58.28°, while the MgO (002) is much less defined. This indicates that the sample is better aligned along the film peaks, suggesting that the Ta-LLZO film grows at a ~19° tilt compared to the substrate MgO.

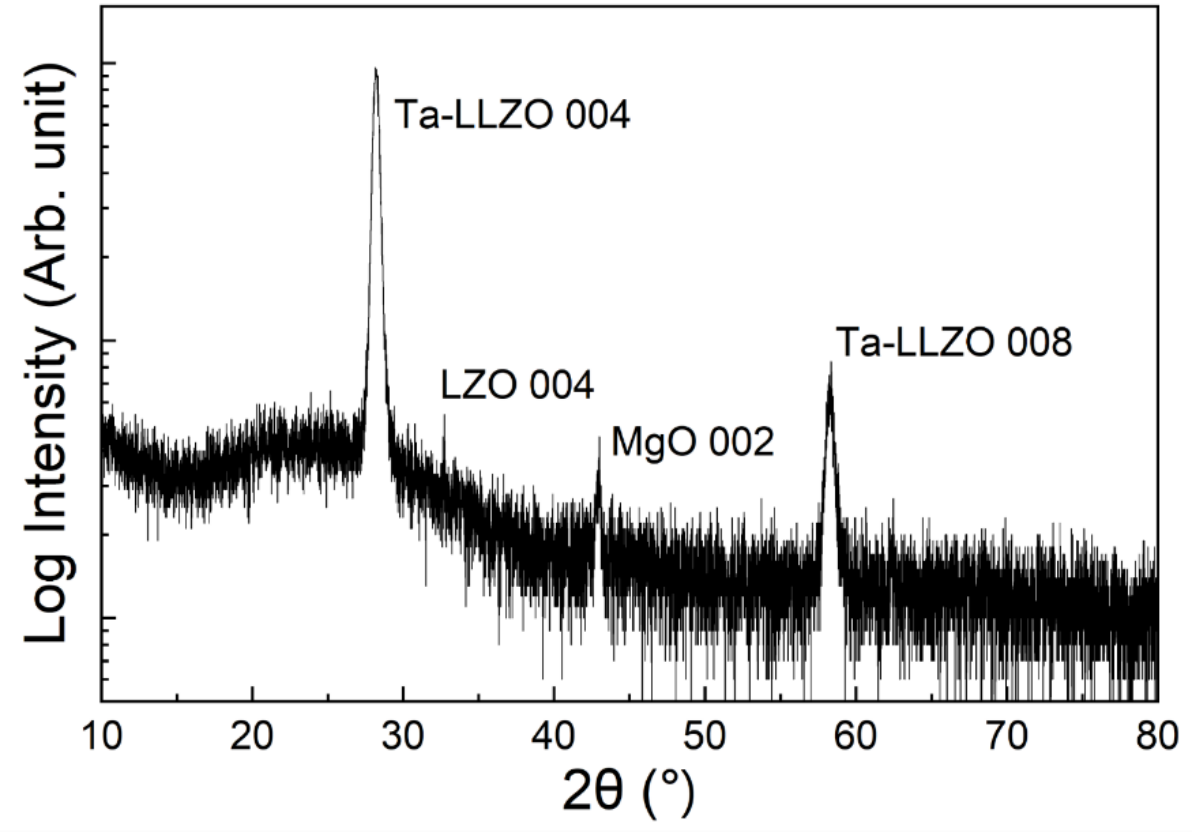

Figure 4.12 XRD pattern of Ta-LLZO measured with Chi tilt of 19°.

The Ta-LLZO thin films are likely growing at the χ-offset of approximately 19°. The exact origins of this behavior have not been determined. The c-axis lattice parameter of the Ta-LLZO films determined using Bragg's law is 12.65 Å, which has a lattice mismatch of less than 1% with the MgO substrates. However, the LLZO peaks are seen when the sample is offset. As shown in Figure 4.13, a 19° χ tilt results in a more significant lattice mismatch.

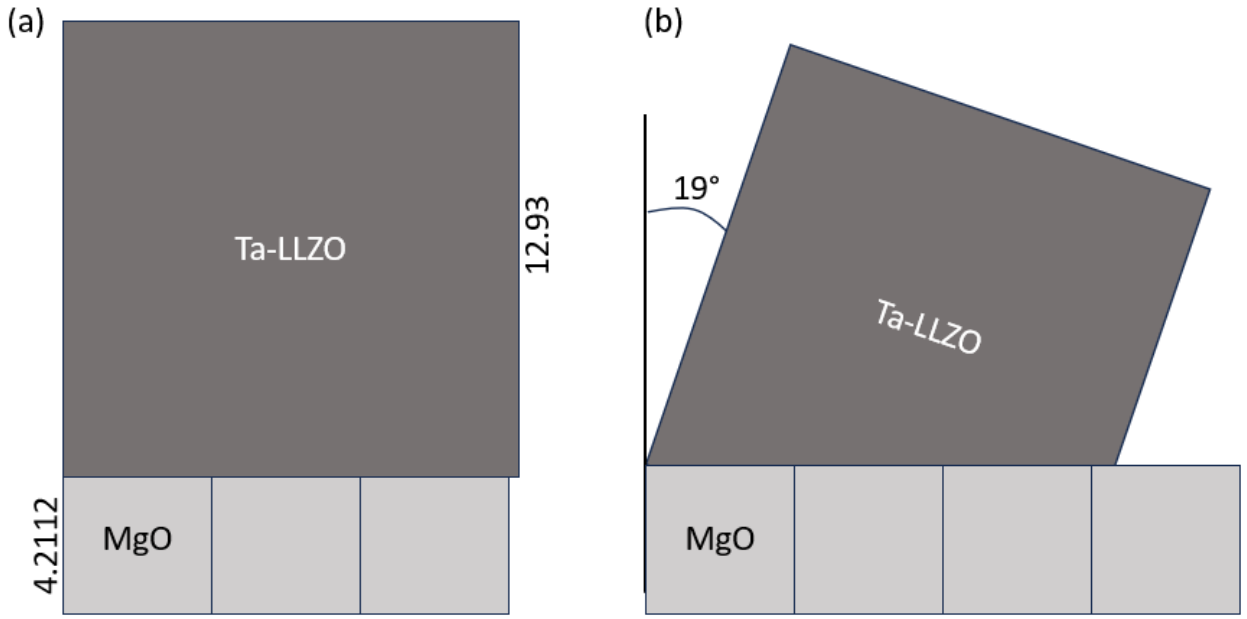

Figure 4.13 (a) Lattice mismatch of Ta-LLZO on MgO. (b) Diagram showing Ta-LLZO 19° tilt

The tilt in the Ta-LLZO thin film can also be seen in SEM images of the cross-sectional area of the samples (Figure 4.14). The angled lines that can be seen suggest tilt in the Ta-LLZO thin films.

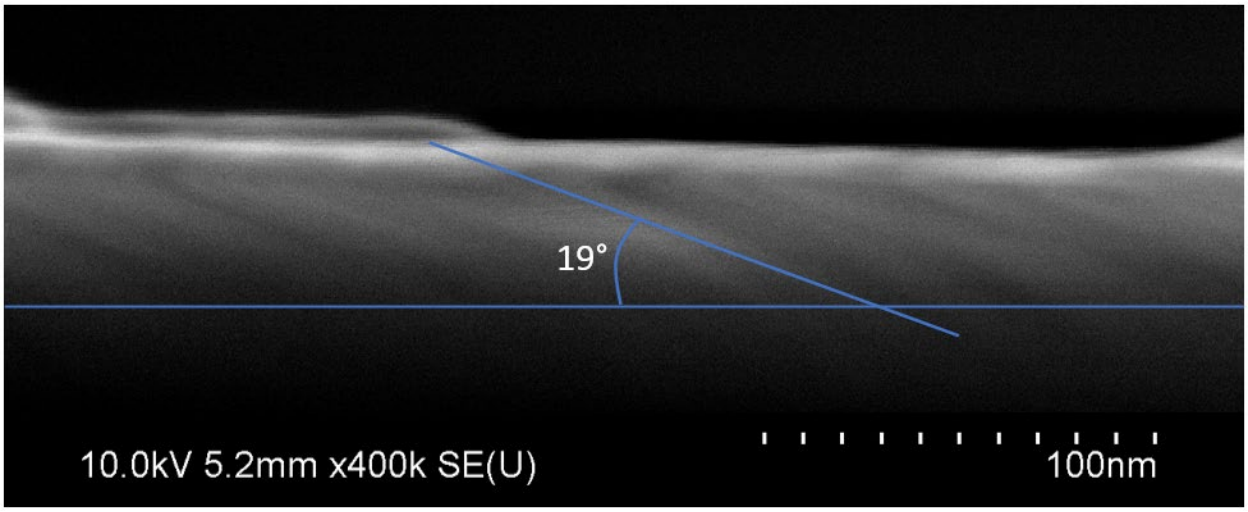

Figure 4.14 SEM cross-section of Ta-LLZO showing 19° tilt.

Figure 4.14 shows φ-scan XRD patterns of the MgO (002), Ta-LLZO (116), and Ta-LLZO (004) planes fixed at their respective 2θ angles, indicating 4-fold symmetry. This confirms the epitaxial growth of Ta-LLZO (004) on MgO (001).

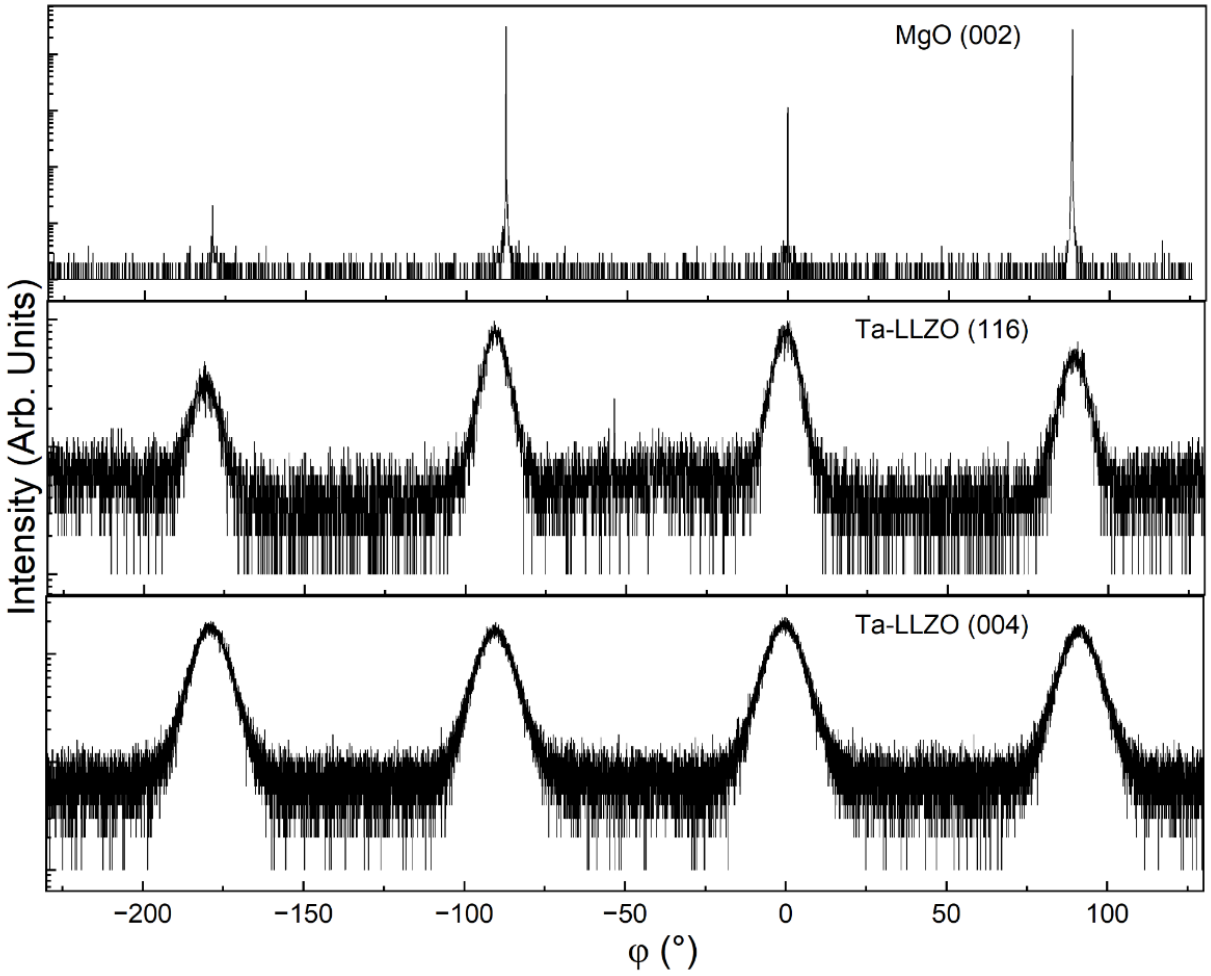

Figure 4.15 XRD φ-scans of MgO (002), Ta-LLZO (116), and Ta-LLZO (004) showing four-fold symmetry, indicating single-crystal like growth.

Of the previous reports on doped LLZO thin films, there is only one published report of Al-doped LLZO deposited on GGG (001) and GGG (111) substrates. Thus, we have demonstrated the epitaxial single-crystal-like growth of Ta-LLZO on MgO (001) substrates.

4.2.3 Ta-LLZO LE soaking

To investigate the solid-electrolyte interface that can form between LLZO and liquid electrolyte, Ta-LLZO thin films were exposed to a liquid electrolyte solution and then examined using XPS and sputtering to identify the compounds that react to form the interface. This also provides insight into how the interface forms and how deep the interaction between the LLZO and electrolyte penetrates the film.

Samples deposited in the QMC lithium PLD chamber were exposed to the $LiPF_6$/PC electrolyte for a period of 3 days before being rinsed to remove excess electrolyte. Spectra analysis was performed using Tougaard type background. P 2p, Zr 3d, and La 3d peaks were fitted with a fixed theoretical area ratio and fixed full width half maximum (FWHM). P 2p and Zr 3d peaks were fitted using reference literature values[209].

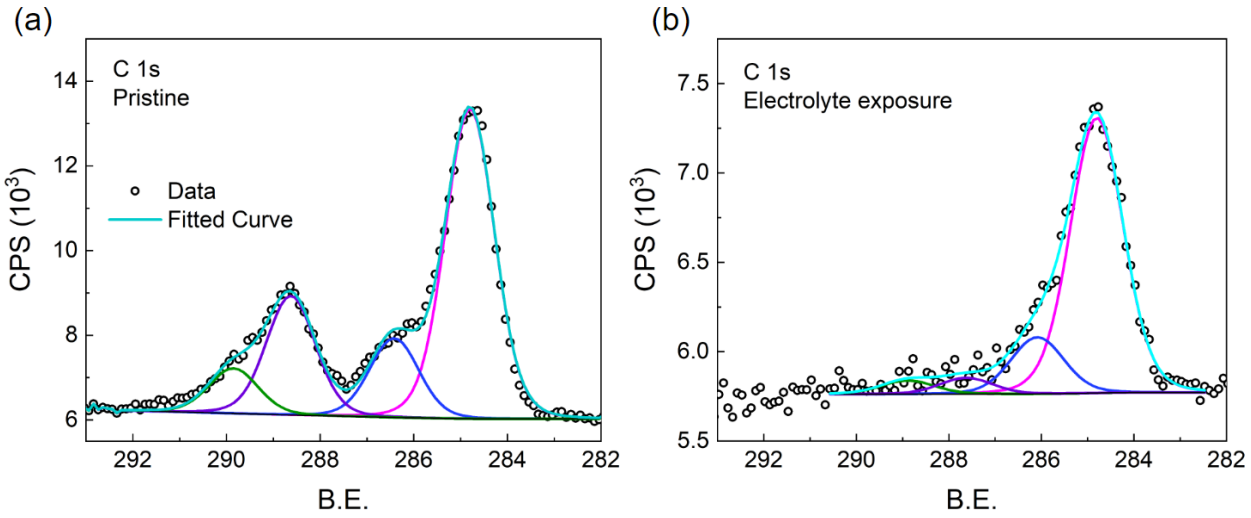

Figure 4.16 C 1s spectra of Ta-LLZO (a) before and (b) after electrolyte exposure.

Figure 4.16 shows the C 1s spectra before and after electrolyte exposure. The C 1s spectra exhibits a peak at a binding energy of 284.8 eV, which is attributed to hydrocarbons[210]. The peak at 286.4 eV is attributed to ethers, a peak at 288.6 eV is attributed to ketones and aldehydes, and a

peak at 289.9 eV is attributed to carbonates[209,211]. Carbon contamination is inevitable due to the air exposure when transferring samples from the PLD chamber to NIST. This is shown in the pristine sample before LE soaking. One such contaminant that can appear is Li_2CO_3, which is formed when LLZO is exposed to moisture in the air[212].

After exposing the sample to the electrolyte, the C 1s signals showed lower intensity compared to the pristine Ta-LLZO samples, with the largest peak associated with hydrocarbons at 284.8 eV[211]. A shoulder at 286.1 eV can be attributed to C–O bonds[209]. The minimal peaks at 287.6 and 288.9 eV suggest that some surface contaminants are removed upon electrolyte exposure[209]. $LiPF_6$ decomposition can generate HF, which can then react with the Li_2CO_3 on the sample surface through the following reactions[213]:

$$LiPF_6 + H_2O \rightarrow LiF + POF_3 + 2HF \quad (11)$$

$$Li_2CO_3 + 2HF \rightarrow 2LiF + H_2CO_3 \quad (12)$$

Another possible reaction that can occur is[214]:

$$LiPF_6 + 2Li_2CO_3 \rightarrow 2CO_2 + 4LiF + F_2PO_2Li \quad (13)$$

These possible reactions that can occur suggest that the removal of surface contaminants such as Li_2CO_3 result in lower carbon contamination.

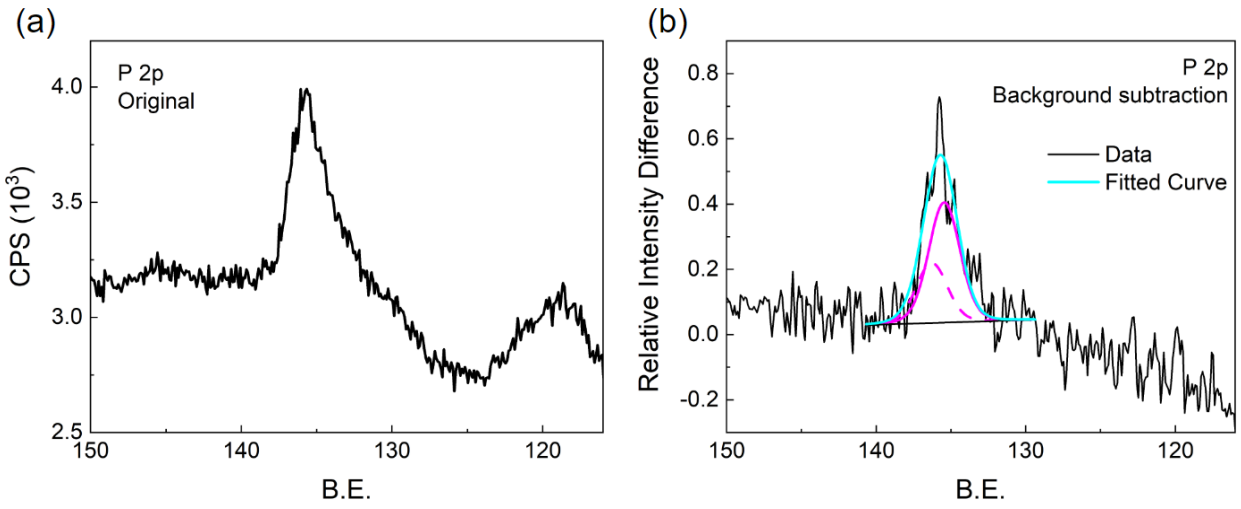

Figure 4.17 P 2p spectra of Ta-LLZO after electrolyte exposure (a) before and (b) after background subtraction. A background spectrum was taken from Ta-LLZO without electrolyte exposure. Note that intensity in (b) is in Relative Intensity Difference. The P $2p_{3/2}$ is shown with a solid line and P $2p_{1/2}$ is shown with a dashed line.

The P 2p spectra in Figure 4.17 shows a peak at around 118.8 eV which can be attributed to a La $4d_{3/2}$ plasmon peak. The slope from 124 eV to 130 eV can also be due to the La 4d signal, necessitating background subtraction to obtain the P 2p spectra without the effects of the La 4d[214]. Background from La 4d was subtracted using a P 2p scan of the same region in a Ta-LLZO sample without exposure to the electrolyte. This gave a distinct P 2p peak range. Background subtraction was performed after normalizing the maximum intensity to 1 for both the pristine and exposed Ta-LLZO spectrum. While the original intensity information is lost, this gives information regarding the P 2p spectra and its relative intensity difference without the La 4d spectra. Peak fitting from 130 eV to 139 eV shows a large peak around 136 eV composed of a P $2p_{3/2}$ peak at 135.4 eV that can be attributed to $Li_xPO_yF_z$, and a P $2p_{1/2}$ peak at 136.3 eV[213,215]. The P $2p_{3/2}$ peak representing $Li_xPO_yF_z$ can include compounds such as $LiPO_2F_2$ and Li_2PO_3F[216].

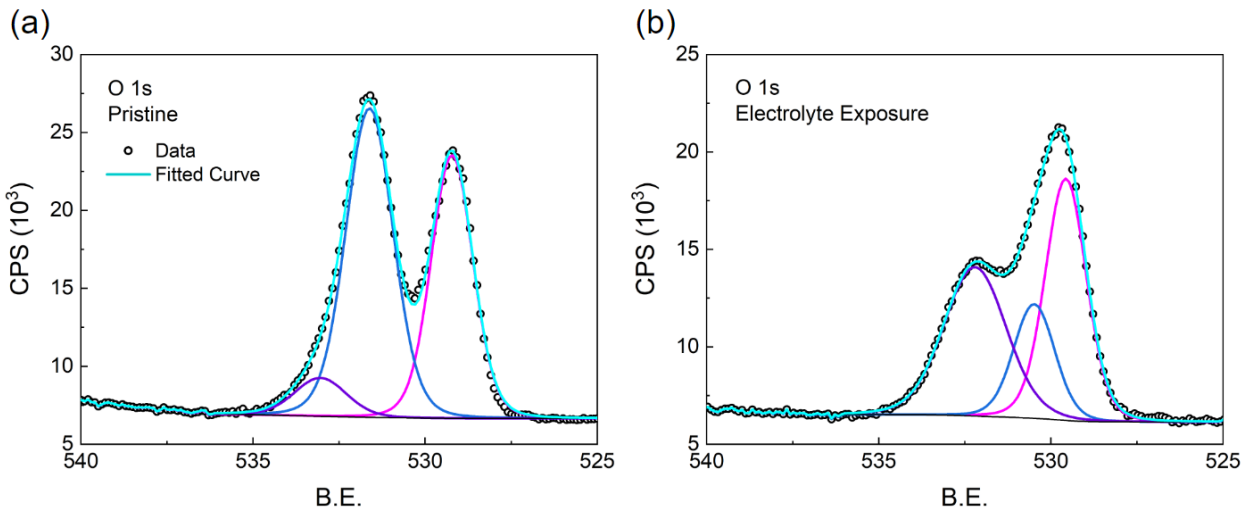

Figure 4.18 O 1s spectra of Ta-LLZO (a) before and (b) after electrolyte exposure.

In the pristine O 1s spectrum before soaking in the LE shown in Figure 4.18a, the peak at 529.2 eV is attributed to metal oxides, while the peaks at 531.6 eV and 533.0 eV are attributed to carbonates and nitrates, respectively[209]. The N 1s spectrum overlaps with the Ta 4p spectrum, making it difficult to specify the nitrate compound present. The carbonate observation is consistent with the C 1s spectrum, which also shows peaks relating to carbonates.

Exposure to the electrolyte results in an increase in the intensity of the metal oxide peak compared to the peaks around 532 eV, seen in Figure 4.18b. Two peaks around 530 eV are attributed to metal oxides, which may be due to deformed LLZO structure that forms because of the electrolyte soaking[209]. The peak at 532.2 eV is attributed to phosphorus compounds, which can include chemicals with P–O–P links, $LiPO_2F$, and Li_2POF. There may be a smaller carbonate peak around 531 eV, but it is difficult to distinguish due to overlap with the large phosphorus compound peak[209,217].

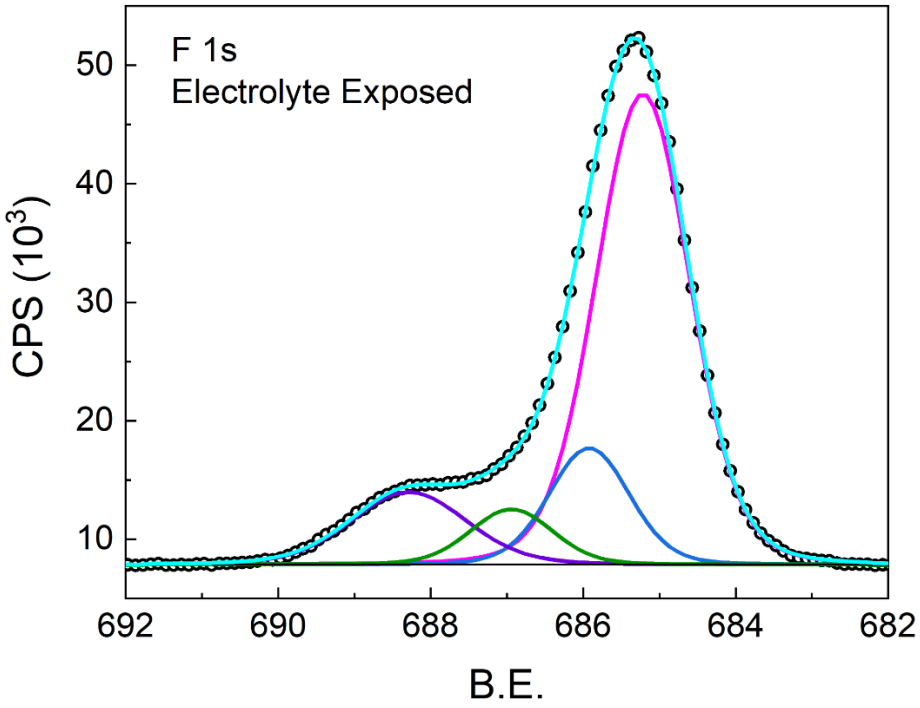

Figure 4.19 F 1s spectrum of Ta-LLZO after electrolyte exposure.

The highest peak at 685.3 eV in the F 1s spectrum in Figure 4.19 is attributed to LiF and LaF_3[209,210]. The peak at 685.9 eV is attributed to ZrF_4 while the peak at 688.3 eV is attributed to P–F bonding in Li_xPF_y and $Li_xPF_yO_z$[209,210,215]. The last peak at 686.9 eV can be attributed to fluorinated LLZO compounds. The formation of LiF is explained in equations 11-13, while LaF_3 and ZrF_4 can form as a result of the LLZO reacting with the HF generated by $LiPF_6$ decomposition, shown in equation 11. Other variations of these compounds that are partially fluorinated can be attributed to the remaining peak.

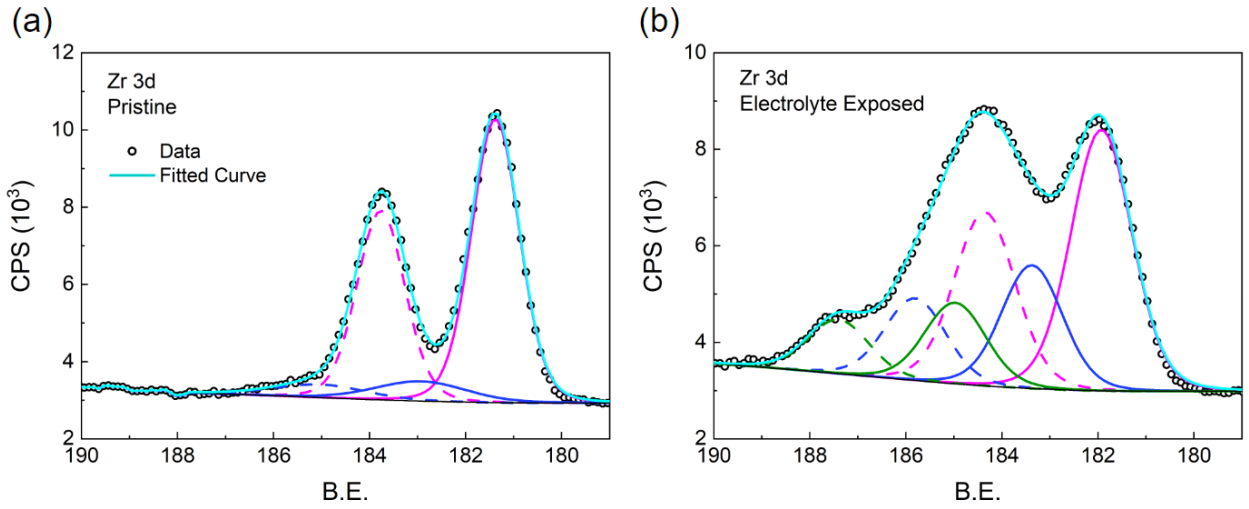

Figure 4.20 Zr 3d spectra of Ta-LLZO (a) before and (b) after electrolyte exposure. Zr $3d_{5/2}$ peaks are shown with solid lines, and Zr $3d_{3/2}$ peaks are shown with dashed lines.

Figure 4.20 shows the Zr 3d spectrum of Ta-LLZO before and after electrolyte exposure. The pristine Zr 3d spectrum shows the main Zr $3d_{5/2}$ and Zr $3d_{3/2}$ peaks at 181.4 eV and 183.8 eV, respectively, which are associated with LLZO. Other broad peaks at 182.9 eV and 185.0 eV are attributed to partially decomposed LLZO at the surface[210]. The wide FWHM suggests that the LLZO is not decomposed to a single component but rather a mixture of oxides. This can be indicative of carbonates such as Li_2CO_3 on the surface of the film, which is supported by the carbonate peaks shown in the C 1s spectrum[211].

After electrolyte exposure, a pair of Zr $3d_{5/2}$ and Zr $3d_{3/2}$ peaks at 181.9 eV and 184.4 eV can be attributed to LLZO. A pair of peaks at 183.4 eV and 185.8 eV is attributed to ZrO_2, while the peaks at 185.0 eV and 187.4 eV are indicative of ZrF_4[210]. This is consistent with the results from the previous spectrums, which show evidence of LLZO and ZrO_2 in the O 1s spectrum and ZrF_4 in the F 1s spectrum.

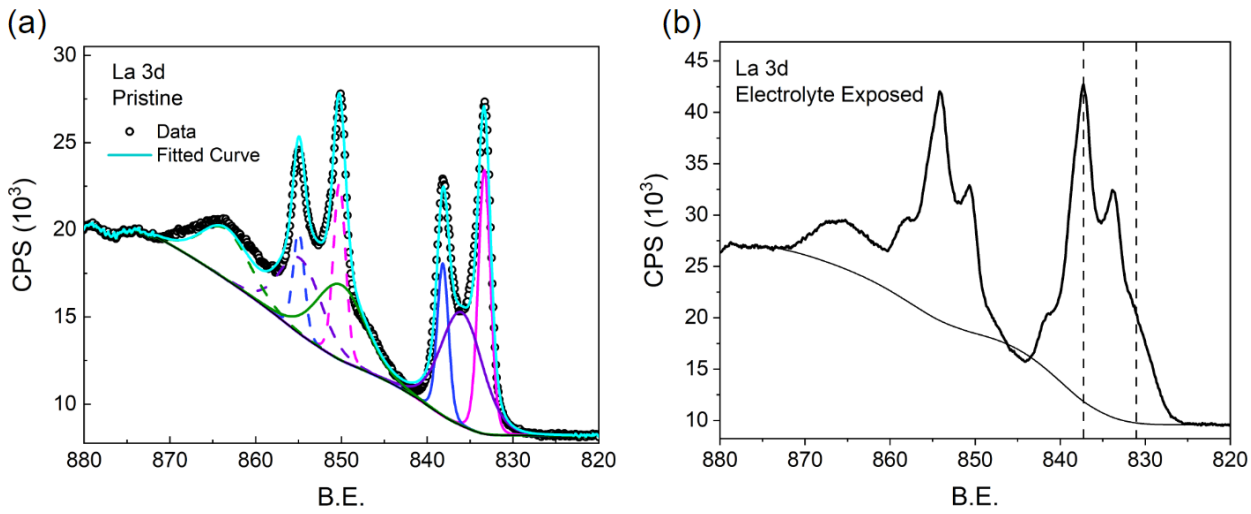

Figure 4.21 La 3d spectra of Ta-LLZO (a) before and (b) after electrolyte exposure. La $3d_{5/2}$ peaks are shown with solid lines, and La $3d_{3/2}$ peaks are shown with dashed lines. In (b), gray dashed lines are at 831 eV and 838.3 eV as guides.

Figure 4.21 shows the La 3d spectrum before and after electrolyte soaking. The pristine La 3d spectrum shows a La $3d_{5/2}$ main peak at 833.2 eV and a La $3d_{3/2}$ main peak at 850.2 eV. La_2O_3 has been reported to show peaks at 834.9 eV and 851.7 eV, which is in agreement with the peak separation seen in the La 3d spectrum[214]. Two satellite peaks due to bonding and antibonding components with a ligand are also present, along with a plasmon peak at higher B.E[214]. These peaks appear at 838.2 eV, 836.0 eV, and 850.0 eV, respectively, for La $3d_{5/2}$, and are observed at 850.2 eV, 855.0 eV, and 863.5 eV, respectively, for La $3d_{3/2}$.

Upon electrolyte exposure, large shoulders were observed on both the lower and higher B.E sides. A large shoulder around 831 eV can be due to Auger line from F, which is supported by the F 1s spectrum. The highest relative intensity shifts to 837.3 eV, which can be attributed to LaF_3, which has a peak at around 837 eV for the La $3d_{5/2}$ peak[218,219]. The shoulder at around 840 eV can also be attributed to LaF_3[218]. The presence of fluorinated lanthanum peaks agrees with the peaks observed in the F 1s spectrum. Other components may also be present but are indistinguishable

from the existing peaks due to overlap. It is expected that LaF_3 exists on the surface of the electrolyte exposed samples, as well as other oxides such as decomposed LLZO compounds.

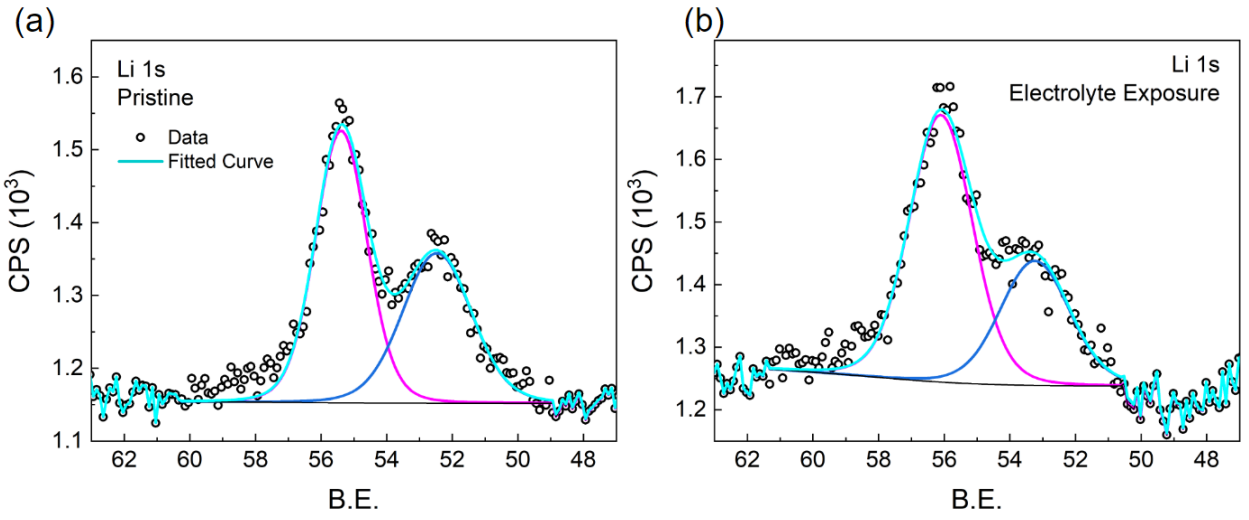

Figure 4.22 Li 1s spectra of Ta-LLZO (a) before and (b) after electrolyte exposure.

The Li 1s spectrum before and after gating is shown in Figure 4.22. The Li 1s spectrum overlaps with the Zr 4s peak. In the pristine sample, Li 1s is observed at 55.4 eV, while the Zr 4s peak is observed at 52.5 eV. This Li 1s peak is attributed to LLZO, but also includes surface contaminants such as Li_2CO_3 due to air exposure during sample transit[210].

After exposure to the electrolyte, the Li 1s peak is observed at 56.1 eV while Zr 4s appears at 53.1 eV. This can be attributed to LiF being observed in the sample, as LiF is reported to have a peak ranging from 55.7 eV to 56.7 eV[210]. Other surface components, such as Li_xPF_y and $Li_xPF_yO_z$ are also reported to be observed around 56.3 eV, and so can be contributing to the observed peaks. Thus, the Li 1s peak in Figure 5.20 can be an overlap of multiple components such as LiF, $Li_xPF_yO_z$, and LLZO.

In the pristine samples, the XPS spectrum show signals that were mostly from the LLZO. Carbon contaminants such as Li_2CO_3 were also present due to the air exposure that occurs during

sample transport, which allows moisture and air to react with the LLZO surface. Electrolyte exposure shows the removal of these surface carbon contaminants, but also the presence of fluorine compounds such as LiF, LaF_3, ZrF_4, and $Li_xPF_yO_z$. HF, which is an expected decomposition product from equation 11, was not observed. This was likely due to further reactions of HF and LLZO, which can produce fluorinated metals such as LaF_3 and ZrF_4. This shows that while electrolyte exposure can be an effective way to remove surface contaminants, the interaction between the electrolyte and the Ta-LLZO film produces other fluorinated compounds that can affect the transport properties of LLZO.

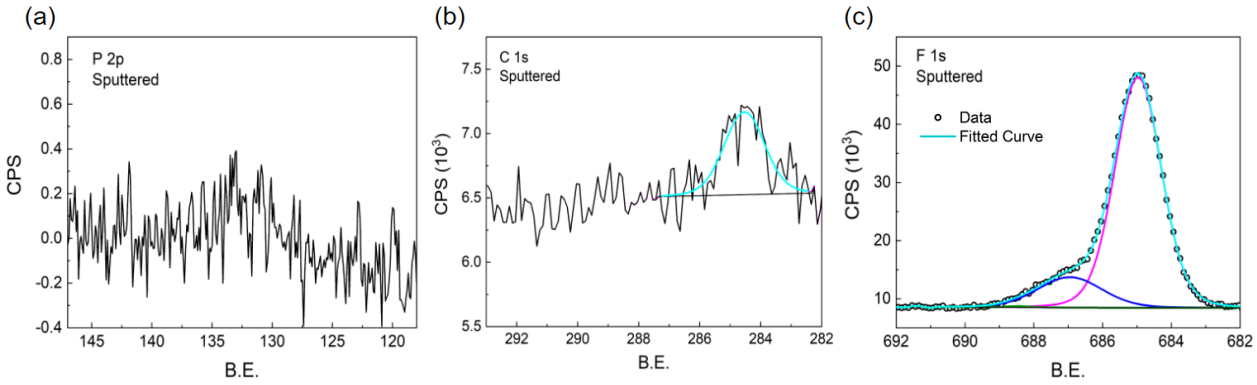

Figure 4.23 (a) P 2p, (b) C 1s, and (c) F 1s spectra after 30 sec sputtering of Ta-LLZO exposed to the electrolyte. (a) is a P 2p spectrum after background subtraction with the intensity in Relative Intensity Difference.

Sputtering the surface of the sample provides insight into how the electrolyte exposure affects the bulk of the film rather than just the surface. Figure 4.23 shows the P 2p (with background subtraction), C 1s, and F 1s spectra after sputtering for 30 sec. Sputtering shows significant changes in the measured spectra when compared to the electrolyte exposed LLZO. The P 2p signal is negligible, and the F 1s spectrum has nearly negligible signal from Li_xPF_y and $Li_xPF_yO_z$. The hydrocarbon peak at 284.5 in the C 1s spectrum also has significantly reduced intensity. The F 1s spectrum shows a peak at 685.0 eV, which can be attributed to LiF and LaF_3,

and the peak at 687.0 eV is attributed to an overlap of the ZrF_4 and decomposed LLZO. This shows that the organic compounds Li_xPF_y and $Li_xPF_yO_z$ were accumulated on the surface of the film and were removed easily by sputtering, suggesting that there is little interaction with the LLZO and these compounds.

The overlapped spectra of F 1s, La 3d, Zr 3d, and O 1s in Figure 4.24 shows the change with progressive sputtering times. Black indicates the film before sputtering, pink shows a 2-minute sputter, blue shows 4 min, purple is 6 min, and green is a 14 min sputter time. Given a sputtering rate around 0.75 nm/min, the estimated sputtered depths are 0 nm, 1.5 nm, 3 nm, 4.5 nm, and 10.5 nm.

The most significant shift to the spectra occurred in the first 2 min sputtering, which removed the top 1.5 nm surface layer. Components such as carbonates, Li_xPF_y, and $Li_xPF_yO_z$ were nearly completely removed after 30 seconds, as seen in Figure 4.23. The removal of these surface components resulted in a higher intensity of the La 3d, Zr 3d, and O 1s peaks, while a decrease in fluorine is observed in the F 1s and La 3d spectrum. The additional peaks in the La 3d spectra, a shoulder around 841 eV and 858 eV attributed to LaF_3[218], were not observed after the sputtering.

The Zr 3d spectrum shows that after 2 min sputtering, the overall peaks shifted to a lower B.E. In the O 1s spectrum, the metal oxide peak intensity increased, while the peak due to phosphorus compounds at 532 eV decreases after 2 min sputtering. In the Zr 3d, O 1s, and La 3d spectra, the peaks overlapped well with a sputter time longer than 2 minutes, suggesting that the electrolyte soaking mostly affected the 1.5 nm surface layer.

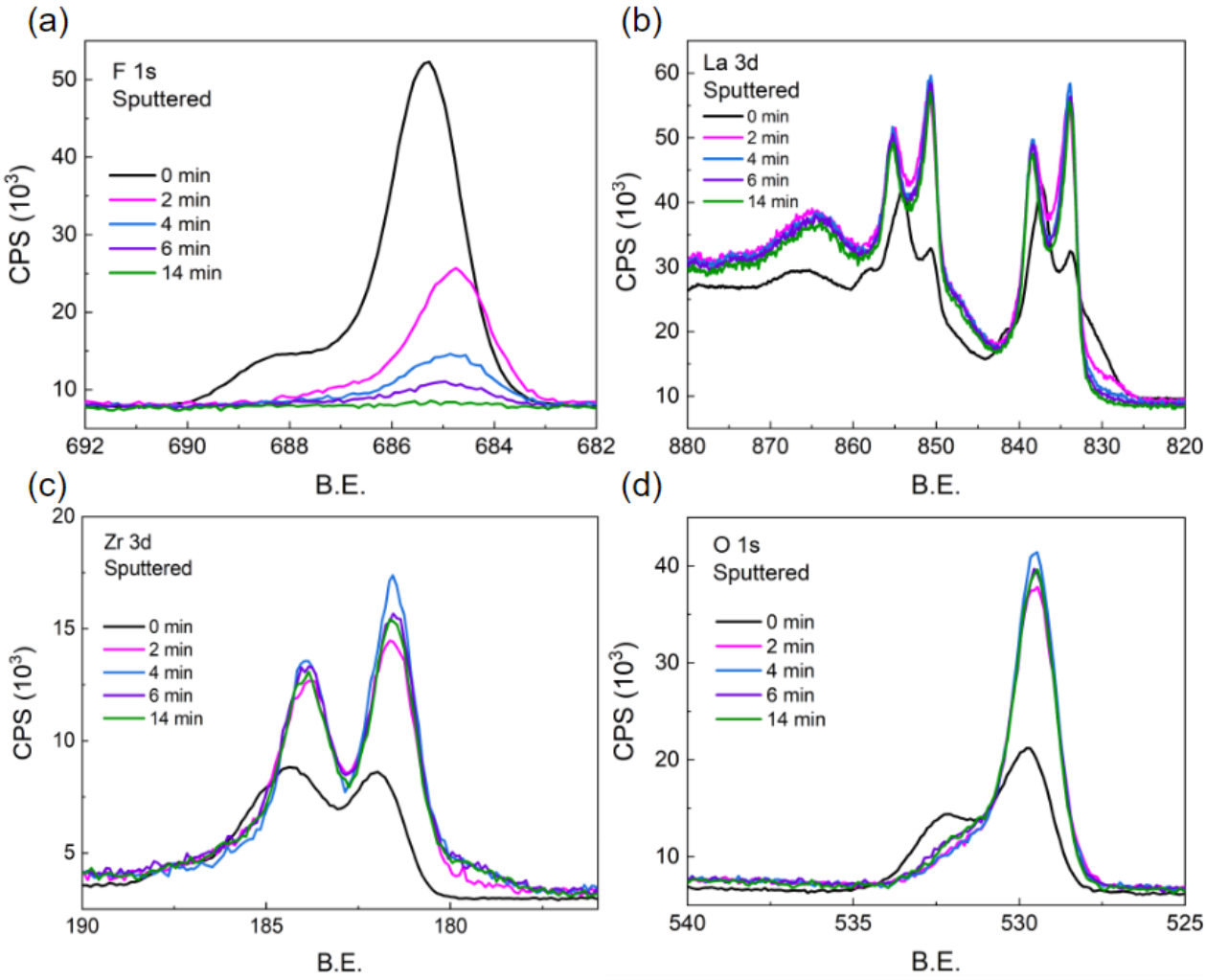

Figure 4.24 (a) F 1s, (b) La 3d, (c) Zr 3d, and (d) O 1s spectra of 0 min, 2 min, 4 min, 6 min, and 14 min sputtering. Black is 0 min (before sputter). Pink, blue, purple, and green are the 2 min, 4 min, 6 min, and 14 min sputter times, respectively.

While the contaminants showed less intensity after 2 min sputtering, fluorinated compounds such as LiF and LaF_3 were still observed. The peak minima at 836.4 eV and 853.3 eV in the 2 min sputtered La 3d spectrum is higher than in the spectra of longer sputter times. Peak intensity of the F 1s peaks attributed to LiF, LaF_3, and ZrF_4 decreased consistently as sputtering time increased. A slight shoulder which decreased from 0 min to 4 min sputtering in the La 3d spectrum at 830 eV is also consistent with fluorinated compounds observed deeper in the films.

The F 1s peak becomes nearly negligible after 14 min sputtering, suggesting that the fluorine was not able to penetrate past 10 nm into the sample.

While sputtering and XPS provides useful insight into the composition deeper into the material, damage from sputtering can affect the resulting data. For example, a shoulder around 178 eV increased from 4 min sputtering and above when compared to 2 min sputtering. A small shoulder at 532 eV in the O 1s spectrum also increases above 6 min sputtering. This may be caused by Ar^+ sputtering damage to the LLZO structure[220].

The spectra of the sputtered samples suggests that surface components such as carbonates, Li_xPF_y, and $Li_xPF_yO_z$, are able to be easily removed, while fluorinated metals such as LiF and LaF_3 are observed deeper in the films. This suggests that the LLZO reacts with the HF generated from $LiPF_6$ decomposition to generate decomposition products that can more significantly affect the structure. The generation of fluorinated metals within the LLZO film results in a solid-electrolyte interface between the LLZO SE and the $LiPF_6$ LE, which can greatly impact the lithium-ion transition and affect the charging rate and overall performance in LiBs. Overcoming the formation of fluorinated metal layers in the LLZO solid electrolyte may be a critical step towards utilizing LLZO in combination with a liquid electrolyte $LiPF_6$ for use as hybrid electrolytes in LiBs.

4.3 Conclusion

$LiCoO_2$ thin films were deposited on Nb-STO (111) and STO (100) in order to investigate a novel and efficient approach for the delithiation of the LCO cathode. The LCO films sputtered with Ne^+ to remove Li ions. Li^+ removal resulted in the formation of Co^{4+} and an increase in holes located at O atoms, indicating that both Co and O are involved in charge compensation caused by the Li ion removal.

Ta-doped LLZO and Li_2O were deposited in a multilayer thin film to investigate the interaction between the Ta-LLZO film and a liquid electrolyte $LiPF_6$. The Li_2O layers act as a lithium reservoir to improve the Li conductivity[137], while Ta is doped to aid in the formation of the cubic LLZO phase[135]. The Ta-LLZO thin films were exposed to 3 mol/dm^3 $LiPF_6$/PC electrolyte and examined using XPS to study how the films interact with the electrolyte. After electrolyte exposure, carbon-based contaminants such as Li_2CO_3 were shown to be reduced, while fluorinated metals, such as LiF, LaF_3, and ZrF_4, and $LiPF_6$ decomposed products, such as $Li_xPF_yO_z$, were found. Sputtering the sample easily removed further carbon-based contaminants and $Li_xPF_yO_z$, indicating that these compounds were found mostly at the surface of the sample[148]. Fluorinated metals such as LiF, LaF_3, and ZrF_4 were observed at depths up to 10 nm, suggesting that the LLZO interacts more strongly with HF than other decomposition products of the electrolyte. While the surface contaminants were shown to be easily removed via sputtering, the presence of fluorinated metals deeper in the film shows how a SEI forms as a result of the interactions between the Ta-LLZO film and $LiPF_6$ electrolyte[155].

Lithium-ion transfer between the solid and liquid electrolytes LLZO and $LiPF_6$ is of high importance due to the impact that it has on charging rate. Based on the XPS results, the compounds which penetrated deepest into the Ta-LLZO films were fluorinated compounds.

Overcoming the formation of fluorinated metals is critical to realize hybrid electrolytes that use the SE LLZO in combination with a LE containing $LiPF_6$. One potential reason for the formation of fluorinated metals is the presence of water contamination in the liquid electrolyte, which can form the HF that reacts with the LLZO and produces the fluorinated metals. Removal of the water contamination in the liquid electrolyte and on the surface of the solid electrolyte can thus reduce the SEI formation and improve the ion transfer between LLZO and $LiPF_6$[150,154,155].

Chapter 5. Conclusions and future work

Ionic liquid gating of $LaNiO_3$ thin films has been shown to increase the resistivity by over six orders of magnitude when gated in low vacuum. This is attributed to a rise in the oxygen vacancy concentration and a shift in the Ni valence state from Ni^{3+} to Ni^{2+}. XPS analysis of both pristine and IL gated $LaNiO_3$ thin films showed that the ratio of oxygen vacancies to lattice oxygens (O_v/O_{lat}) increased from 1.07 to 2.58. The ratio between Ni^{3+} and Ni^{2+} ions in the films decreased with IL gating, from 0.304 to 0.143. The changes in the oxygen vacancy concentration and Ni valence show non-trivial modification of Ni and O valence states, which can be attributed to electron filling of the Mott-Hubbard and charge-transfer bands. The increase in oxygen vacancies and shift in Ni valence enhances electron-electron correlation and decreases the bandwidth, resulting in a reduced overlap between the O 2p and Ni 3d bands. This opens the band gap and induces an insulating phase transition in $LaNiO_3$. The reliable manipulation of the electrical properties of perovskite nickelate thin films via IL gating opens new avenues for investigating the interplay between electron correlation and orbital effects and can be utilized in applications such as non-volatile memories for neuromorphic computing.

Future work in this field can investigate further methods of reliably reintroducing oxygen into the films to form a metallic state in the films after IL gating, such as using a NGV during IL gating or oxygen annealing gated samples to reintroduce oxygen into the films. There is also the possibility of utilizing IL gating to reduce the Ni valence state further, which could induce a phase transition to the infinite-layer superconducting nickelate phase of $RNiO_2$. This would be similar to methods such as CaH_2 annealing, which has been shown to induce superconductivity in rare-earth nickelates such as $(Nd,Sr)NiO_2$ and $(La,Sr)NiO_2$. Exploring the possibilities of utilizing ionic liquid gating to manipulate the electronic structure and bridging the gap to superconducting films

can aid in the understanding of rare-earth nickelate superconductivity and boost materials research to realizing exotic physics in correlated systems.

In Li-ion batteries, the interface between the electrode and electrolyte materials can adversely affect the cycling performance, power density, and capacity retention of the batteries. The migration of the Li ions can also induce structural changes in the materials, which can impact the performance. In order to investigate the effects of Li ion removal from a cathode without the formation of a SEI, a delithiation process utilizing Ne^+ sputtering was developed using LCO thin films. The delithiation of the LCO film was found to result in formation of Co^{4+} ions and the presence of holes situated near O atoms to compensate for the charges induced by the Li ion removal. This charge compensation necessitated reconstruction of the surface termination by 0.5 monolayer of Li. Future work in this field can utilize this delithiation process to investigate the electronic structure of electrode and electrolyte materials without a solid electrolyte interface that can impact the material properties.

Epitaxial Ta-LLZO/Li_2O multilayer thin films were successfully deposited on MgO substrates using PLD. These films showed film growth with a χ tilt of approximately 19° and exhibited four-fold symmetry in the XRD φ-scans. Exposure to a liquid electrolyte $LiPF_6$/PC demonstrated the removal of surface contaminants such as Li_2CO_3, as seen through XPS measurements. This electrolyte soaking however also resulted in the formation of a solid-electrolyte interface, where the HF generated from $LiPF_6$ decomposition was found to react with the LLZO structure up to a depth of around 10 nm. Future investigation into the formation of this interface utilizing methods such as neutron reflectometry in conjunction with electrochemical impedance spectroscopy can provide a better understanding behind the mechanisms of the SEI

formation and its effects on the ionic conductivity in hybrid electrolyte cells. This will open further avenues for LLZO SEs to be utilized in hybrid batteries or ASSBs in the future.

Future work involving Ta-LLZO/Li_2O multilayer films will further investigate the formation of the SEI with a LE containing $LiPF_6$. This will be done by utilizing neutron reflectometry along with in-situ electrochemical characterization. Neutron reflectometry is a nondestructive technique that can penetrate deep into samples. This allows for in situ electrochemical measurements that utilize a LE by measuring through the back of the substrate to provide a neutron scattering length density profile. Combining this with XRR and XPS provides a comprehensive image of the formation of a SEI between LLZO and $LiPF_6$, while the electrochemical measurements provide insight into how the SEI formation affects the transport properties between the SE and LE. The investigation into the formation of the SEI and the impact it has on the ionic conductivity is necessary for the realization of utilizing solid electrolytes as a replacement or supplement to liquid electrolytes in Li ion batteries. Solid electrolytes have a promising future as a solution to performance and safety concerns in conventional Li ion batteries that are being used in electronics all around the world.

Appendix A. Measurement and analysis

A.1 X-ray diffraction measurements

Samples were mounted onto a glass slide and attached to the sample plate using a vacuum/magnet. 1 mm size slits were used during measurements to limit the beam dimensions and the detector opening. To align the samples, the axis and positions were first set to an initial zero value. A scan along the Z-direction provided initial height alignment to measure near the surface of the sample, indicated by the halfway point along the height of the detected intensity plateau. The sample surface was then aligned by scanning along the Omega (ω) axis, which aligned the surface normal of the sample to be perpendicular to the incident beam, indicated by the midpoint of the full-width-half-maximum (FWHM) of the resulting curve. These two scans were then repeated to optimize the ω and Z values until the values remained within a range of 0.5 degrees and 0.5 mm.

For XRD 2θ-ω scans, the 2θ and omega values were set at rough estimates of a given substrate peak provided by literature and the Inorganic Crystal Structure Database (ICSD). Alignment scans were then performed to optimize the ω, 2θ, χ, φ, and Z values to obtain a maximum intensity peak for the substrate. In each scan, the alignment position was chosen to be the midpoint of the FWHM. Substrate peaks were chosen for the initial alignment to ensure that the film was oriented properly. The range chosen for scans varied depending on the material and the specific scan. The ω and 2θ alignment was performed around the literature value ± 1°. χ and φ alignment were performed with a range of - 2° to + 2°. Z alignment was performed around the initial Z alignment ± 0.5°. Scans were performed with a step size of 0.005° and a scan speed of 0.5 sec/step.

XRR scans used the same initial alignment for ω and Z as the XRD scans. The 2θ and ω values were then set to 0.4° and 0.2°, respectively. The same ω, 2θ, χ, φ, and Z scans were then used to align the sample surface. XRR scans were performed with a range of 0.4° - 4°, a scan speed of 0.005°, and a scan speed of 0.5 sec/step.

GI-XRD scans used the same initial alignment for ω and Z as the XRD scans. The ω value was then fixed at 0.5°. During the GI-XRD scans, the detector slit was removed to increase the detection of diffracted X-rays. The GI-XRD scan was performed with a fixed ω value and a 2θ range of 10-80°. The step size was 0.005° and the scan speed was 0.5 sec/step.

A.2 X-ray reflectivity simulation

XRR patterns of the deposited thin films were analyzed using the software GenX 3[175]. Before use with GenX 3, the .xrdml files were converted to .xy using the PowDLL converter. The converted files were then imported into the GenX 3 software for simulation fitting. The relevant crystal structures and lattice parameters were inputted into the software (MgO and Ta-LLZO). Three layers of film were used in the simulation to account for interfaces with the substrate and atmosphere. The simulation was then fitted multiple times in order to obtain a good estimate of the overall film thickness.

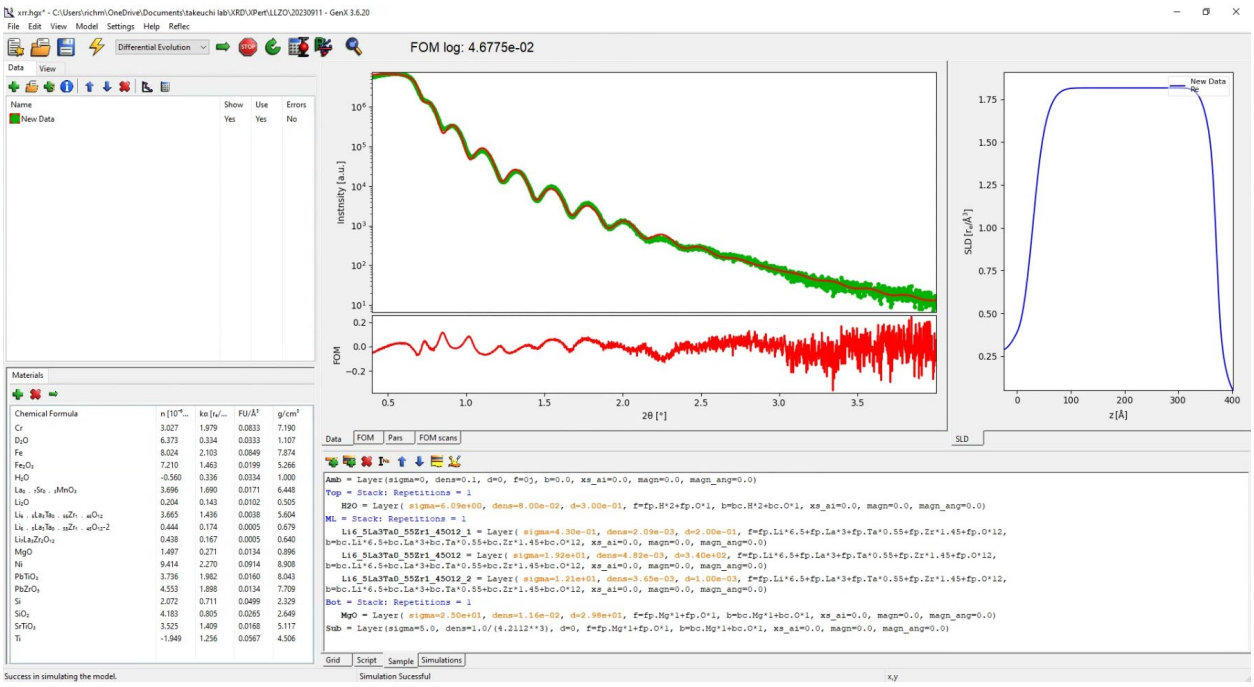

Figure A.1 GenX 3 software used to fit XRR simulations for thickness estimation.

A.3 X-ray photoelectron spectroscopy analysis

XPS data was analyzed using CasaXPS. Files with extension .vms were imported into the software for peak analysis.

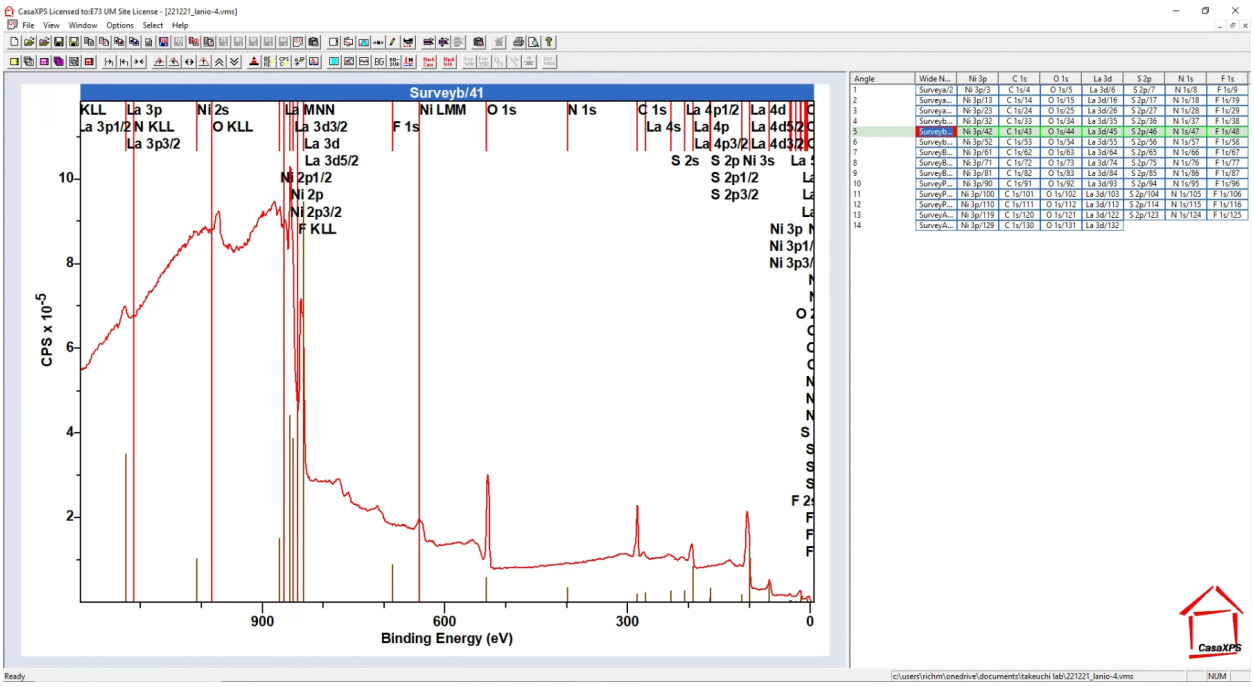

Figure A.2 XPS spectrum of $LaNiO_3$ in CasaXPS with peaks automatically labelled.

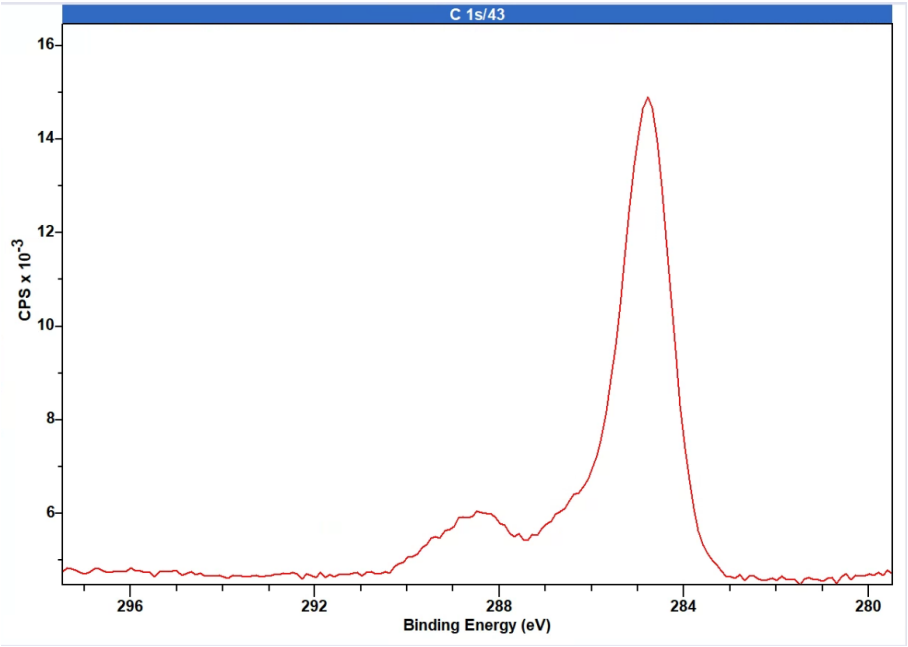

Figure A.3 The C 1s peak used for peak alignment. The peak with larger intensity was calibrated to a binding energy of 284.8 eV.

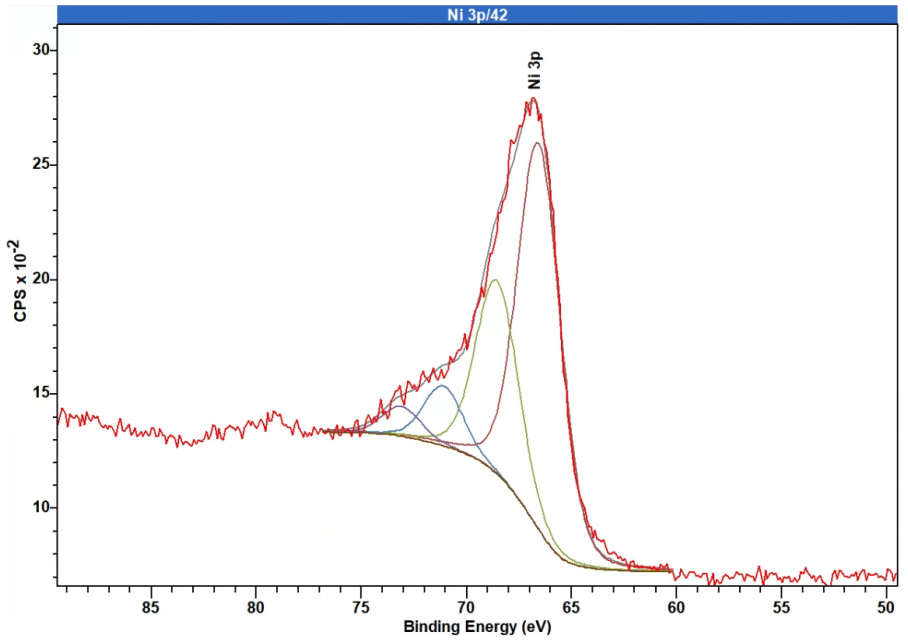

Figure A.4 Ni 3p XPS spectra of $LaNiO_3$ with Shirley background. Background subtraction is not shown.

Appendix B. $LaNiO_3$ XPS tables

Table B.1 Binding energy of O 1s spectrum for IL gated LaNiO3.

				O_{lat}						
	O_V			O – La			O – Ni			
Gating time	B.E. (eV)	FWHM (eV)	RA (%)	B.E. (eV)	FWHM (eV)	RA (%)	B.E. (eV)	FWHM (eV)	RA (%)	O_V/O_{lat}
Pristine	531.21	2.13	50.29	528.59	1.2	25.26	527.99	0.67	21.64	1.072
15 min	531.35	2.17	55.47	528.79	0.99	29.31	528.43	0.78	11.31	1.366
10 hour	531.45	2.11	57.40	528.9	0.99	31.43	528.62	0.81	8.36	1.443
20 hour	530.99	2.04	60.22	528.63	0.87	19.94	528.16	0.79	13.57	1.797
40 hour	531.77	1.93	67.35	528.96	1.12	11.41	528.44	0.93	14.68	2.581

Table B.2 Binding energy of Ni 3p spectra for IL gated $LaNiO_3$.

	Ni^{2+}			Ni^{2+} sat			Ni^{3+}			Ni^{3+} Sat			
Gating time	B.E. (eV)	FWHM (eV)	RA (%)	B.E. (eV)	FWHM (eV)	RA (%)	B.E. (eV)	FWHM (eV)	RA (%)	B.E. (eV)	FWHM (eV)	RA (%)	Ni^{3+}/Ni^{2+}
Pristine	66.45	2.48	50.99	68.45	2.48	25.5	70.08	3.36	15.67	72.08	3.36	7.84	0.307
15 min	66.57	2.41	56.82	68.57	2.41	28.41	71.16	2.5	9.85	73.16	2.5	4.92	0.173
10 hour	66.75	2.44	57.21	68.75	2.44	28.61	71.35	2.43	9.46	73.35	2.43	4.73	0.165
20 hour	66.38	2.47	57.61	68.38	2.47	28.8	70.65	2.19	9.06	72.65	2.19	4.53	0.157
40 hour	66.73	2.61	58.32	68.73	2.61	29.16	71.23	2.28	8.34	73.23	2.28	4.17	0.143

Bibliography

1. Heber, J. Materials science: Enter the oxides. *Nature* **459**, 28–30 (2009).

2. Ishihara, T. *Perovskite oxide for solid oxide fuel cells*. (Springer, 2009).

3. Ashrit, P. *Transition metal oxide thin film-based chromogenics and devices*. (Elsevier Ltd., 2017).

4. Ramanathan, S. *Thin Film Metal-Oxides: Fundamentals and Applications in Electronics and Energy*. (Springer, 2010).

5. Arora, A. K., Jaswal, V. S., Singh, K. & Singh, R. Applications of metal/mixed metal oxides as photocatalyst: A review. *Oriental Journal of Chemistry* vol. 32 2035–2042 Preprint at https://doi.org/10.13005/ojc/320430 (2016).

6. Rao, C. N. R. TRANSITION METAL OXIDES1. (1989).

7. Alexander Pergament *et al. OXIDE ELECTRONICS AND FUNCTIONAL PROPERTIES OF TRANSITION METAL OXIDES*. (Nova Science Publishers, 2014).

8. De Souza, R. A. *5 Ion Transport in Metal Oxides*. (2016).

9. Acosta, E. Thin Films/Properties and Applications. *Thin Films* (2021) doi:10.5772/INTECHOPEN.95527.

10. Abegunde, O. O., Akinlabi, E. T., Oladijo, O. P., Akinlabi, S. & Ude, A. U. Overview of thin film deposition techniques. *AIMS Materials Science* vol. 6 174–199 Preprint at https://doi.org/10.3934/MATERSCI.2019.2.174 (2019).

11. Kittel, C. *Introduction To Solid State Physics*. (John Wiley & Sons Inc, 2005).

12. Callister, W. D. & Rethwisch, D. G. *Fundamentals of Materials Science and Engineering: An Integrated Approach*. (John Wiley & Sons, Inc, 2015).

13. Kofstad, P. *Defects and Transport Properties of Metal Oxides*. *Oxidation of Metals* vol. 44 (1995).

14. Hernandez-Ramirez, F. *et al.* Insight into the role of oxygen diffusion in the sensing mechanisms of SnO2 nanowires. *Adv Funct Mater* **18**, 2990–2994 (2008).

15. Wang, Z., Lin, R., Huo, Y., Li, H. & Wang, L. Formation, Detection, and Function of Oxygen Vacancy in Metal Oxides for Solar Energy Conversion. *Advanced Functional Materials* vol. 32 Preprint at https://doi.org/10.1002/adfm.202109503 (2022).

16. Zhuang, G., Chen, Y., Zhuang, Z., Yu, Y. & Yu, J. Oxygen vacancies in metal oxides: recent progress towards advanced catalyst design. *Sci China Mater* **2020**, 2089–2118 (2013).

17. Al-Hashem, M., Akbar, S. & Morris, P. Role of Oxygen Vacancies in Nanostructured Metal-Oxide Gas Sensors: A Review. *Sens Actuators B Chem* **301**, 126845 (2019).

18. Eom, K. *et al.* Oxygen Vacancy Linear Clustering in a Perovskite Oxide. *Journal of Physical Chemistry Letters* **8**, 3500–3505 (2017).

19. Middey, S. *et al.* Physics of Ultrathin Films and Heterostructures of Rare-Earth Nickelates. *https://doi.org/10.1146/annurev-matsci-070115-032057* **46**, 305–334 (2016).

20. Chakhalian, J. *et al.* Orbital reconstruction and covalent bonding at an oxide interface. *Science (1979)* **318**, 1114–1117 (2007).

21. Stewart, M. K., Liu, J., Kareev, M., Chakhalian, J. & Basov, D. N. Mott Physics near the Insulator-To-Metal Transition in NdNiO 3. *Phys Rev Lett* **107**, 176401 (2011).

22. Catalano, S. *et al.* Rare-earth nickelatesRNiO3: thin films and heterostructures. *Rep. Prog. Phys.* **81**, 46501 (2018).

23. Ha, S. D., Otaki, M., Jaramillo, R., Podpirka, A. & Ramanathan, S. Stable metal–insulator transition in epitaxial SmNiO3 thin films. *J Solid State Chem* **190**, 233–237 (2012).

24. Mercy, A., Bieder, J., Íñiguez, J. & Ghosez, P. Structurally triggered metal-insulator transition in rare-earth nickelates. *Nat Commun* **8**, 1677 (2017).

25. Alonso, J. A. *et al.* Charge Disproportionation in RNiO 3 Perovskites: Simultaneous Metal-Insulator and Structural Transition in YNiO 3. (1999).

26. Chen, B.-J. *et al.* Electronic phase diagram of oxygen-deficient SmNiO3-delta epitaxial thin films. *J. Phys. D: Appl. Phys.* **50**, 235302 (2017).

27. Green, R. J., Haverkort, M. W. & Sawatzky, G. A. Bond disproportionation and dynamical charge fluctuations in the perovskite rare-earth nickelates. *Phys Rev B* **94**, 195127 (2016).

28. Zhu, M. W. *et al.* Strain-induced modification in microstructure and electrical properties of polycrystalline LaNiO3−δ films. *Appl Phys A Mater Sci Process* **122**, 1–7 (2016).

29. Wang, L. *et al.* Oxygen Vacancy Induced Room-Temperature Metal-Insulator Transition in Nickelate Films and Its Potential Application in Photovoltaics. *ACS Appl Mater Interfaces* **8**, 9769–9776 (2016).

30. Liu, J. *et al.* Heterointerface engineered electronic and magnetic phases of NdNiO3 thin films. *Nature Communications 2013 4:1* **4**, 1–11 (2013).

31. Guan, L. *et al.* Electronic structure and optical properties of LaNiO3: First-principles calculations. *Solid State Commun* **150**, 2011–2014 (2010).

32. Allen, S. J. *et al.* Gaps and pseudogaps in perovskite rare earth nickelates. *APL Mater* **3**, 062503 (2015).

33. Bisogni, V. *et al.* Ground-state oxygen holes and the metal–insulator transition in the negative charge-transfer rare-earth nickelates. *Nature Communications 2016 7:1* **7**, 1–8 (2016).

34. Qiao, L. & Bi, X. Direct observation of Ni3+ and Ni2+ in correlated LaNiO3−δ films. *Europhys Lett* **93**, 57002 (2011).

35. Aydogdu, G. H., Ha, S. D., Viswanath, B. & Ramanathan, S. Epitaxy, strain, and composition effects on metal-insulator transition characteristics of SmNiO3 thin films. *J Appl Phys* **109**, 124110 (2011).

36. Torriss, B., Chaker, M. & Margot, J. Electrical and Fourier transform infrared properties of epitaxial SmNiO3 tensile strained thin film. *Appl. Phys. Lett.* **101**, 91908 (2012).

37. Torriss, B., Margot, J. & Chaker, M. Metal-Insulator Transition of strained SmNiO3 Thin Films: Structural, Electrical and Optical Properties. *Sci Rep* **7**, 1–9 (2017).

38. Sidik, U. *et al.* Tunable Proton Diffusion in NdNiO3 Thin Films under Regulated Lattice Strains. *ACS Appl Electron Mater* (2022) doi:10.1021/ACSAELM.2C00711.

39. Li, J., Ramanathan, S. & Comin, R. Carrier Doping Physics of Rare Earth Perovskite Nickelates RENiO3. *Front Phys* **10**, 33 (2022).

40. Wang, Q., Zhou, H. & Ramanathan, S. Electron Doping-Induced Metal–Insulator Transition in LaNiO3 and Memory Devices. *ACS Appl Electron Mater* (2022) doi:10.1021/ACSAELM.2C00242.

41. Shi, J., Zhou, Y. & Ramanathan, S. Colossal resistance switching and band gap modulation in a perovskite nickelate by electron doping. *Nat Commun* **5**, 4860 (2014).

42. Shukla, N. *et al.* Electrically induced insulator to metal transition in epitaxial SmNiO3 thin films. *Appl. Phys. Lett.* **105**, 12108 (2014).

43. Patel, R. K. *et al.* Hole doping in a negative charge transfer insulator. *Communications Physics 2022 5:1* **5**, 1–8 (2022).

44. Shin, Y. & Rondinelli, J. M. Magnetic structure of oxygen-deficient perovskite nickelates with ordered vacancies. *Phys Rev Res* **4**, 22069 (2022).

45. Kotiuga, M. *et al.* Carrier localization in perovskite nickelates from oxygen vacancies. *PNAS* **116**, 21992–21997 (2019).

46. Budiman, R. A. *et al.* Oxygen Nonstoichiometry and Electrochemical Properties of LaNiO 3-δ . *ECS Trans* **66**, 177–183 (2015).

47. Liao, X., Singh, V. & Park, H. Oxygen vacancy induced site-selective Mott transition in LaNiO 3. *Phys. Rev. B.* **103**, (2021).

48. Wang, Y. *et al.* Promoting the Oxygen Evolution Activity of Perovskite Nickelates through Phase Engineering. *ACS Appl Mater Interfaces* **13**, 58566–58575 (2021).

49. Anjeline, C. J., Marate, B. G., Velu, D., Kumar, S. M. S. & Lakshminarasimhan, N. Probing oxygen vacancy-induced mixed-valence states of nickel in LaNiO3 and their

influence on electrocatalytic and magnetic properties. *Mater Chem Phys* **288**, 126331 (2022).

50. Zhang, Y. *et al.* Unravelling the role of oxygen vacancies on the current transport mechanisms in all-perovskite nickelate/titanate heterojunctions for nonvolatile memory applications. *J Appl Phys* **132**, 135303 (2022).

51. Qiao, L. & Bi, X. Direct observation of oxygen vacancy and its effect on the microstructure, electronic and transport properties of sputtered LaNiO3 − δ films on Si substrates. *Thin Solid Films* **519**, 943–946 (2010).

52. Wong, J. C. *et al.* Understanding the Role of Defective Phases on the Conductivity Behavior of Strained Epitaxial LaNiO3Thin Films. *ACS Appl Electron Mater* **4**, 1196–1205 (2022).

53. Zhou, Y. *et al.* Strongly correlated perovskite fuel cells. *Nature* **534**, 231–234 (2016).

54. Shi, J., Ha, S. D., Zhou, Y., Schoofs, F. & Ramanathan, S. A correlated nickelate synaptic transistor. *Nat Commun* **4**, 2676 (2013).

55. Barney, N. & Lutkevich, B. neuromorphic computing. *TechTarget* https://www.techtarget.com/searchenterpriseai/definition/neuromorphic-computing (2023).

56. Corless, V. & Rieck, J. What are neuromorphic computers? *Advanced Science News* https://www.advancedsciencenews.com/what-are-neuromorphic-computers/ (2023).

57. Torrejon, J. *et al.* Neuromorphic computing with nanoscale spintronic oscillators. *Nature 2017 547:7664* **547**, 428–431 (2017).

58. Roy, K., Jaiswal, A. & Panda, P. Towards spike-based machine intelligence with neuromorphic computing. *Nature 2019 575:7784* **575**, 607–617 (2019).

59. Upadhyay, N. K. *et al.* Emerging Memory Devices for Neuromorphic Computing. *Adv Mater Technol* **4**, 1800589 (2019).

60. Schuman, C. D. *et al.* Opportunities for neuromorphic computing algorithms and applications. *Nature Computational Science 2022 2:1* **2**, 10–19 (2022).

61. Burr, G. W. *et al.* Neuromorphic computing using non-volatile memory. *http://dx.doi.org/10.1080/23746149.2016.1259585* **2**, 89–124 (2016).

62. Van De Burgt, Y., Melianas, A., Keene, S. T., Malliaras, G. & Salleo, A. Organic electronics for neuromorphic computing. *Nature Electronics 2018 1:7* **1**, 386–397 (2018).

63. Chen, L., Wang, T.-Y. & Ding, S.-J. Large-scale neuromorphic computing systems. *J Neural Eng* **13**, 051001 (2016).

64. Marković, D., Mizrahi, A., Querlioz, D. & Grollier, J. Physics for neuromorphic computing. *Nature Reviews Physics 2020 2:9* **2**, 499–510 (2020).

65. Caporale, N. & Dan, Y. Spike Timing-Dependent Plasticity: A Hebbian Learning Rule. (2008) doi:10.1146/annurev.neuro.31.060407.125639.

66. Markram, H., Gerstner, W. & Sjöström, P. J. A history of spike-timing-dependent plasticity. *Front Synaptic Neurosci* **3**, 1–24 (2011).

67. Dan, Y. & Poo, M.-M. Spike Timing-Dependent Plasticity of Neural Circuits. *Neuron* **44**, 23–30 (2004).

68. Sánchez, E. Hebbian Theory. https://exploringyourmind.com/hebbian-theory/ (2023).

69. Hebbian Learning - The Decision Lab. https://thedecisionlab.com/reference-guide/neuroscience/hebbian-learning.

70. Yu, S. Neuro-Inspired Computing with Emerging Nonvolatile Memorys. *Proceedings of the IEEE* **106**, 260–285 (2018).

71. Maruyama, S. *et al.* Reversible electrochemical modulation of the superconducting transition temperature of LiTi2O4 ultrathin films by ionic liquid gating. *Appl Phys Lett* **107**, 142602 (2015).

72. Leighton, C. Electrolyte-based ionic control of functional oxides. *Nature Materials 2018 18:1* **18**, 13–18 (2018).

73. Asanuma, S. *et al.* Tuning of the metal-insulator transition in electrolyte-gated NdNiO3 thin films. *Appl Phys Lett* **97**, 142110 (2010).

74. Ha, S. D., Vetter, U., Shi, J. & Ramanathan, S. Electrostatic gating of metallic and insulating phases in SmNiO3 ultrathin films. *Appl Phys Lett* **102**, 183102 (2013).

75. Kalhori, H. *et al.* Oxygen Vacancy in WO3 Film-based FET with Ionic Liquid Gating. *Scientific Reports 2017 7:1* **7**, 1–10 (2017).

76. Du, H., Lin, X., Xu, Z. & Chu, D. Electric double-layer transistors: a review of recent progress. *Journal of Materials Science 2015 50:17* **50**, 5641–5673 (2015).

77. Walter, J., Wang, H., Luo, B., Frisbie, C. D. & Leighton, C. Electrostatic versus Electrochemical Doping and Control of Ferromagnetism in Ion-Gel-Gated Ultrathin La0.5Sr0.5CoO3-δ. *ACS Nano* **10**, 7799–7810 (2016).

78. Paredes, X. *et al.* Thermophysical Properties of 1-Hexyl-3-methylimidazolium bis(trifluoromethylsulfonyl)imide, [C6mim][(CF3SO2)2N]—New Data, Reference Data, and Reference Correlations. *J Phys Chem Ref Data* **49**, 043101 (2020).

79. Nazet, A. *et al.* Densities, Viscosities, and Conductivities of the Imidazolium Ionic Liquids [Emim][Ac], [Emim][FAP], [Bmim][BETI], [Bmim][FSI], [Hmim][TFSI], and [Omim][TFSI]. *J Chem Eng Data* **60**, 2400–2411 (2015).

80. Piatti, E. Ionic gating in metallic superconductors: A brief review. *Nano Express* **2**, 024003 (2021).

81. Ueno, K., Shimotani, H., Iwasa, Y. & Kawasaki, M. Electrostatic charge accumulation versus electrochemical doping in SrTiO3 electric double layer transistors. *Appl Phys Lett* **96**, 252107 (2010).

82. Misra, R., Mccarthy, M. & Hebard, A. F. Electric field gating with ionic liquids. *Appl. Phys. Lett* **90**, 52905 (2007).

83. Rafique, M. *et al.* Ionic Liquid Gating Induced Protonation of Electron-Doped Cuprate Superconductors. *Nano Lett* **19**, 7775–7780 (2019).

84. Bubel, S. *et al.* The electrochemical impact on electrostatic modulation of the metal-insulator transition in nickelates. *Appl Phys Lett* **106**, 122102 (2015).

85. Chen, S. *et al.* The Dynamic Phase Transition Modulation of Ion-Liquid Gating VO2 Thin Film: Formation, Diffusion, and Recovery of Oxygen Vacancies. *Adv Funct Mater* **26**, 3532–3541 (2016).

86. Li, M. *et al.* Suppression of ionic liquid gate-induced metallization of SrTiO 3(001) by oxygen. *Nano Lett* **13**, 4675–4678 (2013).

87. Perera, M. M. *et al.* Improved carrier mobility in few-layer MoS2 field-effect transistors with ionic-liquid gating. *ACS Nano* **7**, 4449–4458 (2013).

88. Jo, S., Costanzo, D., Berger, H. & Morpurgo, A. F. Electrostatically induced superconductivity at the surface of ws2. *Nano Lett* **15**, 1197–1202 (2015).

89. Cui, Y. *et al.* Ionic-Liquid-Gating Induced Protonation and Superconductivity in FeSe, FeSe0.93S0.07, ZrNCl, 1T-TaS2 and Bi2Se3*. *Chinese Physics Letters* **36**, 077401 (2019).

90. Shiogai, J., Ito, Y., Mitsuhashi, T., Nojima, T. & Tsukazaki, A. Electric-field-induced superconductivity in electrochemically etched ultrathin FeSe films on SrTiO3 and MgO. *Nature Physics 2015 12:1* **12**, 42–46 (2015).

91. Ye, J. T. *et al.* Liquid-gated interface superconductivity on an atomically flat film. *Nature Materials 2009 9:2* **9**, 125–128 (2009).

92. Meng, Y. *et al.* Protonation-induced discrete superconducting phases in bulk FeSe single crystals. *Phys Rev B* **105**, 134506 (2022).

93. Ueno, K. *et al.* Discovery of superconductivity in KTaO3 by electrostatic carrier doping. *Nature Nanotechnology 2011 6:7* **6**, 408–412 (2011).

94. Wei, X. *et al.* A selective control of volatile and non-volatile superconductivity in an insulating copper oxide via ionic liquid gating. *Sci Bull (Beijing)* **65**, 1607–1613 (2020).

95. Jeong, J. *et al.* Suppression of metal-insulator transition in VO2 by electric field-induced oxygen vacancy formation. *Science (1979)* **339**, 1402–1405 (2013).

96. Lefler, B. M. *et al.* Voltage Control of Patterned Metal/Insulator Properties in Oxide/Oxyfluoride Lateral Perovskite Heterostructures via Ion Gel Gating. *Adv Funct Mater* 2208434 (2022) doi:10.1002/ADFM.202208434.

97. Passarello, D., Altendorf, S. G., Jeong, J., Samant, M. G. & Parkin, S. S. P. Metallization of Epitaxial VO2 Films by Ionic Liquid Gating through Initially Insulating TiO2 Layers. *Nano Lett* **16**, 5475–5481 (2016).

98. Kan, D., Hatano, T., Abe, A., Ikuta, H. & Shimakawa, Y. Metallic transport properties and electrostatic resistance modulations in LaNiO3 ultrathin channels electrochemically etched in electric-double-layer transistors. *Appl Phys Lett* **117**, 231602 (2020).

99. Qin, M. *et al.* In situ Magnetic Measurements of Ionic-Liquid-Gated Superconducting Films. *J Supercond Nov Magn* **33**, 159–163 (2020).

100. Ding, X. *et al.* Stability of superconducting Nd 0.8 Sr 0.2 NiO 2 thin films. **65**, 267411 (2022).

101. Kouno, S. *et al.* Superconductivity at 38 K at an electrochemical interface between an ionic liquid and FeSe0.8Te0.2 on various substrates. *Scientific Reports 2018 8:1* **8**, 1–9 (2018).

102. Ohno, T. *et al.* Short-term plasticity and long-term potentiation mimicked in single inorganic synapses. *Nat Mater* **10**, 591–595 (2011).

103. Raoux, S., Wełnic, W. & Lelmini, D. Phase change materials and their application to nonvolatile memories. *Chem Rev* **110**, 240–267 (2010).

104. Murray, C. J. Who Really Invented the Rechargeable Lithium-Ion Battery? - IEEE Spectrum. *IEEE Spectrum* https://spectrum.ieee.org/lithium-ion-battery-2662487214 (2023).

105. Fernholm, A. The Nobel Prize in Chemistry 2019. *The Nobel Prize* https://www.nobelprize.org/prizes/chemistry/2019/popular-information/.

106. Blomgren, G. E. The Development and Future of Lithium Ion Batteries. *J Electrochem Soc* **164**, A5019–A5025 (2017).

107. Goodenough, J. B. How we made the Li-ion rechargeable battery. *Nature Electronics 2018 1:3* **1**, 204–204 (2018).

108. How Lithium-ion Batteries Work | Department of Energy. https://www.energy.gov/energysaver/articles/how-lithium-ion-batteries-work.

109. Lithium-Ion Battery - Clean Energy Institute. https://www.cei.washington.edu/education/science-of-solar/battery-technology/.

110. Li, M., Lu, J., Chen, Z. & Amine, K. 30 Years of Lithium-Ion Batteries. *Advanced Materials* vol. 30 Preprint at https://doi.org/10.1002/adma.201800561 (2018).

111. Kim, T., Song, W., Son, D. Y., Ono, L. K. & Qi, Y. Lithium-ion batteries: outlook on present, future, and hybridized technologies. *J Mater Chem A Mater* **7**, 2942–2964 (2019).

112. BU-306: What is the Function of the Separator? - Battery University. https://batteryuniversity.com/article/bu-306-what-is-the-function-of-the-separator.

113. Aurbach, D. Challenges in the Development of Advanced Li-Ion Batteries: A Review. *Energy Environ Sci* (2011) doi:10.1039/C1EE01598B.

114. Goodenough, J. B. & Park, K. S. The Li-ion rechargeable battery: A perspective. *J Am Chem Soc* **135**, 1167–1176 (2013).

115. Tarascon, J. M. & Armand, M. Issues and challenges facing rechargeable lithium batteries. *Nature 2001 414:6861* **414**, 359–367 (2001).

116. Kohlmeyer, R. R. *et al.* Pushing the thermal limits of Li-ion batteries. *Nano Energy* **64**, 103927 (2019).

117. Zhu, G. R. *et al.* Non-flammable solvent-free liquid polymer electrolyte for lithium metal batteries. *Nature Communications 2023 14:1* **14**, 1–12 (2023).

118. Feng, Y. *et al.* Challenges and advances in wide-temperature rechargeable lithium batteries. (2022) doi:10.1039/d1ee03292e.

119. Held, M. & Brönnimann, R. Safe cell, safe battery? Battery fire investigation using FMEA, FTA and practical experiments. *Microelectronics Reliability* **64**, 705–710 (2016).

120. Pfrang, A., Kriston, A., Ruiz, V., Lebedeva, N. & di Persio, F. Safety of Rechargeable Energy Storage Systems with a focus on Li-ion Technology. *Emerging Nanotechnologies in Rechargeable Energy Storage Systems* 253–290 (2017) doi:10.1016/B978-0-323-42977-1.00008-X.

121. Sauer, D. U. SECONDARY BATTERIES – LEAD– ACID SYSTEMS | Lifetime Determining Processes. *Encyclopedia of Electrochemical Power Sources* 805–815 (2009) doi:10.1016/B978-044452745-5.00137-4.

122. Kong, L., Li, C., Jiang, J. & Pecht, M. G. Li-Ion Battery Fire Hazards and Safety Strategies. *Energies 2018, Vol. 11, Page 2191* **11**, 2191 (2018).

123. Lithium Battery Incidents | Federal Aviation Administration. https://www.faa.gov/hazmat/resources/lithium_batteries/incidents.

124. Lithium-ion battery fires from electric cars, bikes and scooters are on the rise. Are firefighters ready? - CBS News. https://www.cbsnews.com/news/lithium-ion-battery-fires-electric-cars-bikes-scooters-firefighters/.

125. Kelly, S. M. Lithium-ion battery fires are happening more often. Here's how to prevent them | CNN Business. *CNN Business* (2023).

126. Xu, K., Zhang, S., Allen, J. L. & Jow, R. Evaluation of Fluorinated Alkyl Phosphates as Flame Retardants in Electrolytes for Li-Ion Batteries I. Physical and Electrochemical Properties. *Article in Journal of The Electrochemical Society* (2003) doi:10.1149/1.1533040.

127. Li, H., Wang, Z., Chen, L. & Huang, X. Research on Advanced Materials for Li-ion Batteries. *Advanced Materials* (2009) doi:10.1002/adma.200901710.

128. Kim, A., Woo, S., Kang, M., Park, H. & Kang, B. Research Progresses of Garnet-Type Solid Electrolytes for Developing All-Solid-State Li Batteries. *Front Chem* **8**, 468 (2020).

129. Awaka, J. *et al.* Crystal structure of fast lithium-ion-conducting cubic Li 7La3Zr2O12. *Chem Lett* **40**, 60–62 (2011).

130. Balaish, M. *et al.* Processing thin but robust electrolytes for solid-state batteries. *Nature Energy 2021 6:3* **6**, 227–239 (2021).

131. Kim, K. J. & Rupp, J. L. M. All ceramic cathode composite design and manufacturing towards low interfacial resistance for garnet-based solid-state lithium batteries. *Energy Environ Sci* **13**, 4930–4945 (2020).

132. Kim, K. J. *et al.* Solid-State Li–Metal Batteries: Challenges and Horizons of Oxide and Sulfide Solid Electrolytes and Their Interfaces. *Adv Energy Mater* **11**, 2002689 (2021).

133. Awaka Ã, J., Kijima, N., Hayakawa, H. & Akimoto, J. Synthesis and structure analysis of tetragonal Li 7 La 3 Zr 2 O 12 with the garnet-related type structure. (2009) doi:10.1016/j.jssc.2009.05.020.

134. Bernstein, N., Johannes, M. D. & Hoang, K. Origin of the Structural Phase Transition in Li7La3Zr2O12. (2012) doi:10.1103/PhysRevLett.109.205702.

135. Thompson, T. *et al.* Tetragonal vs. cubic phase stability in Al – free Ta doped Li 7 La 3 Zr 2 O 12 (LLZO). *J Mater Chem A Mater* **2**, 13431–13436 (2014).

136. Raju, M. M., Altayran, F., Johnson, M., Wang, D. & Zhang, Q. Crystal Structure and Preparation of Li7La3Zr2O12 (LLZO) Solid-State Electrolyte and Doping Impacts on the Conductivity: An Overview. *Electrochem 2021, Vol. 2, Pages 390-414* **2**, 390–414 (2021).

137. Pfenninger, R., Struzik, M., Garbayo, I., Stilp, E. & Rupp, J. L. M. A low ride on processing temperature for fast lithium conduction in garnet solid-state battery films. *Nature Energy 2019 4:6* **4**, 475–483 (2019).

138. van den Broek, J. *et al.* Interface-Engineered All-Solid-State Li-Ion Batteries Based on Garnet-Type Fast Li+ Conductors. *Adv Energy Mater* **6**, 1600736 (2016).

139. Raju, M. M., Altayran, F., Johnson, M., Wang, D. & Zhang, Q. Crystal Structure and Preparation of Li7La3Zr2O12 (LLZO) Solid-State Electrolyte and Doping Impacts on the Conductivity: An Overview. *Electrochem 2021, Vol. 2, Pages 390-414* **2**, 390–414 (2021).

140. Kim, S., Hirayama, M., Taminato, S. & Kanno, R. Epitaxial growth and lithium ion conductivity of lithium- oxide garnet for an all solid-state battery electrolyte. *Dalton Transactions* **42**, 13112–13117 (2013).

141. Zhu, Y. *et al.* Lithium-film ceramics for solid-state lithionic devices. *Nature Reviews Materials 2020 6:4* **6**, 313–331 (2020).

142. Katsui, H. & Goto, T. Preparation of cubic and tetragonal Li7La3Zr2O12 film by metal organic chemical vapor deposition. *Thin Solid Films* **584**, 130–134 (2015).

143. Loho, C., Djenadic, R., Bruns, M., Clemens, O. & Hahn, H. Garnet-Type Li 7 La 3 Zr 2 O 12 Solid Electrolyte Thin Films Grown by CO 2 -Laser Assisted CVD for All-Solid-State Batteries . *J Electrochem Soc* **164**, A6131–A6139 (2017).

144. Bitzer, M., Van Gestel, T., Uhlenbruck, S. & Hans-Peter-Buchkremer. Sol-gel synthesis of thin solid Li7La3Zr2O12 electrolyte films for Li-ion batteries. *Thin Solid Films* **615**, 128–134 (2016).

145. Tadanaga, K. *et al.* Preparation of lithium ion conductive Al-doped Li7La3Zr2O12 thin films by a sol–gel process. *J Power Sources* **273**, 844–847 (2015).

146. Sastre, J. *et al.* Lithium Garnet Li7La3Zr2O12 Electrolyte for All-Solid-State Batteries: Closing the Gap between Bulk and Thin Film Li-Ion Conductivities. *Adv Mater Interfaces* **7**, 2000425 (2020).

147. Zhang, Y. *et al.* Towards better Li metal anodes: Challenges and strategies. *Materials Today* **33**, 56–74 (2020).

148. Besli, M. M. *et al.* Effect of Liquid Electrolyte Soaking on the Interfacial Resistance of Li7La3Zr2O12 for All-Solid-State Lithium Batteries. *ACS Appl Mater Interfaces* **12**, 20605–20612 (2020).

149. Yan, S. *et al.* Revealing the Role of Liquid Electrolytes in Cycling of Garnet-Based Solid-State Lithium-Metal Batteries. *J. Phys. Chem. C* **2022**, 126–14027 (2022).

150. Zhang, N., Hei, Z., Wu, S., Liu, J. & Duan, H. Effect of solution soaking on the electrochemical properties of Li 6.5 La 3 Zr 1.5 Ta 0.5 O 12 /polyethylene oxide composite electrolyte.

151. Flatscher, F. *et al.* Deflecting dendrites by introducing compressive stress in Li 7 La 3 Zr 2 O 12 using ion implantation. (2023) doi:10.26434/chemrxiv-2023-311rv.

152. Choi, S. *et al.* Systematic study on Li dendrite growth and suppression in pouch-type lithium-ion batteries with misaligned electrode pairs. *J Power Sources* **579**, 233265 (2023).

153. Gao, Y. *et al.* Classical and Emerging Characterization Techniques for Investigation of Ion Transport Mechanisms in Crystalline Fast Ionic Conductors. *Chem Rev* **120**, 5954–6008 (2020).

154. Leng, J. *et al.* Insight into the solid-liquid electrolyte interphase between Li 6.4 La 3 Zr 1.4 Ta 0.6 O 12 and LiPF 6-based liquid electrolyte. *Appl Surf Sci* (2021) doi:10.1016/j.apsusc.2021.151638.

155. Liu, J. *et al.* The Interface between Li6.5La3Zr1.5Ta0.5O12 and Liquid Electrolyte. *Joule* **4**, 101–108 (2020).

156. Gupta, A., Kazyak, E., Dasgupta, N. P. & Sakamoto, J. Electrochemical and Surface Chemistry Analysis of Lithium Lanthanum Zirconium Tantalum Oxide (LLZTO)/Liquid Electrolyte (LE) Interfaces. *J Power Sources* **474**, 228598 (2020).

157. Keller, M., Varzi, A. & Passerini, S. Hybrid electrolytes for lithium metal batteries. (2018) doi:10.1016/j.jpowsour.2018.04.099.

158. Xu, Y. *et al.* Promoting Mechanistic Understanding of Lithium Deposition and Solid-Electrolyte Interphase (SEI) Formation Using Advanced Characterization and Simulation Methods: Recent Progress, Limitations, and Future Perspectives. *Adv Energy Mater* **12**, 2200398 (2022).

159. Tan, H., Takeuchi, S., Bharathi, K. K., Takeuchi, I. & Bendersky, L. A. Microscopy Study of Structural Evolution in Epitaxial LiCoO2 Positive Electrode Films during Electrochemical Cycling. *ACS Appl Mater Interfaces* **8**, 6727–6735 (2016).

160. Salagre, E. *et al.* Physical Delithiation of Epitaxial LiCoO2 Battery Cathodes as a Platform for Surface Electronic Structure Investigation. *ACS Appl Mater Interfaces* **15**, 36224–36232 (2023).

161. Lyu, Y. *et al.* An Overview on the Advances of LiCoO2 Cathodes for Lithium-Ion Batteries. *Adv Energy Mater* **11**, 2000982 (2021).

162. Takeuchi, S. *et al.* Epitaxial LiCoO 2 Films as a Model System for Fundamental Electrochemical Studies of Positive Electrodes. (2015) doi:10.1021/am508512q.

163. Ihrig, M. *et al.* Study of LiCoO2/Li7La3Zr2O12:Ta Interface Degradation in All-Solid-State Lithium Batteries. *ACS Appl Mater Interfaces* **14**, 11288–11299 (2022).

164. Shepelin, N. A. *et al.* A practical guide to pulsed laser deposition. *Chem Soc Rev* **52**, 2294 (2023).

165. Introduction To Pulsed Laser Deposition (PLD):8 Applications. *VACCOAT* https://vaccoat.com/blog/what-is-pulsed-laser-deposition-pld/ (2013).

166. Bhaumik, M. L., Bradford, R. S. & Ault, E. R. High-efficiency KrF excimer laser. *Appl Phys Lett* **28**, 23–24 (1976).

167. Paschotta, R. *Field Guide to Lasers*. (SPIE Press, 2008).

168. Oura, K., Katayama, M., Zotov, A. V., Lifshits, V. G. & Saranin, A. A. Growth of Thin Films. in *Surface Science* 357–387 (Springer, Berlin, Heidelberg, 2003). doi:10.1007/978-3-662-05179-5_14.

169. Schlom, D. G., Chen, L. Q., Pan, X., Schmehl, A. & Zurbuchen, M. A. A Thin Film Approach to Engineering Functionality into Oxides. *Journal of the American Ceramic Society* **91**, 2429–2454 (2008).

170. Chambers, S. A. Epitaxial growth and properties of thin film oxides. *Surf Sci Rep* **39**, 105–180 (2000).

171. Osada, M. *et al.* Nickelate Superconductivity without Rare-Earth Magnetism: (La,Sr)NiO2. *Advanced Materials* **33**, 2104083 (2021).

172. Dudley, M. & Huang, X. R. Epitaxial Layers, X-ray Characterization of. *Encyclopedia of Materials: Science and Technology* 2775–2786 (2001) doi:10.1016/B0-08-043152-6/00494-0.

173. Stabrawa, I. *et al.* Characterization of the morphology of titanium and titanium (IV) oxide nanolayers deposited on different substrates by application of grazing incidence X-ray diffraction and X-ray reflectometry techniques. *Thin Solid Films* **671**, 103–110 (2019).

174. Miller, A. M. *et al.* Extracting information from X-ray diffraction patterns containing Laue oscillations. *Zeitschrift fur Naturforschung - Section B Journal of Chemical Sciences* **77**, 313–322 (2022).

175. Glavic, A. & Björck, M. GenX 3: The latest generation of an established tool. *J Appl Crystallogr* **55**, 1063–1071 (2022).

176. Fairley, N. *et al.* Systematic and collaborative approach to problem solving using X-ray photoelectron spectroscopy. *Applied Surface Science Advances* **5**, 100112 (2021).

177. Fang, D., He, F., Xie, J. & Xue, L. Calibration of Binding Energy Positions with C1s for XPS Results. *Journal Wuhan University of Technology, Materials Science Edition* **35**, 711–718 (2020).

178. Leng, Y. *Materials Characterization*. (Wiley-VCH Verlag GmbH & Co., 2013).

179. Wei, H., Jenderka, M., Grundmann, M. & Lorenz, M. LaNiO3 films with tunable out-of-plane lattice parameter and their strain-related electrical properties. *physica status solidi (a)* **212**, 1925–1930 (2015).

180. Wold, A., Post, B. & Banks, E. Rare Earth Nickel Oxides. *J Am Chem Soc* **79**, 4911–4913 (1957).

181. Wrobel, F. *et al.* Comparative study of LaNiO3/LaAlO3 heterostructures grown by pulsed laser deposition and oxide molecular beam epitaxy. *Appl Phys Lett* **110**, 41606 (2017).

182. Zanatta, A. R. Revisiting the optical bandgap of semiconductors and the proposal of a unified methodology to its determination. *Scientific Reports 2019 9:1* **9**, 1–12 (2019).

183. Cui, Y., Ren, J., Yang, G. & Gao, Y. First-Principles Study of Intrinsic Point Defects and Optical Properties of SmNiO3. *J. Phys. Chem. A* **125**, 356–365 (2021).

184. Li, P., Tian, C., Yang, W., Zhao, W. & Lü, Z. LaNiO3 modified with Ag nanoparticles as an efficient bifunctional electrocatalyst for rechargeable zinc–air batteries. *Front Mater Sci* **13**, 277–287 (2019).

185. Fu, Y. *et al.* Core-level x-ray photoemission and Raman spectroscopy studies on electronic structures in Mott-Hubbard type nickelate oxide NdNiO 2. (2020).

186. Qiu, Y. *et al.* Understanding the Enhancement Mechanism of A-Site-Deficient LaxNiO3 as an Oxygen Redox Catalyst. *Chemistry of Materials* **32**, 1864–1875 (2020).

187. Kawai, M. *et al.* Reversible changes of epitaxial thin films from perovskite LaNiO3 to infinite-layer structure LaNiO2. *Appl Phys Lett* **94**, 082102 (2009).

188. Carley, A. F., Chalker, P. R. & Roberts, M. W. Defects in Oxide Overlayers at Nickel Single-Crystal Surfaces. *Source: Proceedings of the Royal Society of London. Series A* **399**, 167–179 (1985).

189. Dubey, P., Kaurav, N., Devan, R. S., Okram, G. S. & Kuo, Y. K. The effect of stoichiometry on the structural, thermal and electronic properties of thermally decomposed nickel oxide †. (2018) doi:10.1039/c8ra00157j.

190. Amarasinghe, D. K. *et al.* Electron doping of NdNiO3 thin films using dual chamber CaH2 annealing. *J Solid State Chem* **315**, 123512 (2022).

191. Mickevičius, S. *et al.* Investigation of epitaxial LaNiO3−x thin films by high-energy XPS. *J Alloys Compd* **423**, 107–111 (2006).

192. Maluf, S. S., Tanabe, E. Y., Nascente, P. A. P. & Assaf, E. M. Study of water-gas-shift reaction over La(1-y)Sr yNixCo(1-x)O3 perovskite as precursors. *Top Catal* **54**, 210–218 (2011).

193. Hien-Hoang, V., Chung, N. K. & Kim, H. J. Electrical transport properties and Kondo effect in La 1− x Pr x NiO 3−δ thin films. *Scientific Reports 2021 11:1* **11**, 1–10 (2021).

194. Burriel, M. *et al.* Absence of Ni on the outer surface of Sr doped La 2 NiO 4 single crystals. *Energy Environ Sci* **7**, 311–316 (2013).

195. McBean, C. L. *et al.* Generalizable, Electroless, Template-Assisted Synthesis and Electrocatalytic Mechanistic Understanding of Perovskite LaNiO3 Nanorods as Viable, Supportless Oxygen Evolution Reaction Catalysts in Alkaline Media. *ACS Appl Mater Interfaces* **9**, 24634–24648 (2017).

196. Jaramillo, R., Schoofs, F., Ha, S. D. & Ramanathan, S. High pressure synthesis of SmNiO 3 thin films and implications for thermodynamics of the nickelates. *J Mater Chem C Mater* **1**, 2455–2462 (2013).

197. Lin, H., Jakub Gawryluk, D., Maximilian Klein, Y. & Lechermann, F. Assessing the correlated electronic structure of lanthanum nickelates. *Electronic Structure* **4**, 015005 (2022).

198. Shannon, R. D. Revised effective ionic radii and systematic studies of interatomic distances in halides and chalcogenides. *Acta Crystallographica Section A* **32**, 751–767 (1976).

199. Hepting, M. *et al.* Electronic structure of the parent compound of superconducting infinite-layer nickelates. *Nature Materials 2020 19:4* **19**, 381–385 (2020).

200. Christensen, D. V. *et al.* 2022 roadmap on neuromorphic computing and engineering. *Neuromorphic Computing and Engineering* **2**, 022501 (2022).

201. Fowlie, J. *et al.* Conductivity and Local Structure of LaNiO3 Thin Films. *Advanced Materials* **29**, 1605197 (2017).

202. Ardizzone, I. *et al.* Optical properties of ${\rm La}{\rm Ni}{\rm O}_3$ films tuned from compressive to tensile strain. *Phys Rev B* **102**, 155148 (2020).

203. Salg, P. *et al.* Oxygen diffusion barriers for epitaxial thin-film heterostructures with highly conducting SrMoO3 electrodes. *J Appl Phys* **127**, 65302 (2020).

204. Detavernier, C., Van Meirhaeghe, R. L., Cardon, F., Donaton, R. A. & Maex, K. The influence of Ti capping layers on CoSi2 formation. *Microelectron Eng* **50**, 125–132 (2000).

205. Chen, B. *et al.* Influence of oxygen diffusion through capping layers of low work function metal gate electrodes. *IEEE Electron Device Letters* **27**, 228–230 (2006).

206. Bulusu, A., Kim, H., Samet, D. & Graham, S. Improving the stability of atomic layer deposited alumina films in aqueous environments with metal oxide capping layers. *J Phys D Appl Phys* **46**, 084014 (2013).

207. Schroeder, J. L., Ingason, A. S., Rosén, J. & Birch, J. Beware of poor-quality MgO substrates: A study of MgO substrate quality and its effect on thin film quality. (2015) doi:10.1016/j.jcrysgro.2015.03.010.

208. Madsen, L. D., Madsen, L. D., My Charavel, R., Birch, J. & Svedberg, E. B. Assessment of MgO(1 0 0) and (1 1 1) substrate quality by X-ray diffraction. *J Cryst Growth* **209**, (2000).

209. Moulder, J. F., Stickle, W. F., Sobol, P. E. & Bomben, K. D. *Handbook of X-ray Photoelectron Spectroscopy*. (Perkin-Elmer Corporation).

210. Naumkin, A. V., Kraut-Vass, A., Gaarenstroom, S. W. & Powell, C. J. *NIST X-ray Photoelectron Spectroscopy Database 20*.

211. Cheng, L. *et al.* The origin of high electrolyte–electrode interfacial resistances in lithium cells containing garnet type solid electrolytes. *Physical Chemistry Chemical Physics* **16**, 18294–18300 (2014).

212. Heider, U., Oesten, R. & Jungnitz, M. Challenge in manufacturing electrolyte solutions for lithium and lithium ion batteries quality control and minimizing contamination level. *J Power Sources* **81–82**, 119–122 (1999).

213. Parimalam, B. S., MacIntosh, A. D., Kadam, R. & Lucht, B. L. Decomposition Reactions of Anode Solid Electrolyte Interphase (SEI) Components with LiPF6. *Journal of Physical Chemistry C* **121**, 22733–22738 (2017).

214. Sunding, M. F. *et al.* XPS characterisation of in situ treated lanthanum oxide and hydroxide using tailored charge referencing and peak fitting procedures. *J Electron Spectros Relat Phenomena* **184**, 399–409 (2011).

215. Parimalam, B. S. & Lucht, B. L. Reduction Reactions of Electrolyte Salts for Lithium Ion Batteries: LiPF6, LiBF4, LiDFOB, LiBOB, and LiTFSI. doi:10.1149/2.0901802jes.

216. Plakhotnyk, A. V., Ernst, L. & Schmutzler, R. Hydrolysis in the system LiPF6—propylene carbonate—dimethyl carbonate—H2O. *J Fluor Chem* **126**, 27–31 (2005).

217. Stich, M., Göttlinger, M., Kurniawan, M., Schmidt, U. & Bund, A. Hydrolysis of LiPF6 in Carbonate-Based Electrolytes for Lithium-Ion Batteries and in Aqueous Media. *Journal of Physical Chemistry C* **122**, 8836–8842 (2018).

218. Shen, W., Wang, X. D., Cattrall, R. W., Nyberg, G. L. & Liesegang, J. XPS analysis of hydroxide ion surface reactions on reactions on CeF3 and LaF3 fluoride ion-selective electrodes. *Electroanalysis* **9**, 917–921 (1997).

219. Yu, H. *et al.* Characterization of LaF3 coatings prepared at different temperatures and rates. *Appl Surf Sci* **254**, 1783–1788 (2008).

220. Greczynski, G. & Hultman, L. X-ray photoelectron spectroscopy: Towards reliable binding energy referencing. *Prog Mater Sci* **107**, 100591 (2020).